GREEN COMPOSITES FROM CASTOR OIL AND RENEWABLE REINFORCING MATERIALS: MALEATED CASTOR OIL-POLYSTYRENE MATRIX REINFORCED WITH GREIGE FIBRE

A dissertation submitted in fulfilment of the requirements for the Degree of Master of Science in Engineering to the Faculty of Engineering and the Built Environment of the University of Cape Town, Cape Town, South Africa

by

Lizé-Mari Ferreira

Centre for Materials Engineering
Department of Mechanical Engineering
University of Cape Town
November 2019

ABSTRACT

The need to find biodegradable alternatives for common polymer materials has risen due to the increase in pollution (soil and water) and the effects that it has on the ocean and wildlife. Alternatives can be found by turning to plant-based oils, for example castor oil, to be used in the synthesis of a variety of monomers. Castor oil is suitable as it is non-edible; thus its use does not deplete food sources and it has high chemical reactivity.

In this study, medical grade castor oil was maleated by the addition of maleic anhydride to form maleated castor oil (MACO). This reaction was performed at 98 ˚C for five hours. The completion of the reaction was monitored using acid value. The maleated castor oil was reacted with styrene monomer (at 60 ˚C) and thermally cured to form a tough but flexible polymer (MACOPS). Curing took place for two hours at 90 ˚C, two hours at 120 ˚C and 1 hour at 160 ˚C. Additionally, the synthesized polymer matrix was reinforced with alkalized greige fibres (consisting of a hemp and cotton mix) using a hand lay-up process. Mechanical tests - tensile, flexural and impact strength - were performed on the neat and reinforced polymer. Comparison tests (to determine mechanical properties) were also conducted on commercial general purpose polystyrene (GPPS) and high impact polystyrene (HIPS). Scanning electron microscopy (SEM) was performed on the tensile fracture surfaces of the reinforced matrix. The crosslink density, contact angles and density of the synthesized polymer were determined. Differential scanning calorimetry (DSC) was used to determine the glass transition temperature(s) of the synthesized and commercial polymers. Thermogravimetry was performed on the synthesized matrix as well as the commercial polymers to determine operating temperatures. Raman spectroscopy was used to obtain structural information on the synthesized polymer as well as confirm the successful completion of the maleation reaction. To test for the compostability of the maleated castor oil-polystyrene polymer matrix, biodegradability tests were conducted for a period of ten weeks. The degraded samples underwent tensile testing and the contact angles were determined. Transmission electron microscopy (TEM) was used to see the distribution of polystyrene throughout HIPS and the MACOPS matrix.

The acid value at the start of the reaction was 80.1/100 mgNaOH and at the end of the reaction the acid value decreased to 74.7/100 mgNaOH. A decrease in acid value indicated that the maleic anhydride stopped reacting at the end of the reaction. An increase in viscosity of the mixture served as an indication that the maleation reaction did take place.

ASTM D6110 was used for the Charpy impact test. HIPS performed as expected with the highest impact strength of 58.4 kJ/m^2. The addition of MACO to styrene monomer led to an increase in the toughness of the end product. An increase was observed for both the MACOPS and reinforced MACOPS compared to GPPS. MACOPS and reinforced MACOPS had impact strengths of 41.5 kJ/m^2 and 45.0 kJ/m^2 respectively. The addition of the reinforcing greige fibres did not significantly improve the impact strength. GPPS had the lowest impact strength of 33.9 kJ/m^2.

Tensile tests were conducted according to ASTM D638. For MACOPS an ultimate tensile strength (UTS) of 23.0 MPa and a Young's modulus of 983 MPa were found. GPPS on the other hand had a much higher UTS and Young's modulus of 44.8 MPa and 3.3 GPa respectively. Once again the MACOPS had tensile properties closer to those of HIPS. The UTS and Young's modulus of HIPS was 13.5 MPa and 1.5 GPa respectively. The reinforced MACOPS did not perform very well under tension with a UTS of 13.1 MPa and a Young's modulus of only 283 MPa. The theoretical modulus of the composite was calculated using the Rule of Mixtures and the Halpin-Tsai model to determine the efficiency of the greige fibres as reinforcement. The efficiency was determined to be less than 30%.

Flexural tests were conducted according to ASTM D7264. A significant difference in the flexibility of the synthesized polymer was found when compared to GPPS. MACOPS had a maximum flexural strength of 22.1 MPa whereas GPPS had a flexural strength of 74.4 MPa. The MACOPS had flexural properties closer to that of HIPS which had a flexural strength of 27.2 MPa. The reinforced MACOPS had a flexural strength of 12.2 MPa. This was ascribed to the presence of significant delamination.

GPPS and HIPS have no crosslinks between the polymer chains. A crosslink density of 2.1×10^{-3} mol/cm^3 was determined for the MACOPS matrix. This could point to co-polymer formation between MACO and polystyrene.

Raman spectroscopy was used to determine if the maleation of castor oil took place successfully. Maleic anhydride has signature absorption bands at 1850 cm^{-1} and 1790 cm^{-1}. These peaks were absent in the MACO spectrum, which suggests complete reaction. Signature peaks of both the MACO and GPPS were present in the spectrum of MACOPS. This also may point to co-polymer formation. A Raman map of MACOPS showed uniform distribution of polystyrene throughout the sample whereas HIPS had numerous gaps where polystyrene was of low intensity. This points to the presence of sections containing polybutadiene. Therefore MACOPS can be characterized as either a co-polymer or an interpenetrating polymer network.

MACOPS displayed two glass transition temperatures (Tg) when analyzed with DSC. A small (low intensity) glass transition temperature peak was observed at 93.2 °C and a second of higher intensity at 54.9 ˚C. Two glass transition temperature can point to an interpenetrating polymer network. The Tg of 54.9 ˚C was assigned to a co-polymer. The Tg of 93.2 ˚C is possibly due to a small amount of homo-polymerized polystyrene. Due to the fact that the glass transition temperature is relatively close to ambient temperature, the matrix is relatively flexible but not elastomeric; hard and tough but not very brittle.

Thermogravimetry indicated a thermal degradation onset temperature of 336 °C for the MACOPS matrix. The onset temperature for thermal degradation of MACOPS is lower than those of HIPS and GPPS.

After biodegradability testing, no significant loss in mechanical properties was observed for the MACOPS matrix and reinforced composite. MACOPS showed the most mass loss (10.4%) in

comparison with the other materials. A significant decrease was seen in the contact angle measurements of the degraded reinforced MACOPS. The contact angle decreased from 88˚ (original) to 54.2˚ (degraded). This points to surface changes as a result of degradation that decreases the hydrophobicity of the material.

It can be seen that the addition of MACO to styrene monomer most likely results in an IPN with a degree of crosslinking. The properties of this matrix is closer to those of HIPS than GPPS. The matrix is hard, tough and more flexible than GPPS. At room temperature the MACOPS matrix is used just above its glass transition temperature. Reinforcing the matrix with greige fibres led to a decrease in mechanical properties. Thus the fibres acted only as a filler. The synthesized MACOPS matrix is hydrophilic and shows no significant degradation when placed in compost after a period of 10 weeks.

ACKNOWLEDGEMENTS

Firstly, I would like to thank my supervisor, Dr Chris Woolard, for sharing his knowledge and supporting me through this journey. His help and input into making my research a success is greatly appreciated.

I would like to thank the University of Cape Town and Dr Chris Woolard for funding this project.

Thank you to the CSIR IBS-program for funding my studies during 2019.

The practical aspect of my research would have been challenging without the help of Dr Richard Curry and Ms Penny Louw. Their assistance with the mechanical testing and general enquiries is greatly appreciated.

Thank you to Mr James Dicks for sharing his valuable insights, whilst completing his journey to a master's degree specializing in biodegradable polymer foams. During my journey he was always available to bounce off ideas on and to share my results.

Thank you to Mr Mikyle Paul that helped with mould and part designs on Solidworks that were needed for my experiments.

All my moulds and parts needed were manufactured in-house at the Mechanical Engineering workshop. Thank you to their team for their great work. A big thank you to Mr Pierre Smith for ensuring the designs were correct and ensuring the work was done on time.

Thank you to Advanced Material Solutions for the waterjet cutting of my samples. Your work is of great quality.

Thank you to Mrs Miranda Waldron and Ms Nasheeta Hanief for conducting the Raman and SEM analysis. Thank you to Mr Mohammed Jaffer for the sample preparation done for TEM and the analysis thereof.

Thank you to Mr Lukhanyo Bolo from the Nelson Mandela University for conducting DSC and TG measurements.

Lastly, I would like to thank my family, my mother, Karen, and my father, Herman, as well as my fiancé, Kobus, for believing in me. I am ever grateful for their support during difficult times and their continuous encouragement to keep going.

DECLARATION

I know the meaning of plagiarism and declare that all the work in the document, save for that which is properly acknowledged, is my own.

This thesis/dissertation has been submitted to the Turnitin module (or equivalent similarity and originality checking software) and I confirm that my supervisor has seen my report and any concerns revealed by such have been resolved with my supervisor.

Signature Signed by candidate

Date 07/11/2019

TABLE OF CONTENTS

ABSTRACT i
ACKNOWLEDGEMENTS iv
DECLARATION v
TABLE OF CONTENTS vi
LIST OF FIGURES ix
LIST OF TABLES xii
LIST OF SYMBOLS, CODES AND ACRONYMS xiii
Chapter 1: Introduction 1
1.1 Background and motivation for this study 1
1.2 Objectives of this study 2
1.3 Scope and limitations of this study 2
Chapter 2: Literature Review 3
2.1. Physical and chemical properties of castor oil and uses 3
Overview 3
Chemical properties 4
Physical properties 4
2.2. Polymers synthesized by using castor oil and modifications of castor oil 5
Polyurethanes 6
Polyamides 6
Polyesters 7
Co-polymers 7
Interpenetrating polymer networks 7
Others 9
2.3. Methods of maleation 9
2.4. Properties of castor oil polyurethane composites versus maleated castor oil composites 13
Castor oil polyurethanes 13
Maleated castor oil composites 15
2.5. Natural fibre reinforcements 17
Overview 17
Modification of natural fibres by alkalization 21

Fibre reinforcements in automotive applications....22
Hemp fibre....23
Cotton fibre....24
Reinforcing methods....25
2.6. Biodegradation of polymers....27
Chapter 3: Experimental methods and materials....30
3.1 Materials....30
3.2 Experimental methods: Synthesis and sample preparation....30
3.2.1 Maleation of castor oil....30
3.2.2 Determination of acid value....30
3.2.3 Purification of styrene....32
3.2.4 Matrix formation of maleated castor oil with styrene....32
3.2.5 Preparation of crosslinked resin....32
3.2.6 Sample preparation....34
3.2.7 Alkalization treatment of hemp-cotton (greige) fibres....34
3.2.8 Hand lay-up process and curing of hemp-cotton fibres in resin....35
3.2.9 Determination of manufacturing volume fraction of fibres....35
3.2.10 Determination of crosslink density using a swelling test....35
3.3 Experimental methods: Property testing....36
3.3.1 Impact testing....36
3.3.2 Tensile testing....37
3.3.3 Efficiency of the fibre reinforcement....40
3.3.4 Flexural testing....41
3.3.5 Specific strength and specific toughness....42
3.3.6 Hardness measurement....43
3.3.7 Density measurement....43
3.3.8 Differential scanning calorimetry....44
3.3.9 Thermogravimetry....44
3.3.10 Biodegradability testing....44
3.3.11 Contact-angle measurements....46
3.4 Experimental methods: Optical characterization....46
3.4.1 Raman spectroscopy....46
3.4.2 Scanning electron microscopy of fracture surfaces....47

3.4.3 Transmission electron microscopy 47
Chapter 4: Results and discussion 48
4.1 Synthesis and sample preparation 48
4.1.1 Acid values 48
4.1.2 Matrix formation of maleated castor oil with styrene 50
4.1.3 Curing of resin 50
4.1.4 Curing of reinforced resin 53
4.1.6 Swelling testing of neat MACOPS 54
4.2 Property testing 55
4.2.1 Impact testing 55
4.2.2 Tensile testing 56
4.2.3 Efficiency of the fibre reinforcement 65
4.2.4 Flexural (3-point bending) testing 65
4.2.5 Hardness testing 73
4.2.6 Density of the polymer and composite samples 73
4.2.7 Specific strength and specific toughness 74
4.2.8 DSC analysis 75
4.2.9 Thermogravimetry 76
4.2.10 Biodegradability testing 80
4.2.11 Contact-angle measurements 82
4.3 Optical characterization 83
4.3.1 Transmission Electron Microscopy 83
4.3.2 Raman analysis 84
4.3.3 SEM analysis of the fracture surface of reinforced MACOPS 87
Chapter 5: Conclusions 92
Chapter 6: Recommendations and future work 94
References 96
Appendix A: Temperature profiling of the vulcanization press 106
Experimental Procedure 106
Results 106
Appendix B: Tensile test of fibres 110
Appendix C: Tensile stress-strain curves for biodegraded samples 111
Appendix D: Contact angles 113

LIST OF FIGURES

Figure 1: (a) Castor oil plant [6] and (b) castor beans [141] 3
Figure 2: Chemical structure of glyceryltriricinoleate [143] 4
Figure 3: Synthesis of poly(amide-hydroxyurethane) through bulk ring opening polymerization [22] 6
Figure 4: (a) Synthesis of a sequential IPN and, (b) synthesis of a simultaneous IPN [30] 8
Figure 5: Idealized maleation of castor oil [137] 10
Figure 6: Maleation of castor oil via glycerolysis [37] 12
Figure 7: Stress-strain curves of PUs from OCP, CaCP, GCP, LCP and CCP [48] 15
Figure 8: Flexural strength of MACO-epoxy/fly ash composites [39] 16
Figure 9: Flexural modulus of MACO-epoxy/fly ash composites [39] 16
Figure 11: Average chemical composition of hemp fibres [67] 20
Figure 12: Average chemical composition of cotton fibres [67] 20
Figure 13: SEM image of the fracture surface of a hemp fibre reinforced composite (Reproduced from Sharma, et al.) [130] 21
Figure 14: SEM image of the fracture surface of carbon fibre reinforced epoxy composite [63] 21
Figure 15: Typical structure of an (a) untreated fibre and (b) an alkalized cellulosic fibre [64] 22
Figure 16: Formation of voids during different manufacturing methods [77] 26
Figure 21: Process of polymer degradation under aerobic and anaerobic conditions (Adapted from Leja and Lewandowicz [83]) 29
Figure 22: Equipment setup for the maleation of castor oil 31
Figure 23: Experimental setup for the copolymerization of MACO with styrene 33
Figure 24: W&W Mini-Vulcanizer vulcanization press used for curing 34
Figure 25: Sample geometry for Charpy impact test samples (units in mm) 37
Figure 26: Sample geometry of tensile test samples (units in mm) 37
Figure 27: Tabbing diagram for fibres (units in mm) 39
Figure 28: Sample geometry of flexural test samples (units in mm) 42
Figure 29: Acid value versus reaction time for the maleation of castor oil (adapted from Ghorui et al. [98]) 49
Figure 30: Trend in the acid value during the maleation of castor oil (reproduced from Mistri et al. [14] 49
Figure 31: Proposed reaction of MACO with styrene 51
Figure 32: Sheet of neat MACOPS matrix 52
Figure 33: Bubble gaps formed on surface of cured MACOPS matrix 52
Figure 34: Side view of bubble gaps on surface of MACOPS matrix 53
Figure 35: Sheet of MACOPS matrix reinforced with greige fibres 54
Figure 36: Impact strength comparison between the tested materials 55
Figure 37: Impact fracture of reinforced MACOPS (notch facing up) 56
Figure 38: Tensile stress-strain curves for neat MACOPS 57
Figure 39: Tensile fracture surface for neat MACOPS 58

Figure 40: Tensile stress-strain curves for general purpose polystyrene 58
Figure 41: Tensile fracture surface of general purpose PS 59
Figure 42: Tensile stress-strain curves for HIPS 60
Figure 43: Tensile fracture surface of HIPS 60
Figure 44: Stress-strain curves for reinforced MACOPS 61
Figure 45: Side-on tensile fracture surface of reinforced MACOPS 62
Figure 46: Tensile fracture surface of reinforced MACOPS 62
Figure 47: Comparison between different tensile stress-strain curves of representative samples 63
Figure 48: Flexural stress-strain curve for neat MACOPS 66
Figure 49: Flexural fracture surface of MACOPS 66
Figure 50: MACOPS showing a U-shape during 3-point bend testing 67
Figure 51: Flexural stress-strain curve for Reinforced MACOPS 68
Figure 52: Side-on view of delamination present in the reinforced MACOPS 68
Figure 53: Flexural stress-strain curves for general purpose polystyrene (PS) 69
Figure 54: Crazing near the flexural fracture surface of PS 70
Figure 55: Flexural stress-strain curve for high impact polystyrene (HIPS) 70
Figure 56: Flexural fracture surface of HIPS 71
Figure 57: Comparison between flexural stress-strain curves of representative samples 72
Figure 58: DSC thermogram for MACOPS 75
Figure 59: DSC thermogram for HIPS 76
Figure 61: TG thermogram and first derivative curve of MACOPS 77
Figure 62: TG thermogram and first derivative curve of reinforced MACOPS 78
Figure 63: TG thermogram and first derivative curve for GPPS 79
Figure 64: TG thermogram and first derivative curve for HIPS 80
Figure 65: (a) Water droplet on MACOPS surface and (b) an example of the contact angle analysis done by ImageJ 82
Figure 66: (a) Untreated fibre after removal of water droplet and (b) treated fibre after water droplet wetted surface of fibre 83
Figure 67: TEM micrograph of HIPS (Staining agent: OsO_4) 84
Figure 68: TEM micrographs of MACOPS (Staining agent: OsO_4) 85
Figure 69: FTIR spectrum of (a) MACOME and (b) MACOME and styrene co-polymer [119] 86
Figure 70: Overlayed Raman spectra of MACOPS and its components 87
Figure 71: Raman spectra of MACOPS 88
Figure 72: Raman spectra of GPPS 88
Figure 73: Raman spectrum of castor oil 89
Figure 74: Raman spectrum of maleated castor oil 89
Figure 75: Raman map of HIPS 90
Figure 76: Raman map of MACOPS 90
Figure 77: SEM image of the tensile fracture surface for reinforced MACOPS 91
Figure 78: View of the reinforced composite fracture surface at higher magnification 91
Figure 79: Temperature settings on the vulcanization press 106
Figure 80: Map of temperature profile points on vulcanization press heating plate 107
Figure 81: Temperature profile for low setting on vulcanization press 107

Figure 82: Temperature profile for medium setting on the vulcanization press 108
Figure 83: Temperature profile for the high setting on the vulcanization press 109
Figure 84: Tensile stress-strain curves for greige fibre 110
Figure 85: Tensile stress-strain curves for hemp fibre 110
Figure 86: Tensile stress-strain curves of degraded MACOPS.....111
Figure 87: Tensile stress-strain curves for degraded PS CD-case (negative control) 112
Figure 88: Tensile stress-strain curve for degraded reinforced MACOPS.....112
Figure 89: Contact angle of water droplet on original MACOPS 113
Figure 90: Contact angle of water droplet on degraded MACOPS 113
Figure 91: Contact angle of water droplet on original reinforced MACOPS 114
Figure 92: Contact angle of water droplet on degraded reinforced MACOPS (start).....114
Figure 93: Contact angle of water droplet on degraded reinforced MACOPS after (a) 1 minute and (b) 1 minute 30 seconds.....114
Figure 94: Contact angle of water droplet on the surface of untreated woven greige fibre.....114

LIST OF TABLES

Table 1: Typical physical properties of castor oil as reported by Patel et al. [12] 5
Table 2: Young's modulus and tensile strength of castor oil polyurethanes [42, 43, 44] 13
Table 3: Naming of vegetable polyols [48].....14
Table 4: Mechanical properties of polyurethanes based on polyols from different vegetable oils [48].....14
Table 5: Mechanical properties of bio-based thermoset polymers containing maleated castor oil glycerides [9].....17
Table 6: World annual production of commercially popular natural fibres [53] 18
Table 7: Properties of popular natural fibres.....18
Table 8: Comparison in weight between natural fibre reinforced composites and conventional composites used for automotive applications [59] 24
Table 9: Properties of cotton/PLA fibre reinforced composites [74] 25
Table 10: Tensile properties of the tested materials 63
Table 11: Mechanical properties of greige and hemp fibres with a cross-sectional area determined by measurement.....64
Table 12: Efficiency of fibre reinforcements.....65
Table 13: Flexural properties for the tested materials.....72
Table 14: Shore-D hardness for the tested materials 73
Table 15: Average densities of the different materials 73
Table 16: Specific strength of tested materials 74
Table 17: Comparison of thermal degradation properties of tested polymers 79
Table 18: Mass loss of tested materials after biodegradability tests 81
Table 19: Comparison of mechanical properties before and after biodegradability test 81
Table 20: Measured contact angles of the tested materials.....82

LIST OF SYMBOLS, CODES AND ACRONYMS

ABS	Acrylonitrile butadiene styrene/polybutadiene-graft-(poly(acrylonitrile-ran-styrene))
CaCP	Canola-castor oil-based polyols
CCP	Castor-castor oil-based polyols
CO	Castor oil
COMG	Castor oil maleated glycerides
DMA	Dynamic mechanical analysis
DSC	Differential scanning calorimetry
E	Epoxy
EF	Epoxy with fly ash
EM	MACO epoxy blend
EMETCO	Epoxidized methacrylated castor oil
GCP	Grape seed-castor oil-based polyols
GPPS	General purpose polystyrene
HIPS	High impact polystyrene
IPN	Interpenetrating polymer network
LCP	Linseed-castor oil-based polyols
MACO	Maleated castor oil
MACOME	Maleic acid-castor oil monoester
MACOPS	Maleated castor oil-polystyrene matrix
MLA	Methacrylated lauric acid
OCP	Olive-castor oil-based polyols
PAHU	Poly(amide-hydroxyurethane)
PLLA	Poly(L-lactide)
PMCs	Polymer matrix composites
PP	Polypropylene
PS	Polystyrene
PU	Polyurethane
RBF	Round bottom flask
SEM	Scanning electron microscopy
SIN	Simultaneous interpenetrating network
TEM	Transmission electron microscopy
Tg	Glass transition temperature
TG	Thermogravimetry
UTS	Ultimate tensile strength
UV	Ultraviolet
C_1	Crosslinker 1
C_2	Crosslinker 2
M1	Monomer 1
M2	Monomer 2
N1	Network 1
N2	Network 2

Chapter 1: Introduction

1.1 Background and motivation for this study

Although the chemical industry has made major improvements in efficiency and in the reduction of carbon dioxide emissions per kilogram product over the past five decades, sustainability is still a large concern [1]. The rapid increase in the world's population has led to an increase in the usage of plastic products, most of which are non-biodegradable. Winterton indicates the requirements for sustainability to be as follows [1]:

- *"…the supplies used to produce products in accordance to the needs of humans should not be depleted; and*
- *emissions caused by the production or disposal of products should have no negative impact on the environment…"*

These requirements can only be met if products are recycled or made out of renewable materials, preferably both. Emissions can be minimized through an extended product life or a decrease in harmful emissions by converting products into harmless substances [1].

To be able to negate the impact that these non-biodegradable products have on the environment, research into biodegradable alternatives is needed [2]. The need to find alternatives for materials based on petroleum precursors and using more renewable resources has driven this research [3]. By using biologically-based materials that do exclude materials used for food or animal feed, the dependence on fossil fuels can be dramatically decreased. The impact that fluctuating oil prices has on the economy can also be minimized by using biological alternatives [4]. These materials include wood wastes, non-food crops and grasses [5]. Vegetable oils like soybean, linseed and castor oil can be utilized in the development of polymers that can be used in polymer matrix composites (PMCs) [3]. Soybean oil is not suitable for use as it is edible. Its use would cause competition between the materials and food industry. Castor oil, on the other hand, is ideal for the materials industry as it is non-edible [6]. Polymers, created by the polymerization of vegetable oils, form part of the class known as biopolymers. Biopolymers can be defined, as by Imre and Pukánszky, as being based on renewable materials or being biodegradable or both [7]. For a polymer to be defined as biodegradable, it needs to be able to form products such as water and carbon dioxide when consumed by microorganisms in soil [8]. What sets castor oil-based polymers (or any other polymer synthesized from vegetable oils) apart from conventional polymers are the following factors [6]:

- these vegetable oil-based polymers are more affordable,
- the natural resources are readily available,
- the properties of the vegetable oil-based polymers are similar to those of conventional polymers, if not better, and
- some of these vegetable oil-based polymers are biodegradable, non-toxic and have a very low contribution to the production of greenhouse gases.

1.2 Objectives of this study

The objectives for this study were therefore:

- to conduct research on non-polyurethane biopolymers,
- to develop a maleated castor oil/polystyrene (MACOPS) polymer matrix, partially produced from a renewable feedstock,
- to reinforce the matrix with natural fibres, *viz.* woven cotton/hemp fibres,
- to determine the mechanical properties of the matrix as well as the reinforced composite. The mechanical properties of MACOPS matrices have not been reported in the literature,
- to compare these mechanical properties to those of pure polystyrene (GPPS) and high impact PS (HIPS), and
- to measure the biodegradability of the maleated castor oil/polystyrene matrix.

1.3 Scope and limitations of this study

The focus of this study was to synthesize a maleated castor oil/polystyrene polymer matrix. The mechanical properties were compared with general purpose polystyrene and high impact polystyrene (HIPS). These choice of these polymers was because the impact of modification of polystyrene was of interest. HIPS is once such modification, hence it was chosen as another reference point so that the changes that resulted from the modification could be gauged.

The synthesized matrix is not available commercially. The method of synthesis and its optimization was deemed beyond the scope of this studying. Varying mixing ratios of the reactants was not explored and the MACOPS polymer produced was made with one weight percentage (wt%) polystyrene. The ratios chosen were based on literature [9].

Reinforcement of the matrix was attempted to observe how the matrix reacts to reinforcements. Reinforcement was limited to cotton/hemp greige fibres in fabric form as these were readily available at a relatively low cost. Exploration of other reinforcing materials was deemed out of scope.

Mechanical properties that were measured were Charpy impact strength; tensile modulus, strength and toughness and flexural (3-point bending) modulus and strength.

Due to time constraints, the biodegradability testing could only run for a period of 10 weeks.

Chapter 2: Literature Review

2.1. Physical and chemical properties of castor oil and uses

Overview

Castor oil is a natural triglyceride containing numerous fatty acid triglycerides. The castor oil plant, seen in Figure 1(a), is found in tropical parts of Asia and Africa [10]. The beans (Figure 1(b)) of *Ricinus communis* (known as the castor oil plant from the Euphorbiaceae family [6]) can be pressed to obtain castor oil or it can be extracted using a solvent such as hexane [11]. A combination of the two processes can also be performed [12]. It has been found that the solvent extraction method yields the most oil and an increase in the temperature results in higher yields [12]. There are many advantages and disadvantages for each of these processes. Differences in the properties of the castor oil result, depending on the method used. Before the castor oil can be extracted, the castor oil seeds need to be prepared. The preparation of the seeds involves four main steps [10]:

1. clearing – separation of the beans from dirt and debris,
2. drying – splitting the casing of the beans and releasing the seeds,
3. winnowing – process of removing the seed casings, and
4. grinding – process of grinding the seeds into a paste to release the fatty acids triglycerides trapped inside the seeds.

A refining process is necessary after the extraction of the castor oil to remove small amounts of free fatty acids and other impurities [10].

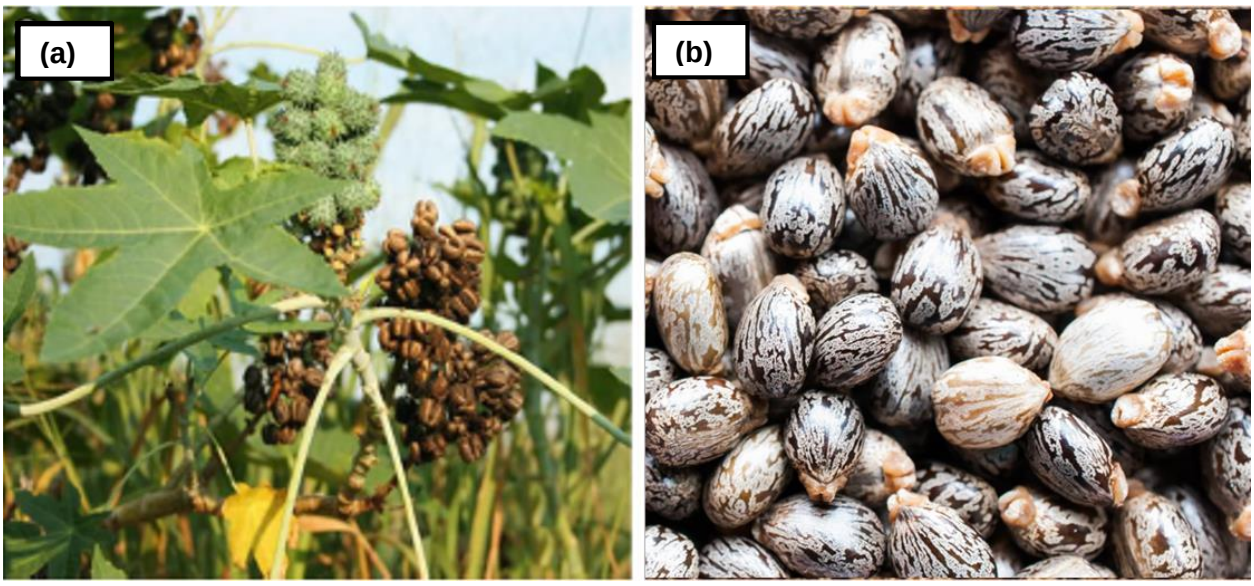

Figure 1: (a) Castor oil plant [6] and (b) castor beans [141]

Castor oil is insoluble in water [2], non-toxic and not suitable to be consumed as food [6]. This makes castor oil especially suited for use in polymeric materials as there is less competition between the polymer and the food industries [6]. Some competition remains but because castor oil can be grown on more marginal soils, less competition results than would be the case if oils such as sunflower or canola were used. Castor oil is used in industries such as biodiesel in the fuel industry, in the polymer industry, and for the production of soaps, waxes and greases as well as lubricants, brake fluids and fertilizers [12].

Chemical properties

The chemical composition of the castor oil does not depend significantly on the area or season in which it was grown [10]. Castor oil contains esters of six different fatty acids of which those of ricinoleic acid are the most abundant (87.5%) [2]. This is beneficial as ricinoleic acid has hydroxyl groups which form reactive sites for reactions such as halogenation, esterification and dehydration [12]. The reactivity of the carboxyl (ester), double bond and hydroxyl groups present in the chains of the ricinoleate esters enables castor oil to be used in the synthesis of many interesting materials [13]. The carboxyl groups allow the transformation of the castor oil via esterification or amidation whereas the presence of the double bond allows reactions like hydrogenation, carbonylation and epoxidation. In the instance where the hydroxyl group is removed by dehydration, the unsaturation of the oil is increased by forming a new double bond [6]. The structure of castor glyceryltriricinoleate is shown in Figure 2. In Figure 2 the ∆9-unsaturation of the castor oil can be seen. This means that the double bond is located nine carbons from the ester linkage.

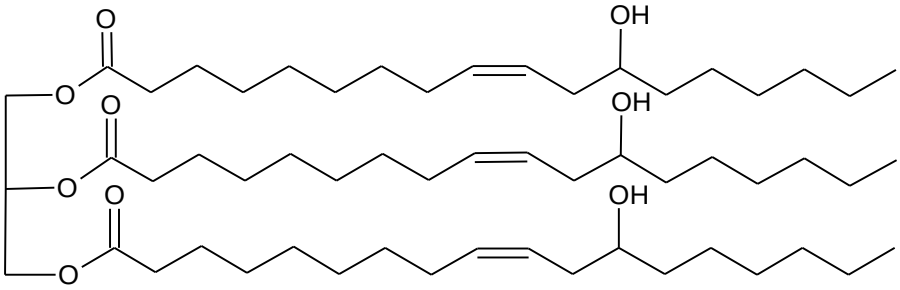

Figure 2: Chemical structure of glyceryltriricinoleate [143]

Physical properties

Patel et al. [12] summarize the most important physical properties of castor oil as seen in Table 1.

Table 1: Typical physical properties of castor oil as reported by Patel et al. [12]

Property	**Value**
Viscosity (centistokes)	889.3
Density (g/cm^3)	0.959
Thermal conductivity (W/m˚C)	4.727
Specific heat capacity (kJ/kg/K)	0.089
Flash point (˚C)	145
Pour point (˚C)	3
Melting point (˚C)	-2 to -5
Refractive index	1.480

2.2. Polymers synthesized by using castor oil and modifications of castor oil

Polymers are large molecules (also known as macromolecules) built up of many repeating units. Some desirable properties include good thermal stability, biodegradability, resistance to chemicals, biocompatibility, non-flammability, electrical conductivity and gas permeability [2]. The type of properties preferred depends on the application of the polymer.

Castor oil is a good candidate for polymerization as the long fatty acid side chains that are attached to a glycerol molecule can be lysed into smaller molecules. It is important when choosing a monomer to note if the monomer is non-toxic, relatively inexpensive, if the monomer is multifunctional and therefore able to form crosslinked networks and easily forms hydrolysable ester linkages through polycondensation reactions. Castor oil is a valuable source of biodegradable hydrocarbons [14]. Biocompatibility is also highly preferred [15]. Castor oil possesses these properties making it the ideal starting agent for many applications [16], especially polymer resins. Because castor oil contains three hydroxyl groups, it is known as a macro triol. This allows polymers to be generated with limited crosslink density, resulting in a material with high toughness [14].

Compared to conventional commodity polymers, biopolymers normally have poor material properties, especially Young's modulus and high viscosity, thus limiting applications. These properties can be improved by using techniques like blending, grafting, copolymerization and transesterification [7].

Esters

Maleated half esters can be formed by reacting castor oil (a hydroxylated triglyceride) with maleic anhydride or maleic acid [17, 18]. These maleated half esters can be cured by means of free radical polymerization. This results in a thermoset polymer [17].

Polyurethanes

The bulk of synthetic polymers produced from castor oil have been polyurethanes [19, 20]. Mosiewicki and Aranguren discussed the increase in reactive hydroxyl groups by means of hydrolysis. These modified oils can be used in polycondensation reactions together with isocyanates to produce polyurethanes [3]. In condensation reactions there is always a small molecule (e.g., water) that is eliminated after each step [21].

There are many variations in the process to synthesize polyurethanes and reinforcements can be added to produce PMCs. To make these polyurethanes environmentally friendly, alternatives for isocyanates should be found as these reactants are highly reactive, toxic and are produced from phosgene which itself is highly toxic and harmful to the environment [6]. Ruiz *et al*., investigated the synthesis of non-isocyanate polyurethanes. These were synthesized using 5 membered cyclic carbonates and amines. By using castor oil-based heptanal and carbon dioxide, activated disubstituted cyclic carbonate as well as an ester containing monomer was prepared. The product, poly(amide-hydroxyurethane) was produced by combining the highly reactive ester containing monomer and 1,6-diaminohexane. The reactions that took place were bulk ring opening polymerization as well as amidation polymerization. Figure 3 shows the bulk ring opening polymerization reaction. This was performed at low temperature and in the absence of a catalyst [22].

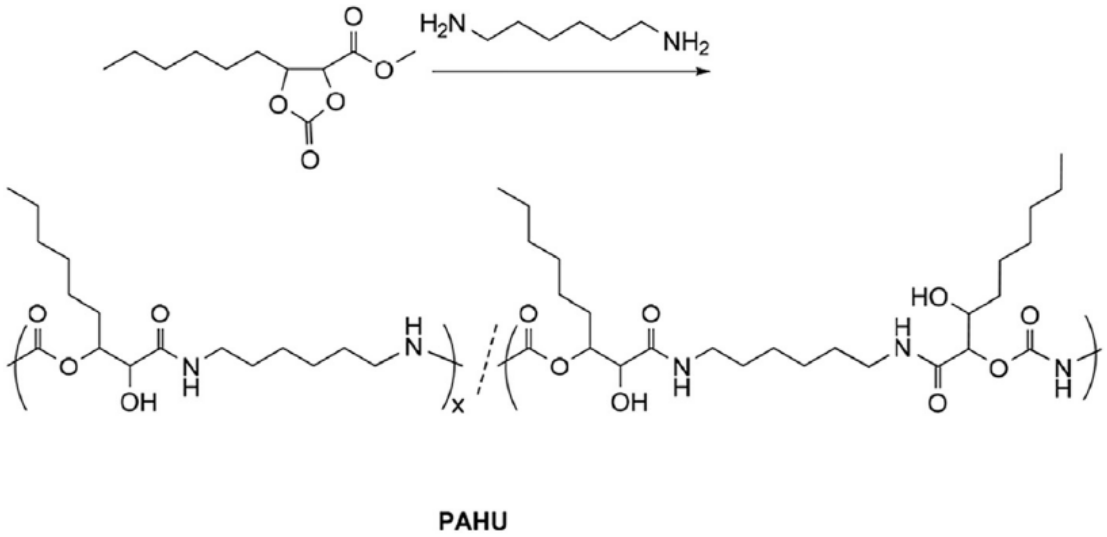

Figure 3: Synthesis of poly(amide-hydroxyurethane) through bulk ring opening polymerization [22]

Polyamides

Polyamides can be synthesized through the pyrolysis of castor oil. This reaction yields methyl undecylenate which can be converted to 11-aminoundecanoic acid. Condensation of this monomer results in the production of nylon-11 which is an engineering thermoplastic [23]. The

BASF Company also relaunched a polyamide (polyamide-6,10) derived from sebacic acid (in turn derived from castor oil) [10].

Polyesters

Sathiskumar and Madras synthesized castor oil-based biodegradable polyesters by means of catalyst free melt condensation polymerization. The reactants were two diacids, castor oil and D-mannitol. This resulted in a rubbery polymer with a hydrophilic surface. The polymer degraded in 21 days when an *in vitro* degradation test was conducted [15].

Co-polymers

Robertson *et al.* synthesized a diblock copolymer from poly(ricinoleic acid) and poly(L-lactide) (PLLA). A lipase-catalyzed condensation reaction was used to polymerize the ricinoleic acid, present in castor oil. The product contained a hydroxyl end-group that was used as an initiator in the ring opening polymerization reaction of the L-lactide. On its own PLLA is brittle in nature but using both these polymers in a block copolymer greatly increased the tensile toughness [24].

Çayli *et al*. co-polymerized epoxidized methacrylated castor oil (EMETCO) with acrylic acid, styrene and methacrylic acid [25]. To form EMETCO the castor oil was first methacrylated using methacryloyl chloride; thereafter the product was epoxidized by the Prilezhaeve reaction. The Prilezhaeve reaction is the reaction where an alkene is epoxidized by a peracid such as m-chloroperbenzoic acid [26]. The EMETCO can be used in various polymerization reactions as the production of a bio-based epoxy acrylate monomer [25]. Although this monomer is bio-based it is quite harmful to the environment due to the use of the Prilezhaeve reaction. Parada Hernandez *et al*. used a toxicity-free catalytic system consisting of H_2O_2, alumina and ethyl acetate. This catalytic system is considered to be environmentally friendly due to the fact that it is free of any heavy metals and toxic solvents [27]. Campanella *et al*. synthesized a co-polymer from a triglyceride derived crosslinker (for example castor oil maleated glycerides) with a co-monomer (in this case styrene). It was found that for this copolymer an increase in the amount of fatty acid esters resulted in a decrease of the glass transition temperature and stiffness of the co-polymer [9].

Interpenetrating polymer networks

Interpenetrating polymer networks (IPNs) form another system for which castor oil is known to be a suitable candidate – the reason being the presence of hydroxyl groups, capable of reacting with carboxyl groups as well as isocyanate groups in the case of polyurethanes [2]. The definition of an interpenetrating polymer network is a “polymer system that comprises of two or more networks, which are at least partially interlaced on a molecular scale but not covalently bonded” [28]. The strength of these IPNs are quite significant as the networks will only separate in the case where a chemical bond is broken, similar to the phenomena found in crosslinked polymers where failure is due to the breakage of bonds. The addition of an IPN formed by triglycerides (like castor oil) to conventional thermoset polymers was found to increase the conventional polymer’s toughness and resistance to fracture. One such IPN mentioned by Sharma and Kundu is that of crosslinked polystyrene and castor oil elastomers [28]. Suthar *et al.* produced an IPN using a castor oil-based

polyester and polymethylmethacrylate. The polyester was synthesized using a polycondensation reaction between castor oil and dibasic acids (like malonic or succinic acid) [29]. Nayak discussed two types of interpenetrating polymer networks: namely sequential IPNs and simultaneous interpenetrating networks (SINs). For the network to be classified as a sequential IPN, a crosslinked polymer (I) first needs to be prepared followed by swelling in the monomer components of the second network (II), where after monomer II is polymerized *in situ* [23]. SINs require mixing of all components at an early stage. The networks are then formed via different reaction pathways, all in the same container [23].

Sperling and Manson illustrate the synthesis of the two types of interpenetrating polymer networks. For the synthesis of the sequential IPN as seen in **Error! Reference source not found.** a), a network (N_1) is produced when the monomer (M_1) and crosslinker (C_1) is polymerized. Monomer 2 (M_2) and crosslinker 2 (C_2) are then swollen into N_1 where after it is polymerized to make the IPN consisting of N_1 and N_2. The synthesis of the simultaneous IPN on the other hand has the swelling and polymerization step in one. This results in N_1 and N_2 being interpenetrated [30].

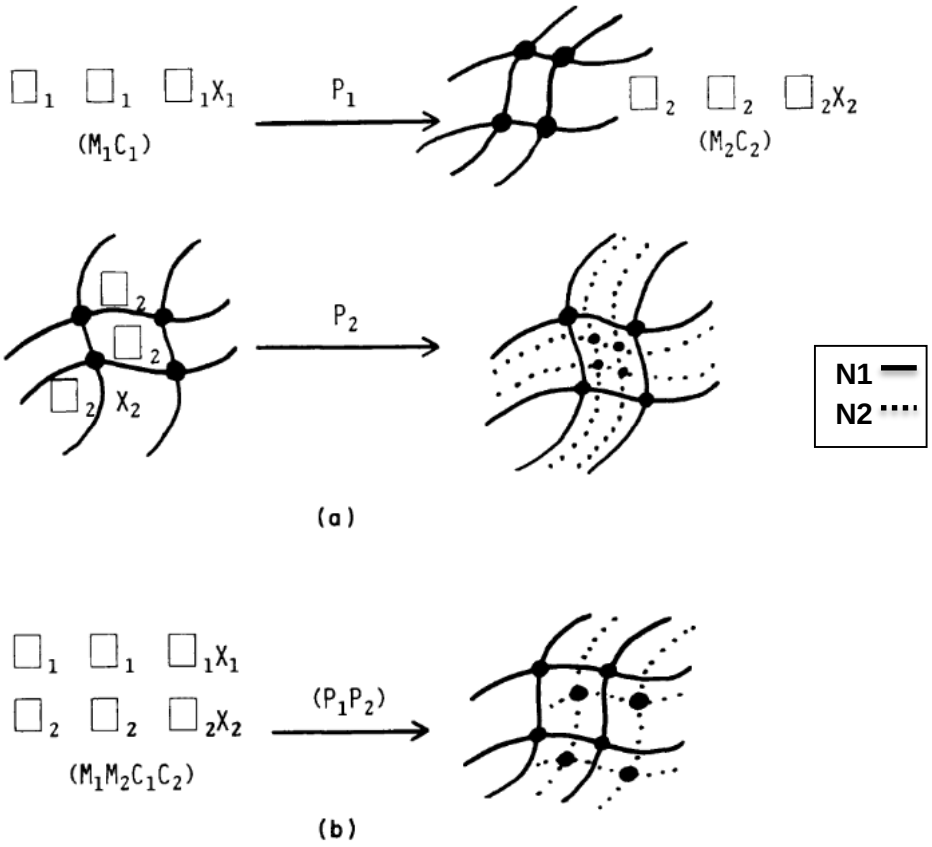

Figure 4: (a) Synthesis of a sequential IPN and, (b) synthesis of a simultaneous IPN [30]

Raymond and Bui prepared an IPN using a polyurethane based on castor oil and an epoxy matrix. The networks were synthesized in a sequential manner. They also found by means of scanning electron microscopy that the IPN samples had a homogenous morphology. This could have been

due to grafting of the castor oil-based polyurethane phase onto the epoxy matrix as the cyanate functional groups of the polyurethane can react with the hydroxyl groups present in the epoxy matrix [31].

Others

Other methods of modification include the hydrogenation of castor oil. Hydrogen can be added to the oil in the presence of a Ni or Pd catalyst. This forms saturated 12-hydroxystearic acid in the semi-solid phase. The saturated monomer can be used in the manufacture of resins or polymer mixtures. As the product is insoluble in water it is also used for lubricants, coatings and paints [6].

2.3. Methods of maleation

During the chemical reaction of castor oil with maleic anhydride, castor oil maleate is produced [32]. Castor oil glycerides on the other hand are produced by the glycerolysis of castor oil. These can also be obtained from the glycerolysis of the methyl ester derivatives of castor oil. The methods used for the production of maleated castor oil or maleated castor oil glycerides by different researchers show many similarities in terms of reaction conditions and molar ratios.

Echeverri *et al.* produced castor oil glycerides by the glycerolysis of castor oil. The reaction took place under an inert atmosphere, created by purging the reaction flask with nitrogen. The castor oil was heated up to a temperature in the range of 180 – 220 ˚C where after crude glycerol was added. After completion of the reaction a small amount of H_2SO_4 in water was added to neutralize the catalyst. The mixture was cooled to 100 ˚C in order for the catalyst and excess glycerol to separate out. The castor oil glycerides were then mixed with maleic anhydride. For optimum conversion of castor oil glycerides to maleated castor oil glycerides, the mixture was magnetically stirred for 5 hours at a temperature of 90 ˚C. The reaction was stopped by placing the reaction flask in cold water [33].

Maleated castor oil was obtained by Saied *et al.* by the reaction of castor oil with maleic anhydride (mole ratio of 1:3). The castor oil and maleic anhydride together with 0.012 wt% hydroquinone (acting as an inhibitor for side reactions) were heated to 90 ˚C. At this temperature the maleic anhydride melted and 0.12 wt% N,N-dimethyl benzylamine (acting as an accelerant) was added. The reaction temperature was stabilized at 98 ˚C and kept there for 5 hours [34].

Wang *et al.* created biodegradable foam plastics from castor oil. Maleated castor oil (MACO) was synthesized (Figure 5) by the addition of maleic anhydride to castor oil (mole ratio of 2.5:1). This reaction was conducted under an inert atmosphere by purging with nitrogen. The reaction mixture was heated to temperatures between 85 – 130 ˚C. Foams were synthesized by means of free radical initiated co-polymerization between the maleated castor oil and a monomer, styrene [35]. A similar process but with a higher maleic anhydride: castor oil ratio (4.5:1) was used by Sahin *et al*. [36]. In Sahin *et al*.'s case, the MACO was epoxidised with formic acid/H_2O_2 before being co-polymerized with styrene (30 wt%) [36].

Another method of maleation is a two-step process. Firstly the castor oil underwent glycerolysis to form castor oil glycerides. The castor oil glycerides were then maleated in a separate reaction. During the glycerolysis reaction, the mole ratio used was 1: 2.4 of castor oil (based on gliceryltriricoleneate) to glycerol. Maleation was then performed by combining the product of the glycerolysis reaction with maleic anhydride and hydroquinone. The molar ratio of OH-groups (present in castor oil) to maleic anhydride was 3:10. The maleation reaction mixture was heated to 90 ˚C, whilst stirring continuously, and kept at that temperature until the maleic anhydride melted. The temperature was stabilized at 98 ˚C and N,N-dimethylbenzylamine was added. The mixture was kept at this temperature for 5 hours. The maleated castor oil glycerides were used in a co-polymerization reaction with styrene and methacrylated lauric acid respectively [9].

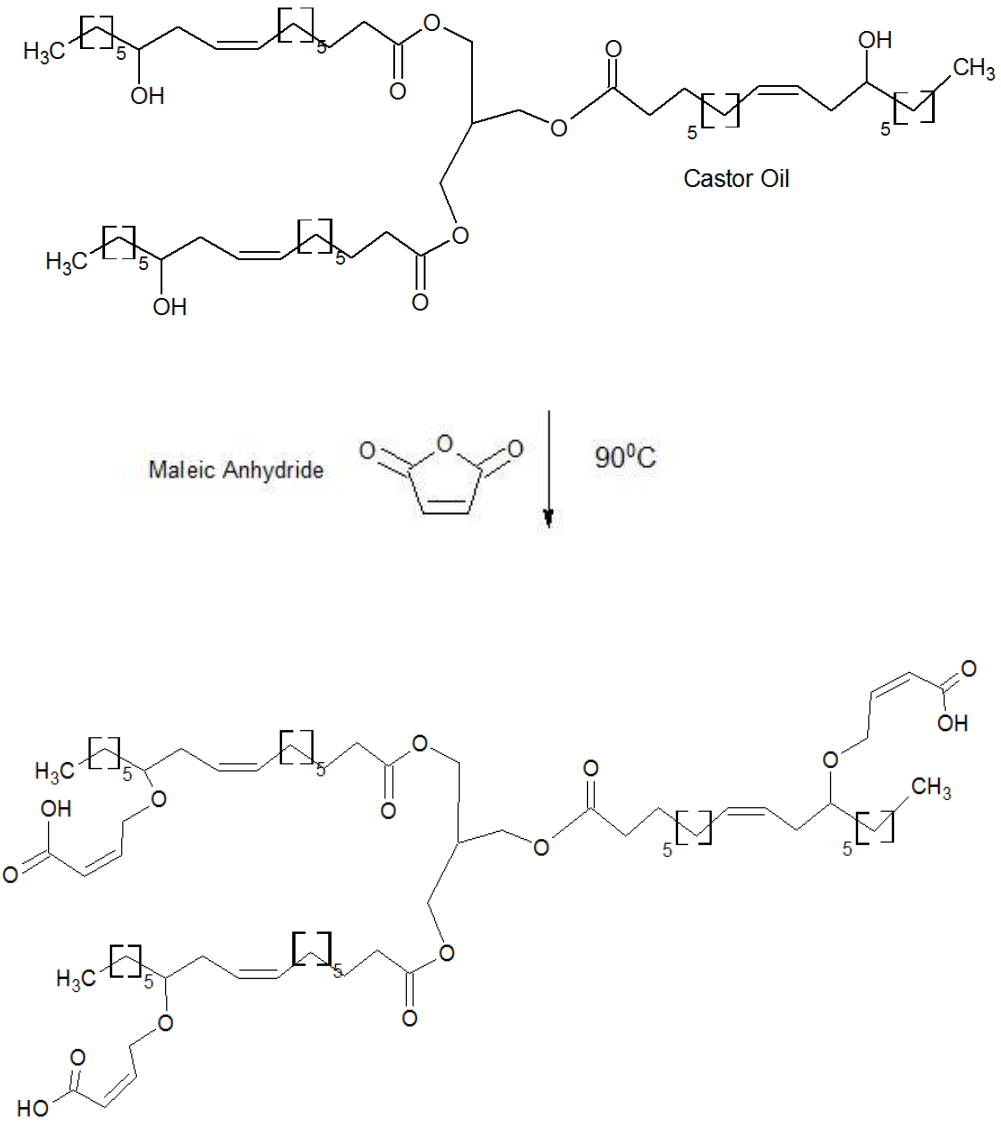

Figure 5: Idealized maleation of castor oil [137]

In another experiment, Echeverri *et al.* synthesized maleated castor oil glycerides by firstly completing a glycerolysis reaction of castor oil, followed by a maleation reaction [37] as shown in Figure 6. The maleated castor oil glycerides were synthesized using the same method as Echeverri and co-workers used in their previous paper [33].

Wang *et al.* synthesized maleated castor oil by dissolving maleic anhydride in castor oil, using a mole ratio of 2.5:1. The mixture was purged with nitrogen to create an inert atmosphere and the reaction continued for approximately 5 hours under reflux at a temperature of 120 ˚C. The reaction was deemed complete when the acid number of the product was lower than 120 mgKOH/g [38].

Ray *et al.* mixed castor oil and maleic anhydride (mole ratio of 1:3) were mixed and stirred continuously at a temperature of 125 ˚C for two and a half hours. The researchers stated that the reason for the choice of reaction time was due to the fact that the acid value of the maleated castor oil was the highest at this point in time. This means that the maleated castor oil will be able to take part in condensation reactions thereafter and will not dimerize [39].

Another method used maleic anhydride and castor oil in a mole ratio of 3:1 but the process differs slightly. Castor oil and xylene (weight ratio of 1:1) were added to a flask and heated to 140 ˚C. Maleic anhydride was added in increments. The reaction time was five hours and the mixture was stirred at a speed of 300 rpm. After the reaction was completed the xylene was removed by means of vacuum distillation [40].

Maia *et al.* synthesized castor oil maleate by means of two different synthesis pathways, an autocatalyzed thermal reaction and a free radical reaction. The autocatalyzed thermal reaction used a molar ratio of 1:1 for the castor oil and maleic anhydride. This is due to the fact that an excess of maleic anhydride will not decrease the reaction time or increase the yield. Different temperatures in the range of 63 – 176 ˚C and reaction times of 15 – 180 minutes were used to determine the kinetics of the reaction. For the free radical reaction Maia *et al.* used a castor oil to maleic anhydride ratio of 1:1. Benzoyl peroxide was added as an initiator. It was found that adding 0.015 w/wt% of initiator at a temperature of 160 ˚C ensured a maximum yield of 92% [32].

Indrajati *et al.* used a varying ratio of castor oil and maleic anhydride and added a fixed ratio of xylene to the mixture (1 castor oil:1 xylene in weight). A Dean Stark apparatus was used together with a cold water condensor. The maleic anhydride was added in increments whilst stirring continuously for 5 hours at a speed of 300 rpm. Vacuum distillation was used to remove the xylene after the reaction was completed [41].

Mistri *et al.* simply maleated castor oil by mixing maleic anhydride with castor oil (3:1 ratio) in a round bottom flask without any catalyst. The mixture was kept at a temperature of 125 ˚C for 4 hours with continuous stirring [14].

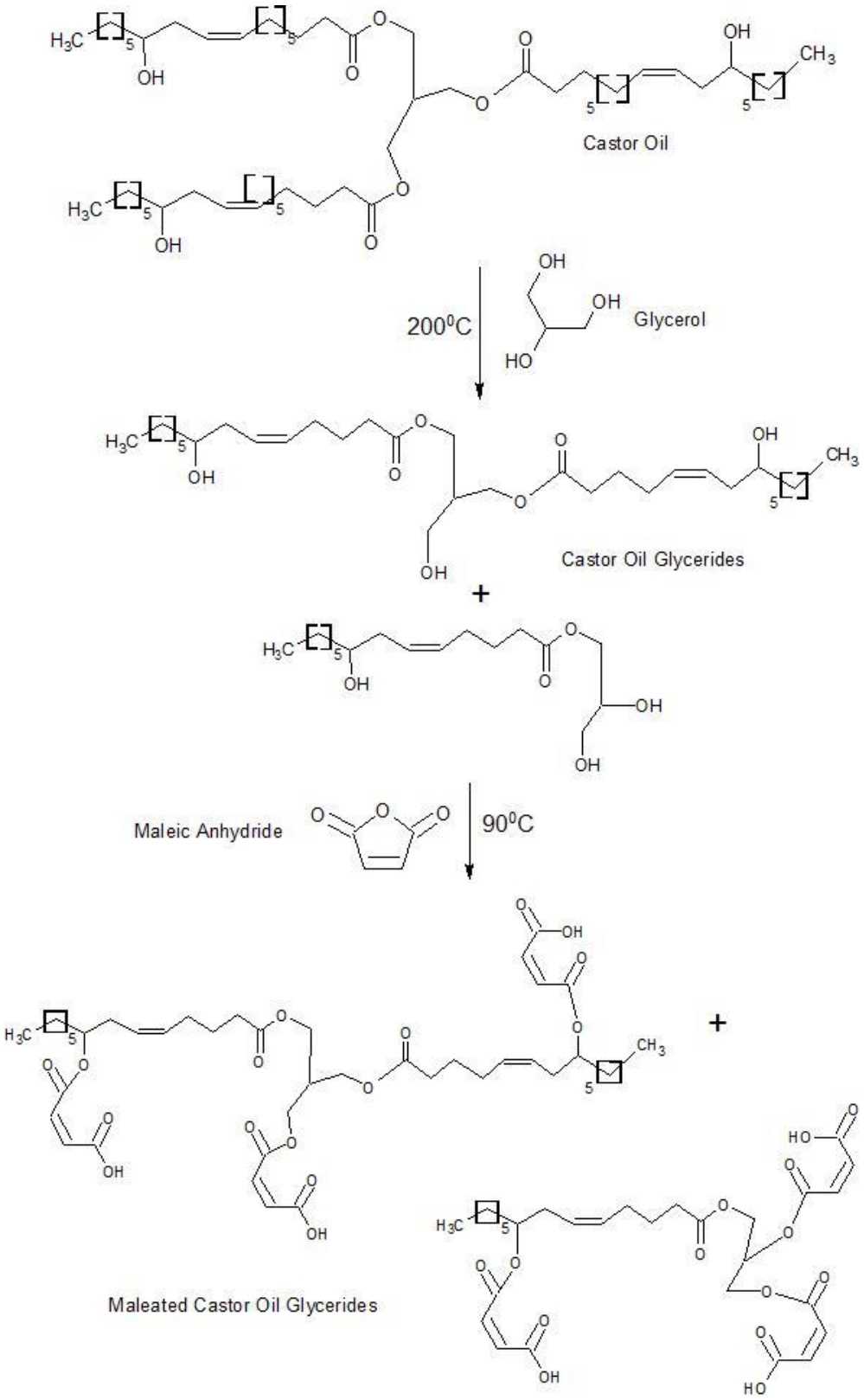

Figure 6: Maleation of castor oil via glycerolysis [37]

2.4. Properties of castor oil polyurethane composites versus maleated castor oil composites

Fibre-reinforced composites have been reviewed by Mosiewicki and Arungeren [3].

Castor oil polyurethanes

In the review by Mosiewicki and Aranguren a few examples were given of polyurethanes synthesized from castor oil containing different fibres [3]. Reported elastic moduli (Young's moduli) and tensile strengths are provided in Table 2.

The addition of treated banana fibre to a castor oil-based polyurethane elastomer resulted in an increase in modulus (from 6 to 54 MPa). This is due to the fact that treated fibres ensures better chemical and mechanical interactions at the matrix-fibre interface [42].

Table 2: Young's modulus and tensile strength of castor oil polyurethanes [42, 43, 44]

Polymer matrix	Fibre	Percentage	Process	Tensile Modulus (GPa)	Tensile Strength (MPa)
Castor oil (PU)	Banana fibre	0	Hand-lay up	0.006	1.96
		15 (vol. %) untreated		0.051	4.80
		15 (vol. %) NaOH treated		0.054	10.1
Castor oil (waterborne PU)	Nanocellulose	0	Casting	0.001	5.42
		4		0.005	8.09
Castor oil (PU from alcoholyzed oil)	Nanocellulose	0	Casting	0.480	27.6
		0.5		0.636	19.2
		1		0.680	31.2

Note that the percentages are weight percentages unless stated otherwise

Microcrystalline cellulose reinforced castor oil polyurethanes have been reported by Miao *et al.* [45]. A five times increase in tensile strength was noted after cellulose addition. Nanocrystalline reinforcement of castor oil polyurethanes was used by Gao *et al.* [46]. Other authors who used cellulose to reinforce castor oil polyurethanes include Maafi *et al*. [47] and Wik *et al*. [43].

Zhang *et al.* [48] used different vegetable oils to create bio-based polyurethanes. The different vegetable polyols that were synthesized, are named as follows:

Table 3: Naming of vegetable polyols [48]

OCP	Olive-castor oil-based polyols
CaCP	Canola-castor oil-based polyols
CCP	Castor-castor oil-based polyols
GCP	Grape seed-castor oil-based polyols
LCP	Linseed-castor oil-based polyols

By conducting tensile tests, the mechanical properties of the different polyurethanes made with their respective polyols were determined. A summary of the mechanical properties can be seen in Table 4. The stress-strain curves (generated from tensile test data) of the polyurethanes based on vegetable oil polyols are shown in Figure 7. It is clear from the stress-strain curves of PU-OCP, PU-CaCP and PU-GCP that they show properties of an elastomeric polymer, *viz.* a large elastic region, near 100% in elongation. PU-LCP and PU-CCP on the other hand have stress-strain curves similar to those of thermoplastics that undergo strain softening and strain hardening before reaching the breaking point respectively [48].

Figure 7 illustrates that PU-CCP shows high strength under tensile load but the amount of elastic deformation that took place was not significant.

Table 4: Mechanical properties of polyurethanes based on polyols from different vegetable oils [48]

Polyurethane	Tensile strength (MPa)	Young's modulus (MPa)	Elongation at break (%)	Toughness (MPa)
PU-OCP	0.4 ± 0.1	0.8 ± 0.1	79.2 ± 7.1	0.16
PU-CaCP	1.7 ± 0.4	2.2 ± 0.2	96.7 ± 15.6	1.06
PU-GCP	3.7 ± 0.6	5.5 ± 0.7	96.8 ± 17.7	2.33
PU-LCP	17.3 ± 3	197.3 ± 6.2	98.0 ± 12.9	10.15
PU-CCP	29.1 ± 4	495.3 ± 41.9	11.0 ± 0.2	2.84

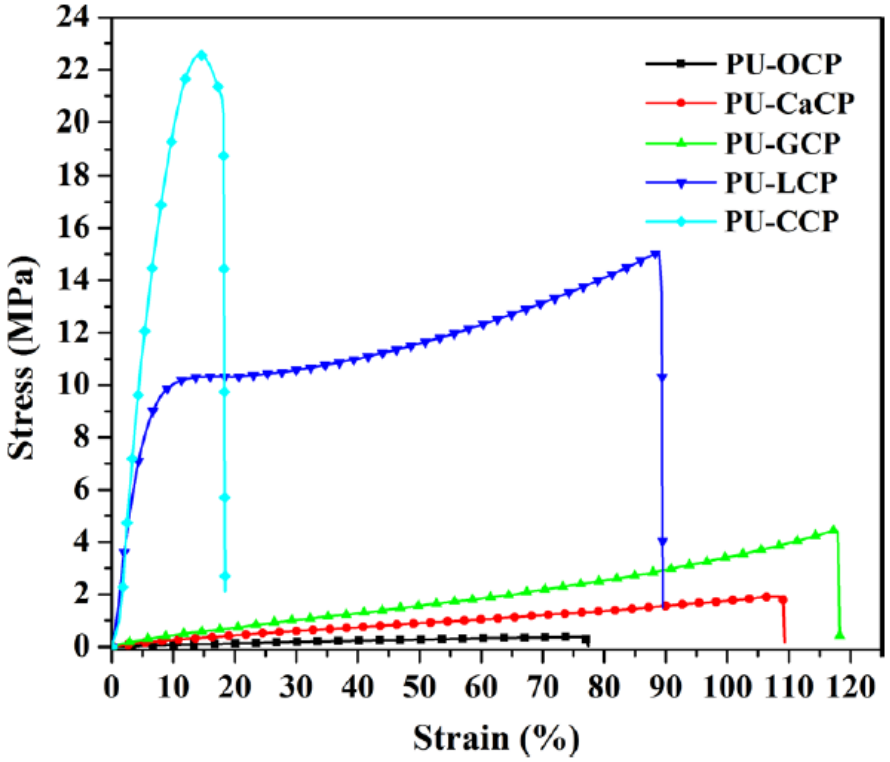

Figure 7: Stress-strain curves of PUs from OCP, CaCP, GCP, LCP and CCP [48]

Other castor oil polyurethane reinforcements include nanoclay [44] and carbon nanotubes [49].

Maleated castor oil composites

Very few composites made from maleated castor oil have been reported. Ray *et al.* synthesized MACO-epoxy/fly ash composites and tested the properties thereof. The flexural strength of the composite was firstly considered. The epoxy (E), epoxy with fly ash (EF) and the MACO epoxy blend (EM) yielded approximately the same flexural strength. The MACO-epoxy/fly ash composite on the other hand showed a significant decrease in flexural strength of approximately 25 MPa as seen in Figure 8. This was ascribed to the fact that the addition of maleated castor oil causes an increase in the hydrophobicity of the matrix thus reducing the amount of interactions on the interface of the fly ash particles between the fly ash particles and the matrix. EM showed a decrease in flexural modulus (Figure 9), indicating that the addition of maleated castor oil increases the flexibility of polymers [39].

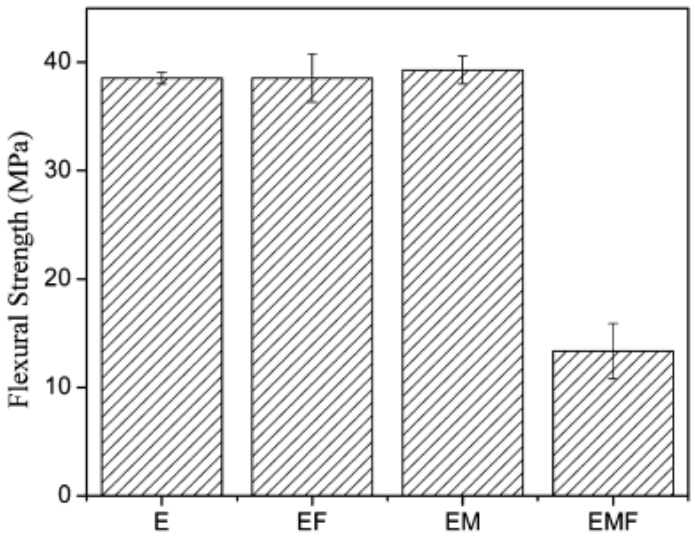

Figure 8: Flexural strength of MACO-epoxy/fly ash composites [39]

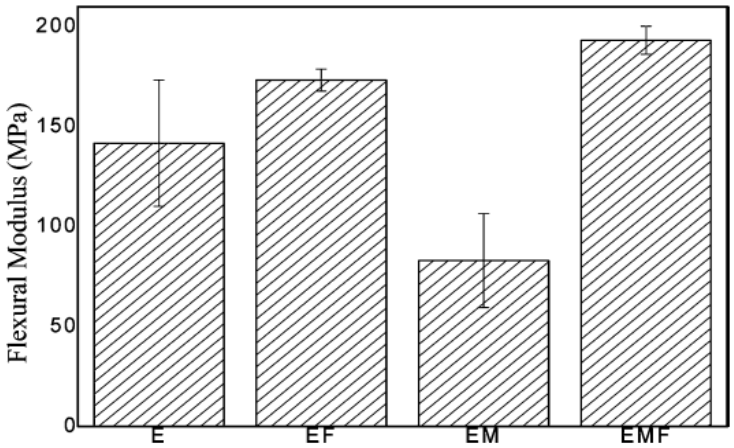

Figure 9: Flexural modulus of MACO-epoxy/fly ash composites [39]

Bio-based thermoset polymers created by Campanella *et al.* showed interesting mechanical properties. Copolymers of maleated castor oil glycerides with styrene and methacrylated lauric acid (MLA) respectively were produced [9]. The properties obtained were as follows:

Table 5: Mechanical properties of bio-based thermoset polymers containing maleated castor oil glycerides [9]

Copolymer	T_g (˚C)	E' (MPa)[a]	ν (mol/m³)	η (Pa.s)[b]
COMG + Styrene	121 ± 7.1	1955 ± 60.4	1.72 x 10^3	0.39 ± 0.03
COMG + MLA	62 ± 3.5	420 ± 6.2	4.8 x 10^2	1.89 ± 0.21

*Note that the amounts of styrene and MLA added were equal (35 wt%)

[a] 5 wt% of butyrated lignin added with respect to total content of resin

[b] At a temperature of 25 ˚C

A homopolymer of MLA would have a glass transition temperature (Tg) of approximately -34 ˚C and polystyrene a Tg of 100 ˚C [9]. Thus co-polymerization with maleated castor oil glycerides increased the glass transition temperature (as seen in Table 5), making the polymer less flexible. The COMG-styrene copolymer has a higher storage modulus than the copolymer with MLA (as seen in Table 5). It can be deduced that the styrene containing copolymer has a higher mechanical rigidity than the MLA containing copolymer. Considering the crosslink densities of the two copolymers, the rigidity of the COMG-styrene copolymer is consistent with its high crosslink density. The fact that the COMG-MLA copolymer has a higher viscosity makes it less suited for liquid molding manufacturing processes such as injection molding [9].

2.5. Natural fibre reinforcements

Overview

Natural fibre reinforced composites consist of a matrix and a bio-based reinforcing phase. The matrix is known as the binding phase which acts as a load transfer medium between the matrix and reinforcement while the reinforcing phase can be anything from fibres to particulates and whiskers [50]. Different conditions can be used to change the properties of the natural fibres. These conditions can include the treatment of fibres with chemicals or the formation of hybrids with other synthetic fibres [51].

Popular fibres that are produced and sold commercially are cotton, jute, flax, sisal, hemp, coir, ramie and kenaf fibres. Table 6 shows the annual production in tons of natural fibres globally. Natural fibre reinforcements are mostly used for the reinforcement of interior parts of vehicles where moisture levels are minimal [52].

Table 6: World annual production of commercially popular natural fibres [53]

Fibre Type	World annual production (10^3 tons)
Cotton	18 500
Jute	2 500
Flax	810
Kenaf	770
Sisal	380
Hemp	215
Coir	100
Ramie	100

The density of natural fibres are quite similar as seen in Table 7, whereas the tensile strengths differ quite significantly.

Table 7: Properties of popular natural fibres

Property	Hemp	Flax	Sisal	Jute	Cotton
Density (g/cm^3) [54, 55]	1.48	1.40	1.33	1.46	1.21
Modulus (GPa) [54, 55]	70	60-80	38	10-30	6-10
Tensile strength (MPa) [54, 55]	550-900	800-1500	600-700	400-800	287-597
Elongation to failure (%) [54, 55]	1.6	1.2-1.6	2-3	1.8	2-10
Specific modulus (kNm/g) [56]	41	50	17	42	-
Specific strength (Nm/g) [56]	20	33	6	14	-

Some of the advantages of using natural fibres instead of synthetic fibres, include:

- natural fibres are renewable,
- natural fibres are less expensive than most synthetic fibres,
- biodegradability,
- low density (in comparison with carbon fibres),
- relatively good mechanical properties [57],
- non-abrasive (lower tooling costs) [58],
- have a higher fibre content for equivalent performance, resulting in a reduction of the use of a polluting polymer matrix, and

- the carbonization of natural fibres result in the recovering of energy and carbon credits [59].

Although there are many advantages for the use of natural fibres in composites, disadvantages like the incompatibility between the matrix and fibres and poor moisture resistance often cause a reduction in the potential of these natural fibres. Other drawbacks can be the incompatibility of the natural fibres with a polymer matrix due to the hydrophobicity of the polymer, the formation of aggregates by the fibres and the thermal stability of the fibres [57]. These drawbacks are the major challenges that are faced when working with natural fibre reinforced composites.

The mechanical properties or performance of natural fibre polymer composites are influenced by a number of factors, which include [51, 52, 60]:

- fibre (type, long or short fibres, orientation, *etc*.),
- matrix (thermoplastic or thermoset),
- interface between the matrix and fibres,
- method used for fibre extraction from plant material, and
- method of fabrication used for the production of woven mats, *etc*.

Manikandan *et al.* have stated that the performance or mechanical properties of composites are improved when they are reinforced with continuous or woven fibres [52]. A fibre can be defined as woven if it is manufactured by interlacing fibre bundles (yarn) to form a layer. Apart from the increase in performance caused by using woven reinforcements, a high packing density and exceptionally good dimensional stability is also obtained [61].

Natural fibres, themselves, can be viewed as reinforced materials, with cellulose fibre being the reinforcement. The cellulose fibres consist of microfibrils that run along the length of the fibre. The matrix in this case is amorphous and consists of lignin and hemicellulose [57]. Average chemical composition of the natural fibres being used in this research project (hemp and cotton) can be seen in Figure 10 and Figure 11 respectively.

It is important to consider that the hemicellulose in the fibres is responsible for multiple problems. Some of these problems are biodegradation, absorption of moisture and thermal degradation. Lignin on the other hand is responsible for UV degradation [58]. When these fibres degrade, the process can lead to odours, discoloration of the composite, release of volatiles and inevitably the deterioration of mechanical properties [54].

Failure modes that can be expected in fibre reinforced composites include, cracking of the matrix, fibre breakage, debonding, fibre pull-out and delamination [62]. An example of fibre pull-out can be seen in Figure 12. The fibres are seen protruding out of the matrix. Cracking of the matrix is also visible. Figure 13 also shows signs of fibre pull-out and matrix debonding. Matrix debonding is seen where a gap is formed between the fibre and the matrix.

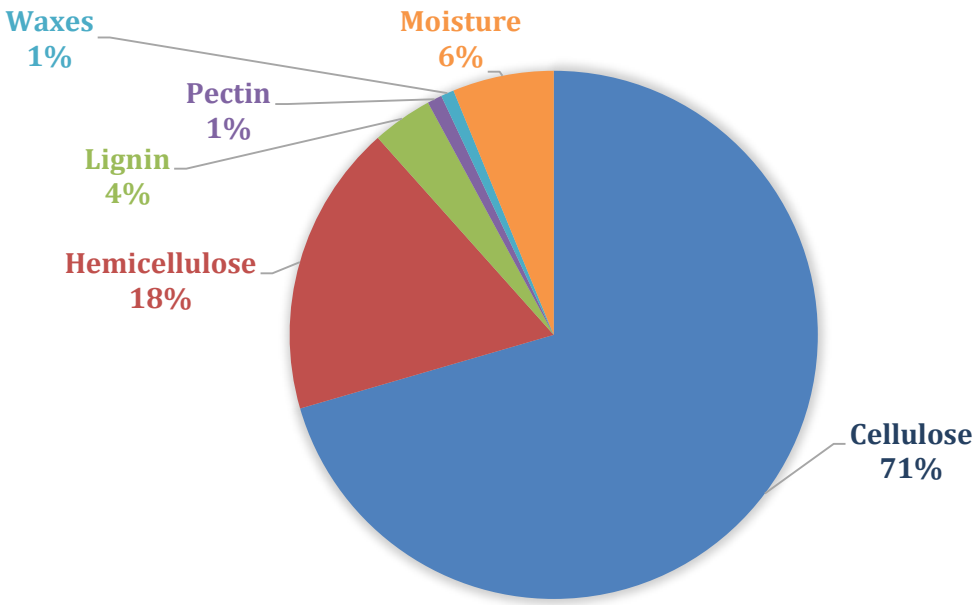

Figure 10: Average chemical composition of hemp fibres [67]

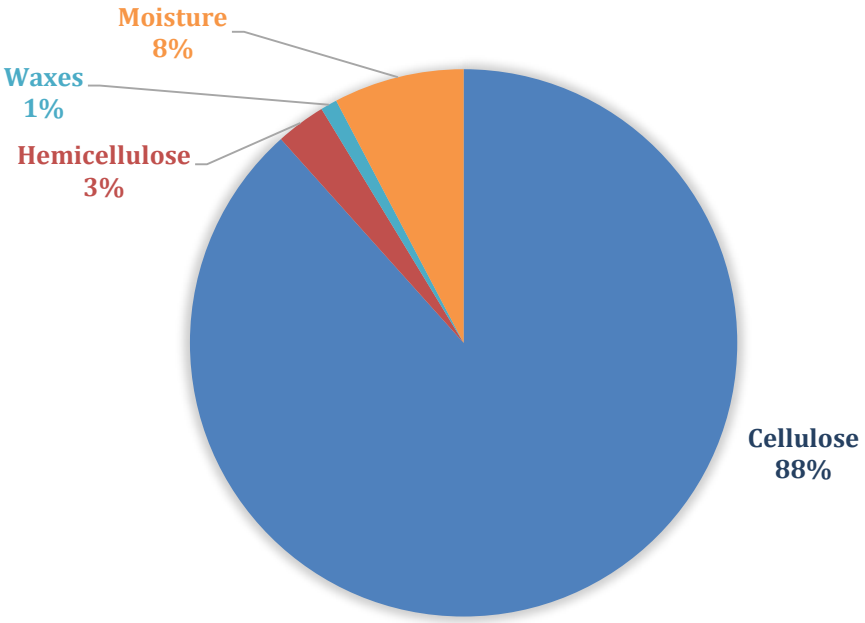

Figure 11: Average chemical composition of cotton fibres [67]

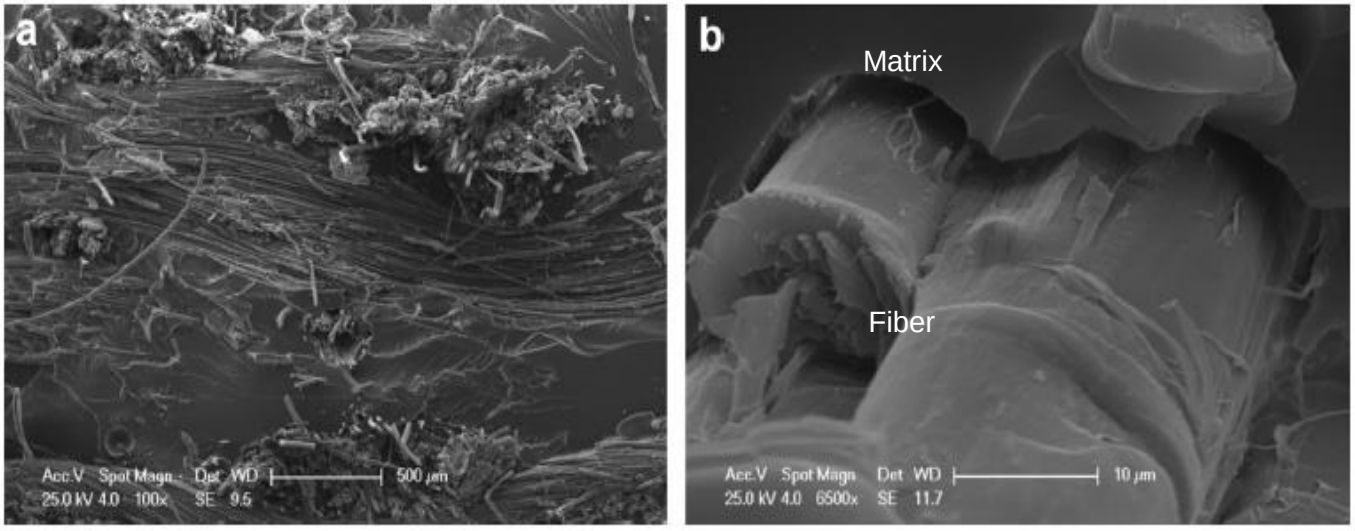

Figure 12: SEM image of the fracture surface of a hemp fibre reinforced composite (Reproduced from Sharma, et al.) [130]

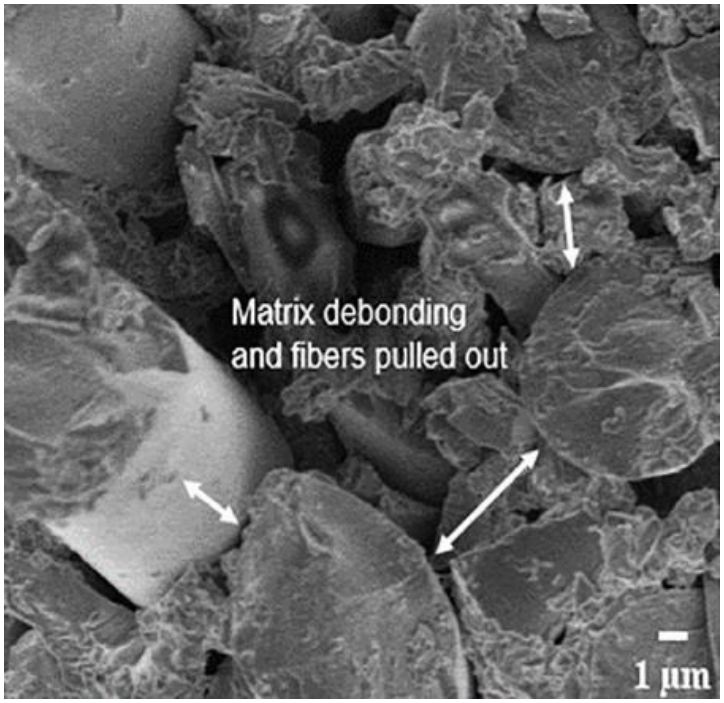

Figure 13: SEM image of the fracture surface of carbon fibre reinforced epoxy composite [63]

Modification of natural fibres by alkalization

When polar polymers are used for the matrix, the hydrogen bond formation between the polymer and the polar natural fibres can be difficult if the fibres are coated with pectin, lignin, natural oils

or other waxy substances [64]. In Figure 14 (a) the coating of the fibre surface with wax and oil is seen in the untreated fibre. Large amounts of lignin and long cellulose chains are present. For this reason, treatment is necessary to increase adhesion between the fibres and the matrix. After treatment the wax and oil particles are mostly removed, the amount of lignin has decreased and the long cellulose chains are lysed into smaller chains or molecules (as seen in Figure 14 (b)).

The most common treatment for natural fibres is alkalization. During the alkalization process the fibres are soaked in a sodium hydroxide solution to remove any impurities or unwanted substances (including lignin, waxes and oils).

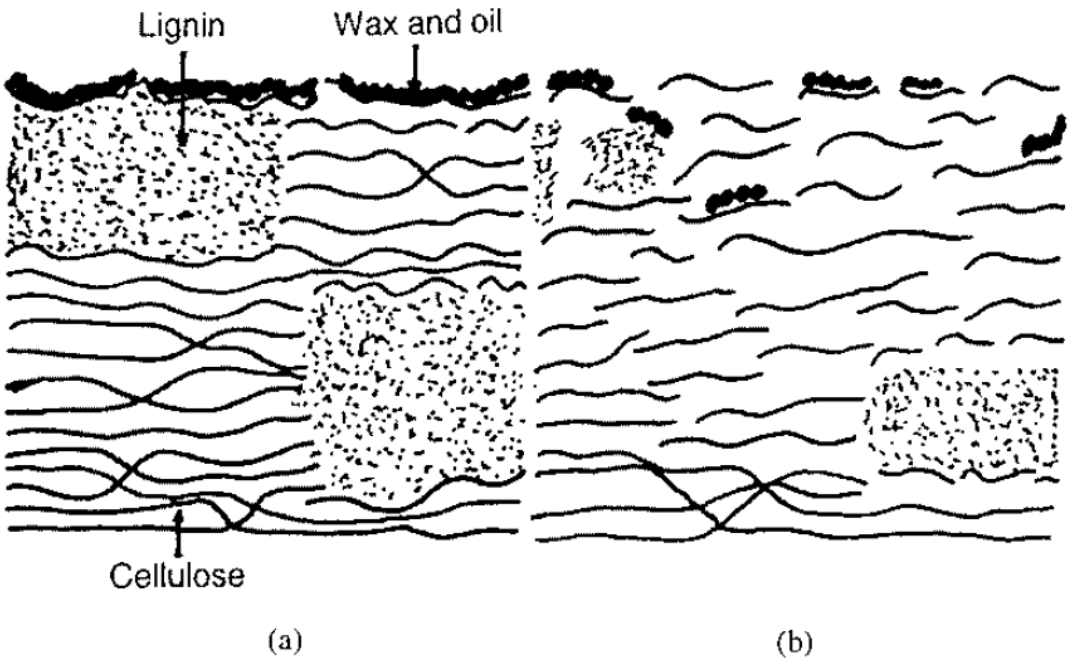

Figure 14: Typical structure of an (a) untreated fibre and (b) an alkalized cellulosic fibre [64]

Fibre reinforcements in automotive applications

Manufacturers in the automotive industry focus mainly on end-of-life recycling to minimize the amount of waste at disposal. New materials need to be developed to increase the overall recyclability of automotive vehicles [56].

Fibre reinforced composites can be used in multiple parts of automotive vehicles. These include body, chassis and engine parts. Examples of exterior body components include the hood and body panels. Currently polyester or vinyl ester resin reinforced with E-glass fibres are used for the manufacturing of exterior body parts. Other composite materials used include polypropylene reinforced with hemp, flax or sisal fibres [56]. A “Class A” surface finish is required for these parts as this will influence the value of the automotive vehicle.

For underbody components excellent surface finish is not necessary. Examples of these components are roof frames, door frames and engine valve covers. Sheet molding is used for the manufacture of these components which results in a decrease in tooling cost of 40-60% in comparison with the cost of stamping steel parts [54]. Another advantage of the use of composites instead of conventional metals is a decrease in the weight of the vehicles. This in turn leads to a decrease in fuel consumption and thus a decrease in pollution due to lower carbon dioxide emissions [56].

Components where natural fibre reinforcements are mostly used are inner door panels, seat backs and inner roof panels [54]. A major disadvantage for most manufacturers is the inconsistency in properties of natural fibre reinforced composites. Factors like harvest time, climate, processing of the soil and the processing of fibres all influence the final properties of the natural fibres [65]. All these factors make producing natural fibre reinforced composites with consistent properties very difficult.

Hemp fibre

The use of hemp (*Cannabis sativa)* fibre reinforcement is attractive to the automotive industry due to the low cost thereof and hemp fibre's low density [59]. It also meets the biodegradability standard for waste treatment and can thus be used as reinforcement in the interior components of automotive vehicles. Despite the attractive properties of hemp fibres, it is still mostly used in the textile industry [66].

The estimated density of hemp fibres is 1.45-1.48 g/cm^3 [54, 55, 67]. Hargitai *et al.* found that 40-50% of hemp fibre by weight is needed to achieve optimal mechanical properties in reinforced polypropylene composites. [68]. Hu and Lim mentioned that a 40% volume fraction of hemp fibres treated with alkali is needed for optimum mechanical properties in polylactic acid composites [66].

In this research project a hemp and cotton hybrid woven mat is used as reinforcement. Hemp is classified as a bast fibre and cotton is classified as a seed fibre [52]. Bast fibres are obtained from the inner bark of dicotyledonous plants [69, 70] whereas seed fibres are collected from the seeds themselves or the seed cases [71].

The advantages of hemp fibre over traditional glass fibres are typical of the advantages of using natural fibres instead of synthetic fibres (as mentioned in the overview section of Chapter 2.5). The disadvantages of hemp fibre composites in comparison with glass fibres composites are that hemp fibre composites have a lower impact strength, higher level of moisture absorption and poor thermal stability. An increase in moisture absorption can lead to dimensional changes and in its turn, to microcracking. Poor thermal stability can lead to the thermal degradation of the hemp fibres [68].

Joshi *et al.* compared conventional composite materials and natural fibre reinforced materials (NRF materials) [59]. A significant weight reduction was found in automotive parts reinforced with natural fibres compared to their conventional counterparts. This can be seen in Table 8.

Table 8: Comparison in weight between natural fibre reinforced composites and conventional composites used for automotive applications [59]

Component	Conventional composite materials	Weight of conventional component (g)	NRF materials	Weight of NRF component (g)	Weight reduction (%)
Auto side panel	ABS	1125	Hemp –epoxy	820	27
Auto insulation panel	Glass fibre - PP	3500	Hemp - PP	2600	26
Transport pallet	Glass fibre - PP	15 000	China reed - PP	11 770	22

Ahmad *et al*. produced a natural fibre reinforced composite using EpoxeAmite as the resin and woven hemp fibres as the reinforcement. Vacuum infusion was used as the production process. The tensile strength of this composite was found to be 47.0 MPa and the elastic modulus, 2.1 GPa [61].

Symington *et al.* produced a hemp reinforced composite using a base resin with a Young's modulus of 3.0 GPa (between polyethylene terephthalate and polystyrene). The volume fraction of the fibres was 50-60%. This composite showed a maximum stress of 58.2 MPa and a Young's modulus of 13.7 GPa [72].

Few castor oil-based hemp-filled composites are reported. One such was a microfoam composite made by Arungeren *et al*. [73]. Aging was noted in that mechanical properties increased with time. These were ascribed to oxidative crosslinking reactions that involved unreacted double bonds along the triglyceride chains.

Cotton fibre

Cotton fibres are used as reinforcement primarily due to availability. 46% of the world annual natural fibre production is cotton [55]. The high liquid absorptivity of cotton fibre is an attractive property for use in composites [55]. Compared to bast fibres like hemp, which contain lignin, cotton fibre does not contain lignin [74] as seen in Figure 11. Cotton is therefore more resistant to UV-degradation than other fibres containing lignin. Timar-Balazsy and Eastop indicate that Stout compared the impact of exposure to UV radiation on the strength of fibres that contain lignin and fibres that do not. It was found that cotton fibres eventually experienced a loss in strength due to UV degradation but fibres containing lignin reached the loss in strength with shorter exposure times [75].

The Young's modulus for cotton fibres is approximately 6.0 GPa [74]. Graupner manufactured a cotton fiber-reinforced composite using PLA as the matrix by means of compression moulding.

The properties were as follows:

Table 9: Properties of cotton/PLA fibre reinforced composites [74]

Sample	Fibre weight percent (%)	Tensile strength (MPa)	Young's modulus (GPa)	Elongation at break (%)	Charpy impact strength (kJ/m^2)
Cotton/PLA	40	41.2	4.2	2.95	28.7
Neat PLA	0	30.1	3.8	0.83	22.4

Raftoyiannis manufactured a composite using woven cotton fibres and a polyester resin as matrix. Under tension an average Young's modulus of 1.2 GPa was found for the reinforced samples. Raftoyiannis concluded that woven cotton fibre reinforced polyester composites are satisfactory in terms of structural requirements for parts like panels or doors in the automotive industry [70].

No examples of either hemp-filled or cotton-filled maleated castor oil composites have been found in the literature.

Reinforcing methods

The following four methods are expected to be compatible with the MACO/styrene co-polymer:

(a) Hand lay-up process

In this process the reinforcing fibres are added layer by layer and the polymer is spread between the layers by using a brush [76]. Although hand lay-up is the simplest and most cost effective method, in most cases the quality of the product is not sufficient. During hand lay-up a large quantity of voids normally form. Micro-voids form between the reinforcement and macro-voids in the matrix itself (Figure 15). Vacuum bagging under pressure decreases the amount of voids (especially macro-voids). The fewest voids are present when cured at an elevated temperature under vacuum [77].

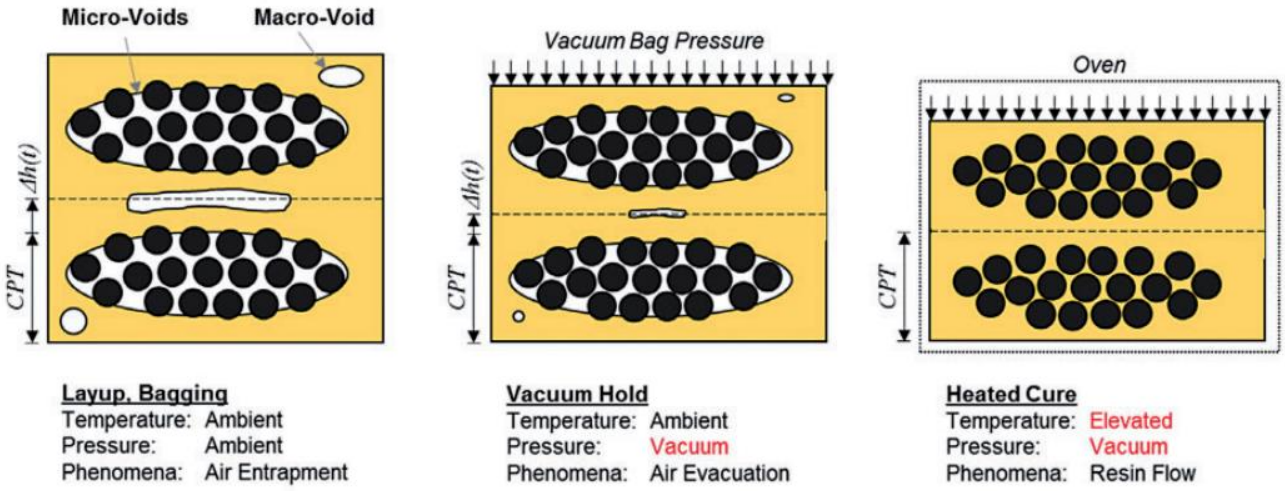

Figure 15: Formation of voids during different manufacturing methods [77]

(b) Vacuum infusion process

High performance and large scale composites can be produced with this closed-mold process. In this process a resin of choice is pulled into a laminate by means of a vacuum pump. The dry reinforcing materials are placed in a mould, a vacuum is formed and thereafter the liquid resin is sucked through the reinforcing material via tubing [76]. The liquid resin becomes the matrix after curing [54]. The pressure created by the vacuum is useful to force the resin through the fibres and ensure sufficient wetting of the fibres [54]. This method is suitable for resins that cure at both ambient and elevated temperatures.

Some of the problems encountered with the vacuum infusion are [72]:

- ensuring uniform resin fill,
- damaging of the vacuum pump due to resin escaping through the vacuum pipe,
- methods required to reduce voids in the finished product,
- consistency of the fibre to matrix volume fraction,
- undesirable finish on the surface of the composite, and
- large amount of material wastage

(c) Vacuum bagging

Another type of closed mould process is that of vacuum bagging. Large, high performance parts can be manufactured using this process. It is normally used for applications where high production rates are not important [54]. The pressure caused by the vacuum is used to achieve interesting properties [76]. Although the processes of vacuum bagging and vacuum resin infusion look similar, there can be a noticeable difference in the composite properties they produce. The reason for this is that the resin infusion process ensures that the fibres are completely wetted by the resin.

For vacuum bagging on the other hand, a wet lay-up by hand has to be done if pre-pregs are not used, before the vacuum can be applied. This results in less favorable properties [54].

(d) Compression moulding

Compression moulding/matched moulds is a process where a polymeric material is compressed into the final product by means of a hydraulic heated press [78] and high pressure [79]. This manufacturing process is normally used for thermosets but can be applied to thermoplastics and elastomers [79]. This process is popular in the automotive industry for the manufacturing of sheet moulding compounds [80].

Some of the advantages of using the compression mould process [79, 81] are as follows:

- low tooling costs (due to simplistic moulds being used),
- low setup costs,
- small amount of material wastage,
- high mechanical properties of final products,
- low mould maintenance,
- production of large scale parts, and
- suitable for reinforced composites.

Disadvantages of this method [79, 81] include

- it is not suitable for intricate shapes,
- thick and heavy parts will have slow curing times,
- when using polymers with low viscosity, flash is produced (rough edges when resin escapes mould) that has to be removed, increasing costs, and
- slow production speed compared to, for example, injection moulding.

2.6. Biodegradation of polymers

There are different methods for the disposal of polymers. Landfill sites can be used but are not always readily available. Recycling is one of the more preferred options but recycling systems are not in place in most countries. Lastly incineration is an option but this method contributes to air pollution [82]. Biodegradation is preferred.

Leja and Lewandowicz define biodegradation as the chemical degradation of materials which is promoted by the presence of microorganisms (*e.g.*, bacteria, fungi and algae) [83]. A more comprehensive definition is when the chemical, physical and mechanical properties of the material change. It consequently weakens and completely disintegrates in the presence of microorganisms, aerobic and anaerobic conditions [84]. Biodegradation normally takes place in three stages [85], namely:

1. biodeterioration
2. biofragmentation
3. assimilation

Biodegradable polymers can either be petrochemical- or bio-based [82]. The rate of biodegradation is largely dependent on the properties of the materials (chemical and physical) and on the polymer structure [82]. Arutchelvi *et al.* discussed the factors that affect the biodegradability of a polymer. These are:

- presence of polar functional groups,
- molecular weight and density of the polymer material,
- crystallinity of the polymer,
- complexity of the polymer structure (*e.g.*, branching),
- presence of weak ester or amide bonds,
- molecular composition of the polymer, and
- physical morphology of the polymer (films, pellets, *etc.*) [86].

The biodegradability of polymers can be improved by numerous methods. Examples of these methods are:

- ensuring that the polymer has a degradable backbone (this includes polyanhydrides and polylactones) [87],
- blending of synthetic and biodegradable natural polymers (these natural polymers include, for example, starch and cellulose) [86], and
- the addition of pro-oxidants [86].

During the biodegradation reaction, polymers form byproducts. These can be seen in Figure 16. Degradation of polymers can either be aerobic or anaerobic which results in different byproducts.

The extent of biodegradability can be monitored using different strategies [86]. The strategies include:

- the buildup of biomass on the polymer surface,
- the rate that oxygen is taken up,
- the rate at which CO_2 is formed,
- the products that form using chemical analysis,
- changes in the sample topography, and
- changes in the mechanical and physical properties of the polymer [86].

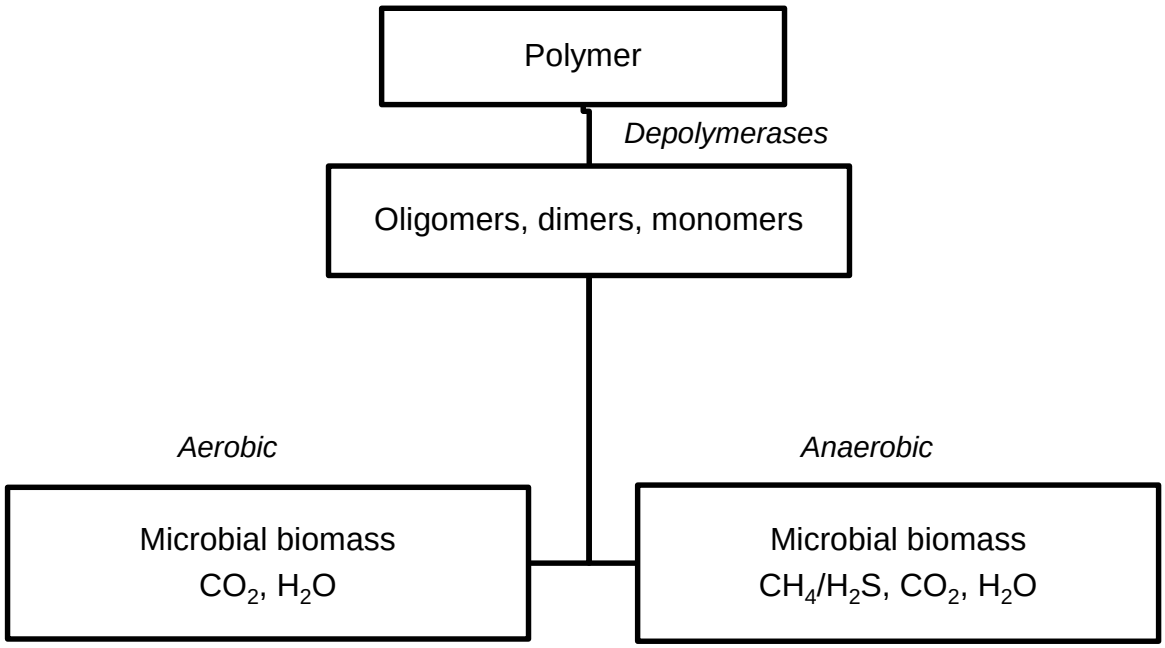

Figure 16: Process of polymer degradation under aerobic and anaerobic conditions (Adapted from Leja and Lewandowicz [83])

Chapter 3: Experimental methods and materials

3.1 Materials

Medical grade castor oil was supplied by Barrs Pharmaceutical Industries (Cape Town, South Africa). Styrene, N,N-dimethylbenzylamine, tert-butyl peroxybenzoate, hydroquinone, 1,2,3,4–tetrahydronaphthalene and maleic anhydride were supplied by Sigma Aldrich (St Louis, MI). Sodium hydroxide, sodium chloride, diethyl ether, ethanol, oxalic acid, dichloromethane and anhydrous magnesium sulfate were supplied by Kimix Chemicals (Cape Town, South Africa). Argon gas (Lasal Alphagaz (Ar 5.0)) was supplied by Air Liquide (Cape Town, South Africa). OsO_4 and RuO_4 stains were obtained from Agar Scientific (Stansted, UK).

Greige fibres (55% hemp/45% cotton) were supplied by Hemporium (Cape Town, South Africa). Commercial grade general purpose polystyrene (GPPS) and high impact polystyrene (HIPS) were obtained from Maizey's Plastics (Cape Town, South Africa). Marshal silicone spray was used as the mould release agent. Plant boutique compost (grade II fertilizer) was purchased from the Builders Express (Cape Town, South Africa).

3.2 Experimental methods: Synthesis and sample preparation

3.2.1 Maleation of castor oil

Medical grade castor oil was maleated following the method of Saied *et al.* [34]. Castor oil and maleic anhydride were added to a 250 mL round bottom flask in a 1:3 molar ratio. This ratio was chosen because each glicerylltriricoleneate molecule has 3 hydroxyl groups at which maleic anhydride can react. Hydroquinone (0.012 wt%) was added to the round bottom flask. The mixture was heated to 90 ˚C under reflux in an argon atmosphere. Once a temperature of 90 ˚C was reached, 0.12 wt% of N,N-dimethylbenzylamine was added to the round bottom flask. Further heating took place until the temperature stabilized at 98 ˚C. The reaction was kept at this temperature for 5 hours under reflux in an argon atmosphere with constant stirring. After 5 hours the mixture was sealed to prevent any oxygen from entering the flask and then left to cool to room temperature. The equipment setup for this reaction can be seen in Figure 17.

3.2.2 Determination of acid value

The titrant was made up by adding 4 g of NaOH to 1000 mL of distilled water.

Standardization of the NaOH solution

50 mL of distilled water were added to 0.13325 g oxalic acid (dried to constant weight at 60 ˚C for 2 hours). Three drops of phenolphthalein were added and the mixture was titrated with the NaOH solution until a pink colour was observed.

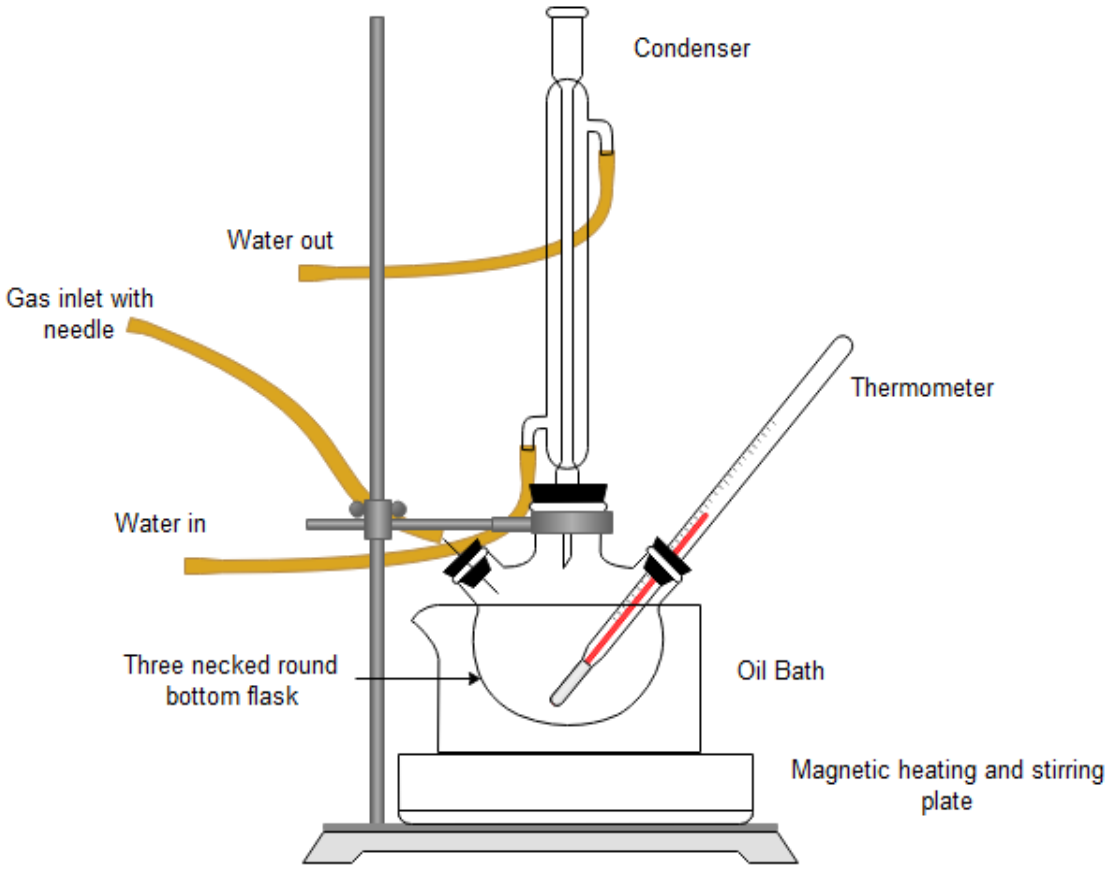

Figure 17: Equipment setup for the maleation of castor oil

The acid number was determined using the following equation:

$$Acid\ Number\ (/100\ mgNaOH) = \frac{V_{NaOH} \times [NaOH] \times 39.997}{M_{sample}} \qquad (1)$$

where,

V_{NaOH} = volume sodium hydroxide used to neutralize solution
[NaOH] = concentration of sodium hydroxide solution
M_{sample} = mass of the sample analyzed

$$[NaOH] = \frac{M_{oxalic} \times P_{oxalic} \times 1000}{V_{NaOH} \times M_{w\ (oxalic)}} \qquad (2)$$

where,

[NaOH] = concentration of sodium hydroxide solution
M_{oxalic} = mass of oxalic acid

P_{oxalic} = assay of oxalic acid
V_{NaOH} = volume of sodium hydroxide used to neutralize the solution
$M_{w\ (oxalic)}$ = molecular mass of oxalic acid

Titration of MACO
Approximately 0.5 g of the castor oil mixture was accurately weighed off at the start of the reaction (when the temperature reached 98 ˚C and all the reactants were added). 25 mL of ethanol and 25 mL of diethyl ether were added to the castor oil mixture. Once dissolved, three drops of phenolphthalein were added and the mixture was titrated with the NaOH solution until a pink colour was observed for at least 30 seconds.

3.2.3 Purification of styrene

The styrene was purified by removing the inhibitor (4-tertbutyl catechol) by means of a separation funnel. Styrene was added to the separation funnel. It was washed twice with a 10% NaOH solution, once with distilled water and lastly with a saturated NaCl solution. The washed styrene was dried with anhydrous $MgSO_4$ for about a minute. Using a vacuum filtration system, the $MgSO_4$ was filtered off and the purified styrene was immediately used.

3.2.4 Matrix formation of maleated castor oil with styrene

The method to form a matrix from maleated castor oil (MACO) and styrene is a modified version of that used by Campanella *et al.* [9]. Note that Campanella *et al.* first prepared a maleated monoglyceride, unlike the triglyceride in this study. Purified styrene (35 wt%) was added to the maleated castor oil (ratio of 1:2) and heated to 50 ˚C. Once a temperature of 50˚C was reached, 2 wt% of the initiator, *tert-butyl* peroxybenzoate was added (ratio of 1 part initiator to 13 parts styrene) and the mixture was heated to 60 ˚C. The mixture was kept at 60 ˚C for 2 minutes. Thereafter it was immediately transferred to the prepared aluminium mould for curing.

3.2.5 Preparation of crosslinked resin

The mould was sprayed beforehand with Marshal silicone release agent and lined with Teflon paper. Before inserting the mould, a vulcanization press (W&W Co. Mini-Vulcanizer) was heated to about 90 ˚C. By using a thermocouple the temperature of the mould could be monitored. The temperature profile used is similar to the one used by Campanella et al. [9]. The temperature profile for 5mm sheets was as follows:

- 2 hours at 90 ˚C
- 2 hours at 120 ˚C
- 1 hour at 160 ˚C

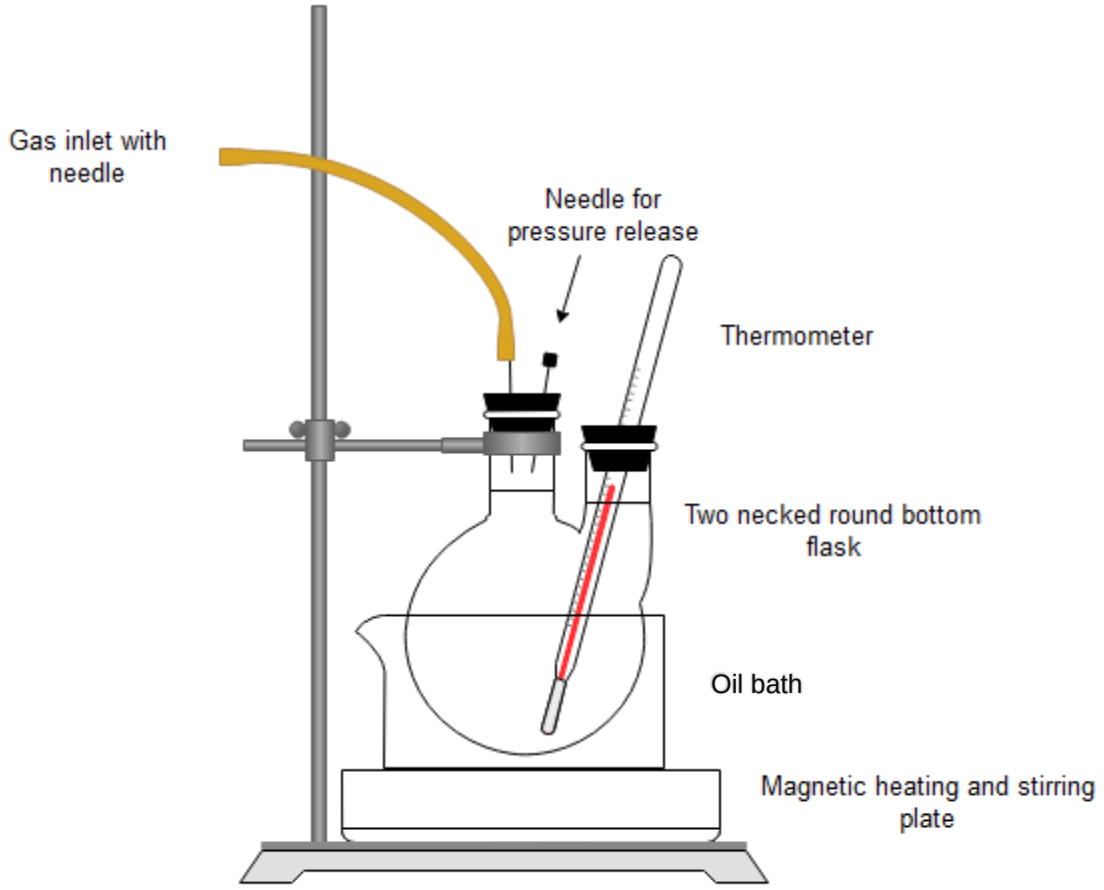

Figure 18: Experimental setup for the copolymerization of MACO with styrene

The temperature profile for 10mm sheets was as follows:

- 2 hours and 15 minutes at 90 ˚C
- 2 hours and 15 minutes at 120 ˚C
- 1 hour and 15 minutes at 160 ˚C

The temperature profile for 2mm sheets was as follows:

- 1 hour and 30 minutes at 90 ˚C
- 1 hour and 30 minutes at 120 ˚C
- 45 minutes at 160 ˚C

The mould was removed from the press. The cured sheets were then left to cool overnight before they were removed from the mould.

Figure 19: W&W Mini-Vulcanizer vulcanization press used for curing

3.2.6 Sample preparation

5 mm and 10 mm cured sheets, as well as the commercial polymer sheets, were sent for waterjet cutting by Waterjet Cape Town, South Africa to produce test samples from the sheets. The sample geometries are indicated under the respective testing sections. Any surface roughness was manually ground off using 220 grit grinding paper followed by 540 grit paper. Water was used as a lubricant. 2 mm cured sheets were cut using a Dremel Moto-Saw.

3.2.7 Alkalization treatment of hemp-cotton (greige) fibres

The hemp-cotton woven fibre mats were soaked in a 6% NaOH solution for 48 hours at a temperature of about 21 ˚C. Distilled water was used to rinse the woven mats where after a 1% acetic acid solution was used to rinse the mats in order to neutralize any leftover NaOH. Lastly the mats were rinsed with distilled water. The rinsed mats were dried in a drying oven overnight at a temperature of 60 ˚C [64]. Note that shrinkage of the mats took place and therefore the mats were only cut after the alkalization treatment.

3.2.8 Hand lay-up process and curing of hemp-cotton fibres in resin

After alkalization treatment the woven mats were cut to size. Aluminium plates covered with a sheet of Teflon were used as the mould. The layers were built up on the Teflon coated aluminium plate. The Teflon layer was wetted slightly with resin before the first woven layer was added. The first layer was added and wetted followed by the second layer, *etc*. Excess resin during the curing process was caught up in a temperature resistant plastic bag. The curing process was kept the same as that mentioned in section 3.2.5 for the respective sheet thicknesses.

3.2.9 Determination of manufacturing volume fraction of fibres

The manufacturing volume fraction of fibres in the cured composite was determined using the following formula:

$$\Phi_{fiber} = \frac{\frac{W_{fibre}}{\rho_{fibre}}}{\frac{W_{matrix}}{\rho_{matrix}} + \frac{W_{fibre}}{\rho_{fibre}}} \qquad (3)$$

where,

ϕ_{fibre} = volume fraction of the fibres
w_{fibre} = weight fraction of fibres (mass of fibre/ total composite mass)
w_{matrix} = weight fraction of the matrix (1-W_{fibre})
ρ_{fibre} = density of fibres (g/cm^3)
ρ_{matrix} = density of matrix (g/cm^3)

The mass of the fibre used for the composite was determined by physically weighing the fibre mats before impregnation with the resin. After the manufacturing of the composite it was weighed to determine the total composite mass. These values were used to determine W_{fibre}.

3.2.10 Determination of crosslink density using a swelling test

Samples (about 3x3mm) were cut using a Dremel Motosaw. The samples were weighed and placed in 10 mL of toluene. The container with samples was left for 24 hours in a dark cabinet. The solvent was replaced twice. After 72 hours the samples were removed from the container and gently dabbed dry with tissue paper. The masses of the wet samples were recorded immediately after drying to prevent the evaporation of solvent from the sample. The samples were dried in an oven at 40-50 °C to remove all solvent and then re-weighed to find the dry mass.

The volume fraction of polymer in the swollen gel and the crosslink density were determined using the following equations:

$$V_{polymer} = \frac{\frac{m_{dry}}{\rho_{original}}}{\frac{m_{dry}}{\rho_{dry}} + \frac{m_{dry} - m_{wet}}{\rho_{solvent}}} \quad (4)$$

$$XLD\ \left(\frac{mol}{cm^3}\right) = -\frac{\ln\left(1 - V_p\right) + V_p + \chi {V_p}^2}{2V_{m,s}\left(V_p^{\frac{1}{3}} - \frac{1}{2}V_p\right)} \quad (5)$$

where,

V_p = volume of polymer (cm^3)
m_{dry} = dry mass of sample (g)
m_{wet} = wet mass of sample (g)
ρ_{dry} = dry density of sample (g/cm^3)
$\rho_{solventl}$ = density of solvent (g/cm^3)
$\rho_{original}$ = density of original sample (g/cm^3)
XLD = crosslink density (mol/cm^3)
χ = solvent interaction parameter (χ = 0.37 for polystyrene [88])
$V_{m,s}$ = molar volume of the solvent (mol/cm^3)

3.3 Experimental methods: Property testing

3.3.1 Impact testing

Charpy impact testing was conducted according to ASTM D6110 [89]. A Zwick Roell B5113.300 impact tester was used. The sample geometry can be seen in Figure 20.

The width of all the material specimens were 10 mm with a notch depth of 2 mm. The thicknesses of the MACO/PS and reinforced MACO/PS samples were 10 mm whereas the PS samples had a thickness of 2 mm and the HIPS samples a thickness of 4 mm. A 5 Joule pendulum was released from an angle of 160° perpendicular to the sample. All samples had a height of approximately 10 mm. The net breaking energy (in Joule) was recorded from the instrument display as the instrument compensates for friction loss. 5 specimens were tested per material.

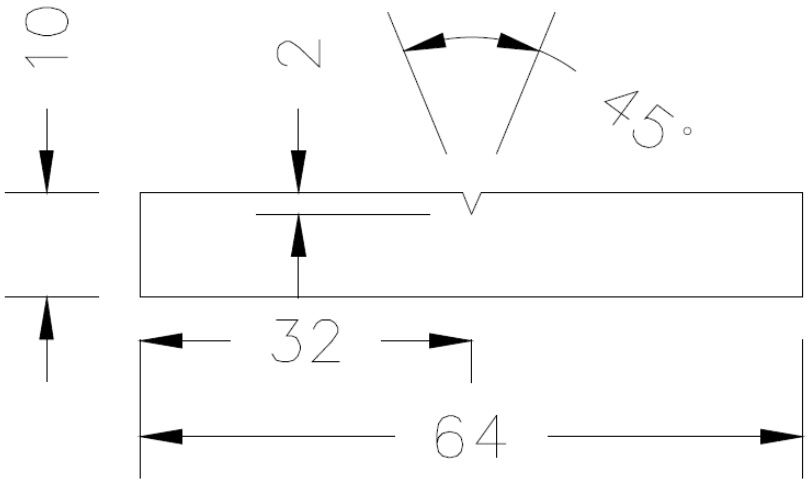

Figure 20: Sample geometry for Charpy impact test samples (units in mm)

The impact resistance of the materials was calculated as follows

$$impact\ resistance\ = \frac{breaking\ energy}{width \times height} \qquad (6)$$

3.3.2 Tensile testing

Tensile testing was done according to ASTM D638-14 using a standard dogbone sample geometry (Figure 21) [90]. A Zwick Roell 1484 Universal tester was used for the tensile tests. The gauge length of the MACOPS samples were 33 mm. The GPPS and HIPS had a thickness of 2 mm and 4 mm respectively. A Limess video extensiometer was used to ensure accuracy in the modulus measurements. The gauge length of the video extensiometer was set to ±30 mm and calibrated before the test was started. A load cell of 10 kN was used for testing.

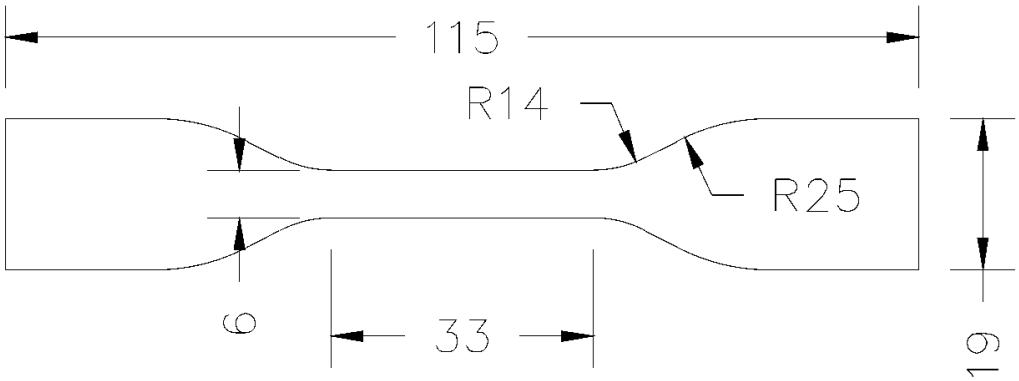

Figure 21: Sample geometry of tensile test samples (units in mm)

For this test the crosshead speed was set to 5 mm/min. 3 specimens were tested per material.

The maximum tensile strength was calculated using the following formula:

$$\sigma_{tensile} = \frac{F}{A} \qquad (7)$$

where,

$\sigma_{tensile}$ = maximum tensile stress (MPa)
F = force (N)
A = cross sectional area (mm^2)

To calculate Young's Modulus of the material, the following equation was used

$$E = \frac{\Delta\sigma}{\Delta\varepsilon} \qquad (8)$$

where,

E = Young's modulus (MPa)
$\Delta\sigma$ = difference in flexural stress between two selected points (MPa)
$\Delta\varepsilon$ = difference between two selected strain points

The toughness of the tested materials was determined by calculating the area under the curve by numerical integration.

In addition to the tensile testing of the produced samples and the commercial polymers, tensile testing of the greige and pure hemp fibres was done according to ASTM Standard D3822-14 [91]. A crosshead speed of 1mm/min was used in this case. The fibres were attached to aluminium tabs for easy gripping as seen in Figure 22. The fibres were attached in such a manner that the distance between tabs were 30mm. The distance between the tabs were used as the gauge length for the video extensiometer. A commercial cyanoacrylate adhesive was used.

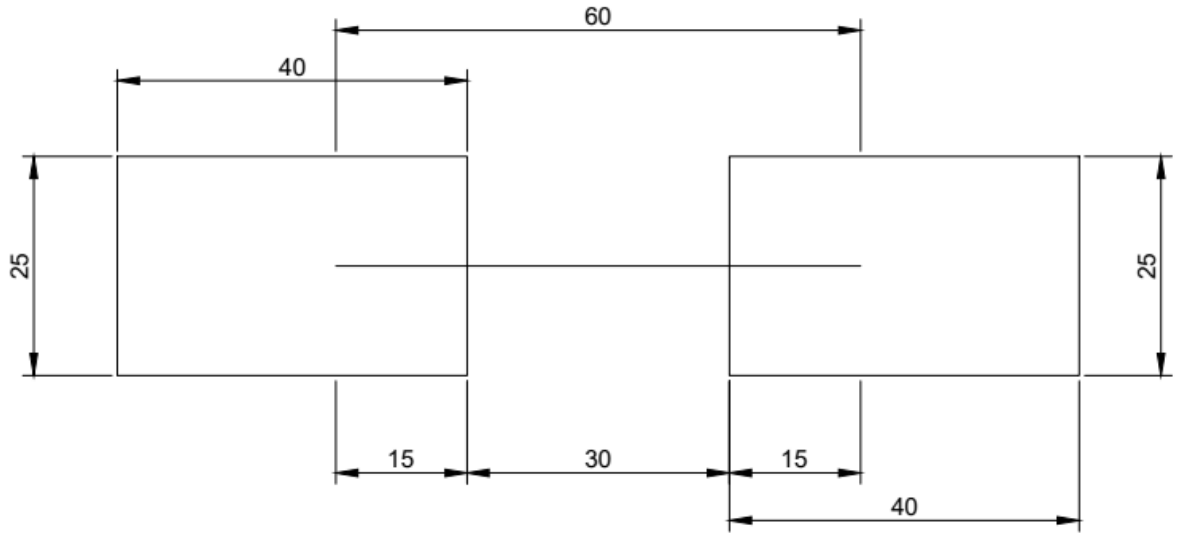

Figure 22: Tabbing diagram for fibres (units in mm)

The cross-sectional area of the fibres were determined using the following method:

Measuring the diameter of the fibre using a stereomicroscope

The fibre was placed under a Leica MZ 8 stereomicroscope and using Nix image analysis software, the diameter was measured and cross-sectional area calculated.

Calculation of cross sectional area of fibre

The load bearing cross-sectional area can be calculated as follows:

$$Cross\text{-}sectional\ area\ (mm^2) = \pi r^2 \qquad (9)$$

where,

r = radius of the fibre in mm (diameter/2)

Note that the Young's modulus of the fibres were determined as the slope of the linear region in the stress-strain curve.

3.3.3 Efficiency of the fibre reinforcement

The efficiency of the fibre as reinforcement was determined by calculating the theoretical modulus of the reinforced MACOPS composite. This was done by combining the rule of mixtures and the Halpin-Tsai model to calculate the modulus of a matrix reinforced with woven fibres [92]. The Halpin-Tsai equation is suitable for discontinuous fibres or for yarn fibres made up of shorter filaments as in this study [93]

The theoretical modulus used is similar to that used by Abdel Ghafaar *et al.* [94] with a minor adjustment. The rule of mixtures is used to predict properties, including the modulus and strength, of fibre reinforced composites [95].

It is important to note that in this calculation, woven fabric is considered to have two types of fibres - longitudinal and transverse fibres, present in equal quantities. The assumption is made that the fibre modulus in the transverse and longitudinal direction is the same. The volume fraction can thus be written as follows:

$$\varphi_{tf} = \varphi_{lf} = \frac{1}{2} V_f \qquad (10)$$

where,

Φ_{tf} = volume fraction of transverse fibres
Φ_{lf} = volume fraction of longitudinal fibres
V_f = volume fraction of fibre in composite

Using the rule of mixtures,

$$E_c = \frac{1}{2}(E_T + E_L) \qquad (11)$$

where,

E_c = elastic modulus of the composite
E_T = elastic modulus in the transverse direction
E_L = elastic modulus in the longitudinal direction

Note that the value of ½ is used on the assumption that longitudinal and transverse fibre density are equal. Abdel Ghafaar *et al.* replace ½ by an empirically adjustable parameter F_1) [94]. In this study, the load bearing efficiency, instead is calculated as the actual measured modulus as a percentage of the predicted modulus.

The elastic moduli in the transverse and longitudinal direction can be calculated using the Halpin-Tsai formulae.

$$E_T = \frac{E_m\left(1 + \zeta_T \eta_T \varphi_{tf}\right)}{1 - \eta_T \varphi_{tf}} \quad (12)$$

$$E_L = \frac{E_m\left(1 + \zeta_L \eta_L \varphi_{lf}\right)}{1 - \eta_L \varphi_{lf}} \quad (13)$$

$$\eta_T = \frac{\frac{E_f}{E_m} - 1}{\frac{E_f}{E_m} + \zeta_T} \quad (14)$$

$$\eta_L = \frac{\frac{E_f}{E_m} - 1}{\frac{E_f}{E_m} + \zeta_L} \quad (15)$$

where,

E_T and E_L = elastic modulus in transverse and longitudinal direction
E_m = elastic modulus of matrix
ζ_T = empirical parameter = 0.5 for transverse
ζ_L = empirical parameter = 2 for longitudinal
η_T, η_L = calculated parameters
E_f = elastic modulus of fibre
Φ_{tf} = volume fraction of transverse fibres
Φ_{lf} = volume fraction of longitudinal fibres

3.3.4 Flexural testing

Flexural testing was done in the form of a three-point bend test according to ASTM D7264-15 [96]. A Zwick Roell 1484 universal tester was used for testing. The sample geometry can be seen in Figure 23.

The commercial GPPS and HIPS had a thickness of 2 mm and 4 mm respectively. A crosshead speed of 1 mm/min and a 10 kN load cell was used for testing and the span was set to 56 mm. 5 specimens were tested per material.

Figure 23: Sample geometry of flexural test samples (units in mm)

The maximum flexural stress was calculated using:

$$\sigma_{flexural} = \frac{3\,PL}{2bh^2} \qquad (16)$$

where,

$\sigma_{flexural}$ = stress at the outer surface at mid-span (MPa)
P = applied force (N)
L = length of support span (mm)
b = width of beam (mm)
h = thickness of beam (mm)

3.3.5 Specific strength and specific toughness

The specific strength of the neat MACOPS matrix and the reinforced MACOPS composite was determined as:

$$specific\ strength\ \left(\frac{Nm}{kg}\right) = \frac{\sigma}{\rho} \qquad (17)$$

where,

σ = maximum flexural or tensile strength (N/m^2)
ρ = density of the polymer or composite (kg/m^3)

The specific toughness can be determined as follows:

$$specific\ toughness\ \left(\frac{Nm}{kg}\right) = \frac{toughness}{\rho} \qquad (18)$$

where,

Toughness = area under stress-strain curve (MPa)
ρ = density of the polymer or composite (kg/m^3)

3.*3.6 Hardness measurement*

Shore hardness was measured using a Durotech M202 durometer. An indenter to measure Shore-D hardness was used for all the tested materials. 10 measurements were made per material tested.

3.3.7 Density measurement

The density of the material (MACOPS and HIPS) was determined using a density bottle. Distilled water (ρ = 1.000 g cm^{-3}) was used as the liquid with known density. The density of GPPS was determined by the flotation technique using 1,2,3,4–tetrahydronaphthalene and dichloromethane. For the density determination of the fibres, ethanol (ρ = 0.789 g cm^{-3}) was used as the liquid with the known density for greige fibres and hexane for the hemp fibres.

The volume of the sample was determined using the following equation

$$V_s = \frac{M_{liquid} - (M_t - M_b - M_s)}{\rho_{liquid}} \qquad (19)$$

where,

V_s = volume of the sample (cm^3)
M_t = total mass of bottle, sample and liquid (g)
M_b = mass of bottle (g)
M_s = mass of sample (g)
M_{liquid} = mass of liquid required to fill bottle (mass of filled bottle – mass of empty bottle) (g)
ρ_{liquid} = density of liquid at room temperature (g/cm^3)

The density was determined by dividing the sample mass by the calculated sample volume.

To determine the density using the flotation method, 1,2,3,4–tetrahydronaphthalene was added to a 250 mL conical flask with the GPPS sample. Dichloromethane was titrated into 1,2,3,4–tetrahydronaphthalene until the sample just floated. The titrated mixture was transferred to a density bottle to determine its density.

The theoretical density of the reinforced MACOPS composite was calculated using the rule of mixtures. The equation used was as follows:

$$\rho_c = \rho_f V_f + \rho_m V_m \qquad (20)$$

where,

ρ_c = density of composite (g/cm^3)
ρ_f = density of fibre (g/cm^3)
ρ_m = density of matrix (g/cm^3)
V_f = volume fraction of fibre
V_m = volume fraction of matrix

For this calculation the fibre volume fraction used is the manufacturing fibre volume fraction as calculated in section 3.2.9.

3.3.8 Differential scanning calorimetry

Differential scanning calorimetry was performed at a heating rate of 20 ˚C/min. Sample sizes were approximately 2-3 mg. A DSC 250 Discovery Series was used to conduct the tests. The DSC was calibrated for temperature using the melting temperature of pure samples of In (156.61 ^{o}C), Sn (231.88 ^{o}C), Pb (327.46 ^{o}C) and Zn (419.53 ^{o}C). Heat flow was calibrated using the enthalpy of fusion of In (28.58 J/g). Samples were placed in aluminium pans with an empty pan as reference. High purity N_2 was used as purge gas at a flow rate of 25 $\mu\ell$/min. Glass transition temperatures were determined at the inflection points of the heat flow signals.

3.3.9 Thermogravimetry

Thermogravimetry was performed under a high purity nitrogen atmosphere (flow rate of 30 $\mu\ell$/min) at a heating rate of 10 ˚C/min. A TGA 5500 Discovery Series with Pt cradles was used to conduct the tests. Sample sizes were approximately 10mg. The thermogravimetric analyser was calibrated for temperature using the Curie points of samples of alumel (152 ^{o}C), Ni (354 ^{o}C), an 83% Ni/17% Co alloy (554 ^{o}C), a 63% Ni/37% Co alloy (746 ^{o}C) and a 37% Ni/63% Co alloy (931 ^{o}C). Mass was calibrated using reference mass standards.

3.3.10 Biodegradability testing

The biodegradability test was based on the ASTM standard D5988-18 [97].

Soil preparation

A 2mm sieve was used to reduce the particle size of the compost to a maximum of 2 mm.

The pH of the compost was measured using a Mettler Delta 350 pH-meter. Buffers of pH 4 and 7 were used for standardization of the meter. A mixture of 20 g compost and 50 mL water was made of which the pH was tested.

As the compost was relatively dry on purchase a small amount of water was added to wet the soil. The initial moisture content of the soil was determined by adding the wet soil to a beaker and determining the mass thereof. To determine the dry mass of the soil, the soil was dried overnight in an oven at 105 ˚C. The following equation was used to determine the initial percentage moisture content,

$$initial\ percentage\ moisture\ content = \frac{w_2 - w_3}{w_2 - w_1} \times 100 \qquad (21)$$

where,

w_1 = mass of container (g)
w_2 = mass of sample soil and container (g)
w_3 = mass of dried sample soil and container (g)

A calculation was then done to determine the amount of water to be added to reach a moisture content of 60%.

$$W_d = W_0 \times \frac{(100 - M_0)}{100} \qquad (22)$$

$$W_{MO} = W_0 - W_d \qquad (23)$$

$$W_1 = W_d \times \frac{100}{(100 - M_1)} \qquad (24)$$

$$W_{water} = W_1 - W_0 \qquad (25)$$

where,

W_d = dry soil mass (g)
W_0 = initial soil mass (g)
M_0 = initial percentage moisture content
W_{MO} = mass of water in initial soil (g)
W_1 = humidified soil mass (g)
M_1 = final percentage moisture content
W_{water} = mass of water in soil with moisture content M_1

Sample preparation

Polystyrene samples were used as a negative control and were cut using a utility knife. Printed newspaper was used for the positive control. The MACOPS matrix and reinforced MACOPS matrix were cut using a Dremel Motosaw.

Setup of experiment

Polypropylene 5 L buckets with lids were used as the containers for this experiment. 500 g soil (with a moisture content of approximately 60%) was added to each container. The individual masses of the samples were recorded. Half of the soil was first added where after the samples were placed in the container and covered with the rest of the soil. Care was taken to cover the samples completely. The mass of the container (containing the soil and samples) was recorded. The containers were placed in a dark cupboard at room temperature and the mass of the containers were recorded every two weeks. After each mass recording the difference in mass was corrected for by adding distilled water to the container (until the mass was that of the original container). This was done for a total of ten weeks.

Tensile testing of degraded samples

At the end of ten weeks tensile tests were conducted according to ASTM D638-14 [90]. A video extensiometer was used to ensure accurate modulus results.

3.3.11 Contact-angle measurements

Pictures where taken at an angle of 90˚ to the sample using a Canon EOS100D with an EFS 18-55 mm lens. An equal amount of distilled water was dropped onto each sample using a syringe. ImageJ image analysis software was used to calculate the contact angle (θ_C).

3.4 Experimental methods: Optical characterization

3.4.1 Raman spectroscopy

Raman spectroscopy was used for compositional analysis of MACOPS matrix and the reinforced MACOPS composite. A WiTec Alpha 300 R was used. The laser power for the solid samples was set to 1-2 mW except for MACOPS the laser power was set to 15mW as lower laser power showed significant amounts of noise. For liquid samples (MACO and castor oil) the laser power was set to 5 mW. The excitation wavelength was 532.2 nm for all samples. Raman spectra were obtained using an integration time of 1.19 seconds. Raman maps were obtained using an integration time of 0.25 seconds except for MACOPS where an integration time of 0.44 seconds was used. All solid samples were analyzed looking at the waterjet cut face of the sample.

3.4.2 Scanning electron microscopy of fracture surfaces

A WiTec RISE electron microscope was used for the analysis of the tensile specimen fracture surfaces. Due to the detailed topography of the fracture surfaces, the samples were not carbon-coated. Backscatter electron analysis was performed under low vacuum and in the presence of a small amount of moisture. An acceleration voltage of 20 kV was used. The sample was viewed under a 200 x magnification.

3.4.3 Transmission electron microscopy

MACOPS and HIPS were cut using an ultramicrotome (Leica Reichert Ultracut S) with a diamond blade (Diatome). The samples were cut to a thickness of 100 nm. The samples were placed on a copper grid and vapour stained with a 2% OsO_4 solution for 1 hour and 16 hours. RuO_4 staining (0.6%) was performed separately to vapour stain the samples for 30 minutes.

Samples were viewed under a FEI Tecnai G2 F20 X-Twin transmission electron microscope. The TEM was operated at 200 kV (Lab6 emitter) and fitted with a Tridiem energy filter and Gatan CCD camera.

Chapter 4: Results and discussion

4.1 Synthesis and sample preparation

4.1.1 Acid values

For the acid value at the beginning of the reaction a sample was taken from the flask just as the temperature of the mixture reached 98 °C. The sample for the start of the reaction dissolved quite easily in the ethanol/diethyl ether mixture. The acid value for the start of the reaction was determined to be 80.0 (±1.0) /100 mgNaOH. Note that all values in brackets represent the standard deviation of the mean.

When the reaction time reached five hours, the sample for the calculation of the acid value at the end of the reaction was removed from the reaction flask. An increase in the viscosity of the mixture was noticed. The mixture took longer to dissolve in the ethanol/diethyl ether mixture. The acid value for the end of the reaction was determined to be 74.7 (±1.62 /100 mgNaOH.

Ghorui *et al.* used the determination of the acid values to determine if the maleation reaction was completed. An acid value of approximately 111 was found for the start of the reaction and towards the end of the reaction (after four hours when the reaction was stopped) the acid value was determined to be approximately 109 [98]. Mistri *et al.* measured the acid values for a time of 4 hours during the maleation of castor oil. A similar trend to the data measured by Ghorui *et al.* is seen in the results of Mistri *et al.* (Figure 25) [14].

Initially an esterification took place resulting in the formation of free acid groups. This formation caused an increase in the acid value during the first half of the reaction as seen in Figure 24. As the reaction progressed the acid value started decreasing due to the formation of dimers, trimers or oligomers with these free acid groups [14, 98].

By extrapolating the graph in Figure 24 to reach a reaction time of five hours (red dashed line), it is seen that the acid value decreases to approximately 100 /100 mgKOH. Thus from start to finish the acid value decreased by a value of approximately 11 /100 mgKOH. The experimental results of Mistri *et al.* yielded approximately the same values [13].

To compare the experimental results with the literature, the acid values were calculated as if KOH was used instead. Thus at the start of the reaction an acid value equivalent to 111.9 (±1.4) /100 mgKOH was obtained and at the end of the reaction the acid was 101.9 (±1.5) /100 mgKOH. The return of the acid value to near the starting value is indicative of no more maleic anhydride was reacting towards the end of the reaction [98]. The increase in viscosity of the mixture supports the fact that the maleation reaction took place. No attempt was made to extract any unreacted maleic anhydride

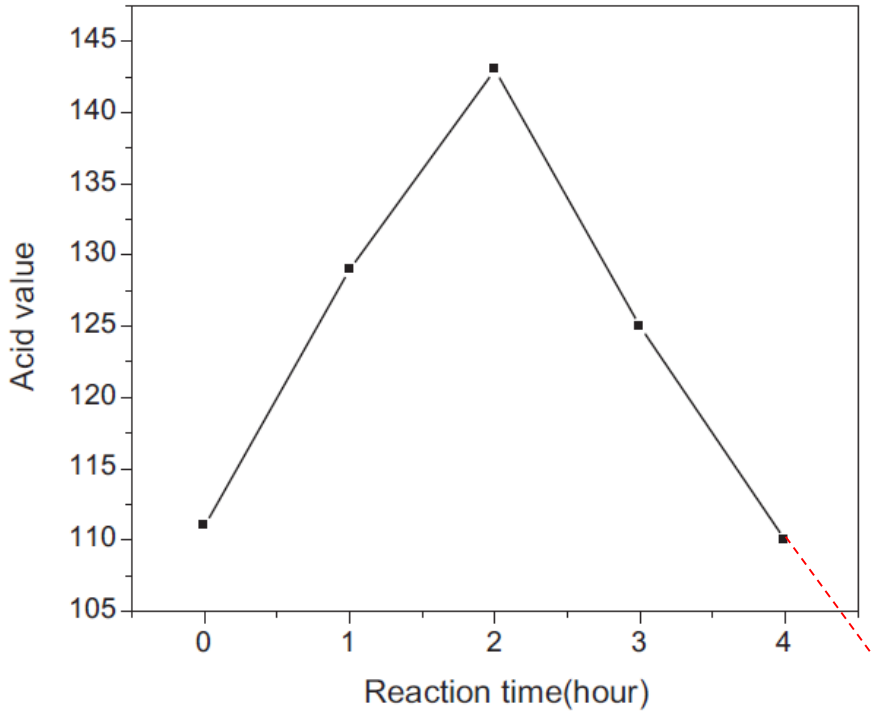

Figure 24: Acid value versus reaction time for the maleation of castor oil (adapted from Ghorui et al. [98])

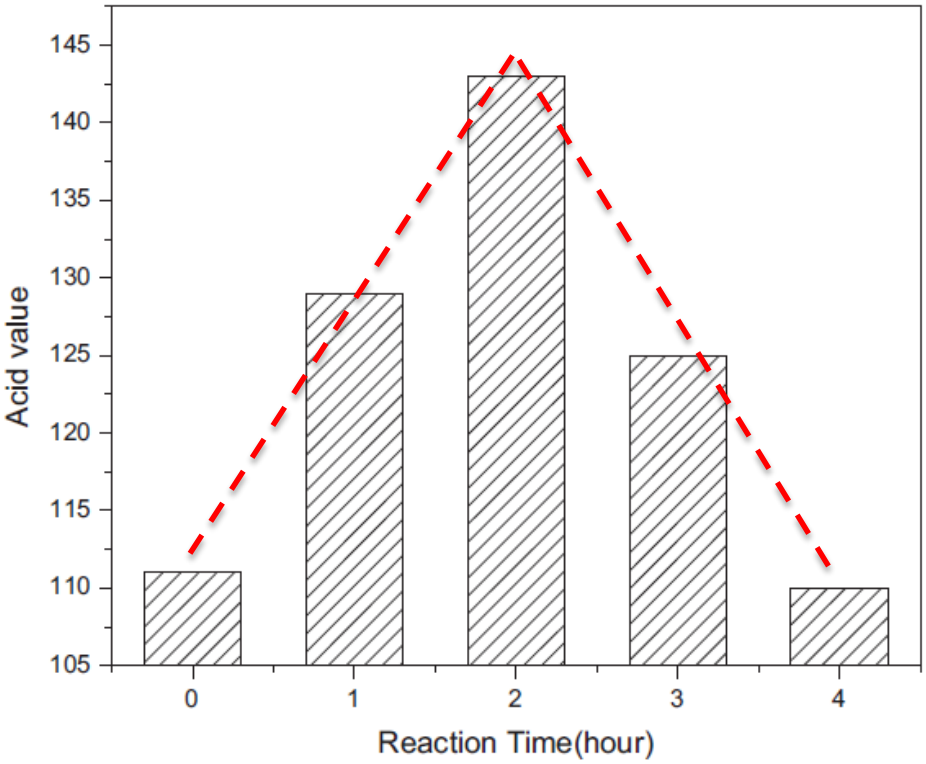

Figure 25: Trend in the acid value during the maleation of castor oil (reproduced from Mistri et al. [14]

4.1.2 Matrix formation of maleated castor oil with styrene

When following the method of Campanella *et al.* [9], a problem was encountered when using a mixing time of two hours at 60 °C. After a mixing time of approximately 30-45 minutes the mixture started to gel and harden in the reaction flask. To solve the problem the mixture was heated up to 60 °C whilst stirring vigorously and left at this temperature for only two minutes to ensure thorough mixing. It was then immediately poured into the mould.

Considering the reaction of maleated castor oil glycerides with styrene monomer as illustrated by Echeverri *et al.* [37] a proposed structure of the MACOPS matrix was formulated. The proposed structure can be seen in Figure 26. Squiggly lines represent positions at which styrene could attach and form chains. Note that some double bonds would remain unreacted.

Figure 31 represents just one of a set of reactions that would have occurred. Another possible reaction path that can be considered for the reaction of styrene with maleated castor oil is the formation of a polystyrene homopolymer by means of free radical polymerization. Considering the results for the Raman spectrum of MACOPS (Section 4.3.2), the presence of the peak at 1654.3 cm^{-1} could be due to the presence of remaining double bonds [99] thus possibly pointing to the presence of homopolymerized styrene. The abstraction of allylic hydrogens to form a radical which then reacts with styrene and results in the formation of a polystyrene homopolymer cannot also be ruled out [100].

4.1.3 Curing of resin

Care was taken in the design of a mould as the viscosity of the resin is significantly lower at a temperature of 90 °C than at room temperature. If the mould was not sealed completely a small amount of resin leaked out causing surface imperfections and uneven thickness of the end product; therefore a gasket seal was used for the sealing of the mold. Once the cured sheet was removed a small amount of red gasket seal residue was left on the edges as seen in Figure 27. The mould was also designed in such a way that the resin did not touch the top surface of the mould. In such an event the resin would pull away as it started to cure and form bubble gaps (Figure 28, Figure 29), creating large surface imperfections.

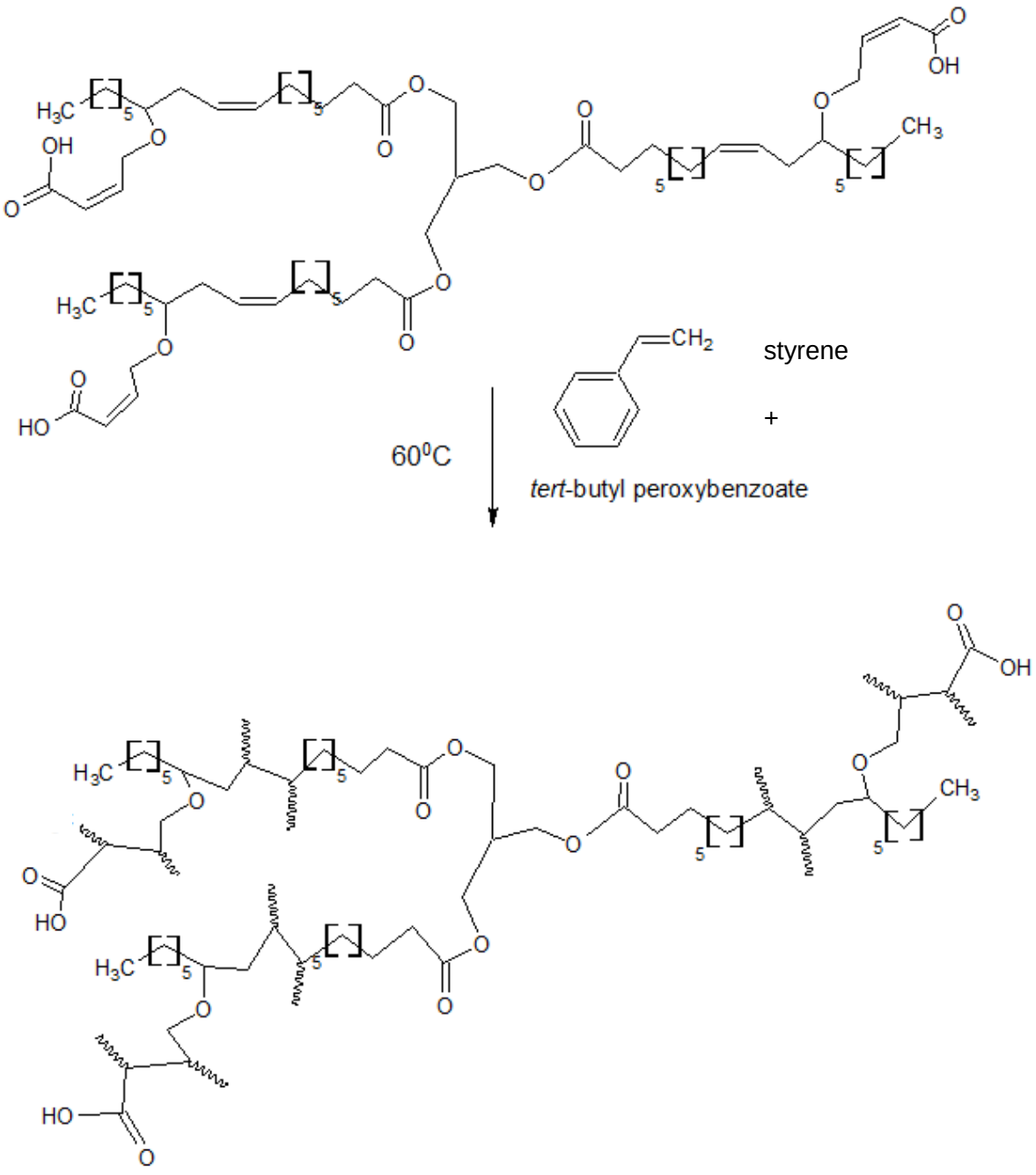

Figure 26: Proposed reaction of MACO with styrene

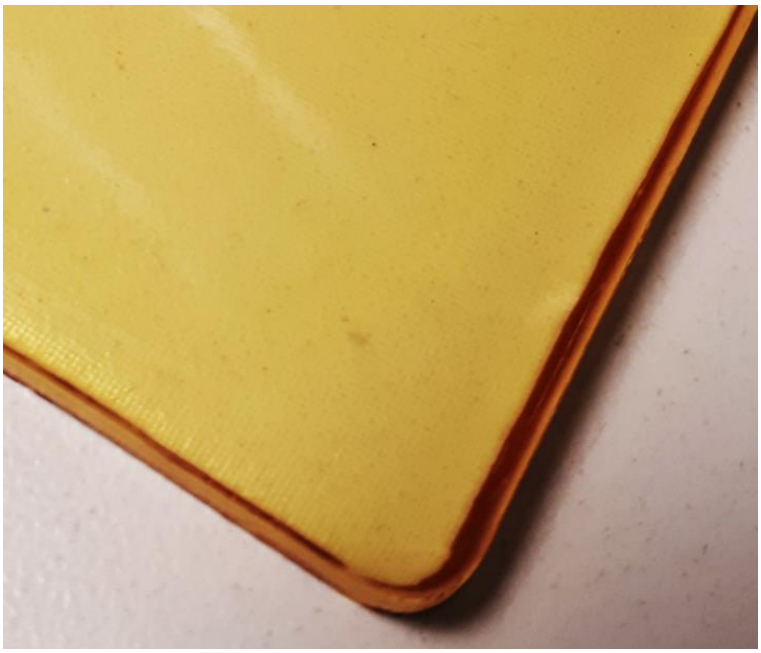

Figure 27: Sheet of neat MACOPS matrix

Figure 28: Bubble gaps formed on surface of cured MACOPS matrix

Figure 29: Side view of bubble gaps on surface of MACOPS matrix

4.1.4 Curing of reinforced resin

During the hand lay-up process the greige fibres seemed to wet easily. After curing, when the samples were cut, some delamination was visible. This could be due to uneven wetting caused by the hand lay-up process, creases in the fabric or the fact that a relatively tight weave was used. This could have led to the delamination and the presence of voids between the fibre and matrix.

The manufacturing volume fraction of the MACOPS composite was calculated to be 0.53 (as explained in section 3.2.9). This calculation took into account the resin that was squeezed out during curing as the calculation was based on the mass of the final reinforced product and the mass of the fibres used in the hand lay-up process.

Figure 30: Sheet of MACOPS matrix reinforced with greige fibres

4.1.6 Swelling testing of neat MACOPS

Due to the fact that the MACOPS is novel, all experimental parameters are not yet known. For this reason the polymer solvent interaction factor of polystyrene (χ_1 = 0.37) was used [88]. The crosslink density for MACOPS was determined to be 2.1 x 10^{-3} (± 1.0 x 10^{-4}) mol/cm^3. The presence of crosslinking explains why the unbroken samples of MACOPS returned almost completely back to their original shape after flexural bend testing. In the linear elastic region, there is firstly uncoiling of chains and secondly stretching of bonds. Failure is a result of the breaking of bonds [101]. Thus the unbroken samples were still in the elastic region which results in the recoiling of chains after the load is removed. Very little plastic deformation took place. Furthermore, homopolymerization of styrene monomer may occur resulting in a more rigid matrix. The MACOPS samples did not dissolve in the toluene solvent which also points to the presence of crosslinking.

The presence of crosslinking points to the presence of a network structure. Comparing the result to the crosslink density found for COMG-styrene co-polymer of 1.72 x 10^{-3} mol/cm^3 [9], a higher crosslink density was achieved in this study. It should, however, be noted that Campanella *et al*. used a different technique to estimate crosslink density. Campanella et al. used DMA (dynamic mechanical analysis) and the rubber elasticity theory to determine the crosslink density [9]. It should also be noted COMG co-polymer was made from the monoglyceride, unlike the triglyceride used here.

4.2 Property testing

4.2.1 Impact testing

The impact strength measures the amount of energy absorbed by the material before fracture. HIPS had the highest impact strength of 58.4 kJ/m^2. General purpose PS had the lowest impact strength (33.9 kJ/m^2) due to its brittle nature. The MACOPS matrix and reinforced composite had an impact strength of 41.5 kJ/m^2 and 45.0 kJ/m^2, between that of HIPS and PS. The impact strengths of the tested materials are shown graphically in Figure 31. Charpy impact tests, like other mechanical tests, for MACOPS have not yet been reported in the literature. In the images that follow, error bars indicate the standard deviation of the mean.

The impact strength for HIPS is consistent with that reported in the literature by Katime *et al*. [102], 64.7 kJ/m^2.

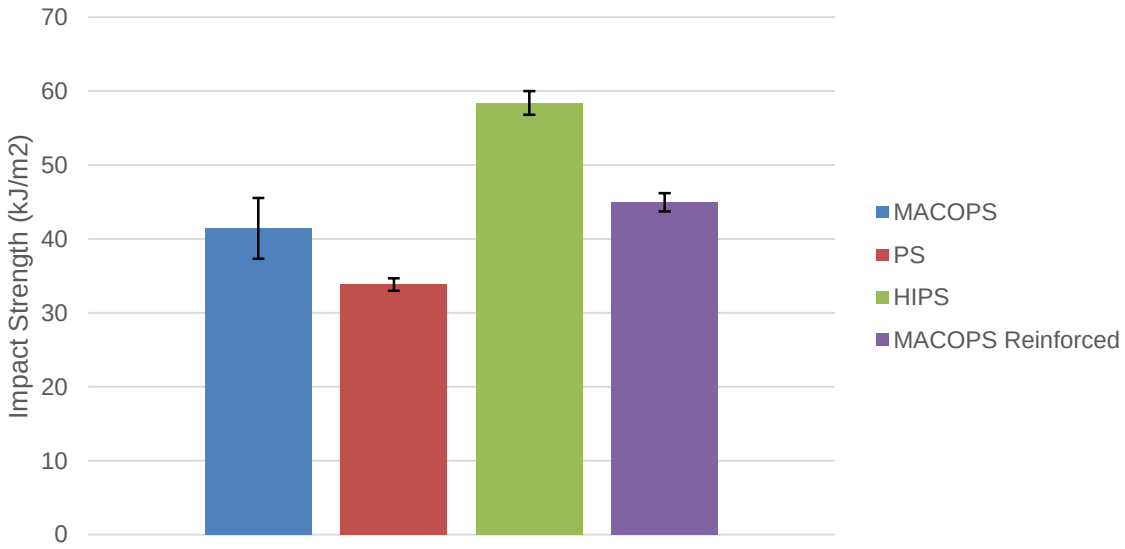

Figure 31: Impact strength comparison between the tested materials

When looking at the fracture surface of the reinforced MACOPS impact sample (Figure 32), a similar type of fibre pull-out (as seen in the tensile results for the reinforced sample) is present with the fibre strand breaking at different lengths. Voids and signs of delamination are also visible. It is likely (see later results) that the interfacial bond strength between the matrix and the reinforcement is weak. This is known to increase toughness [103].

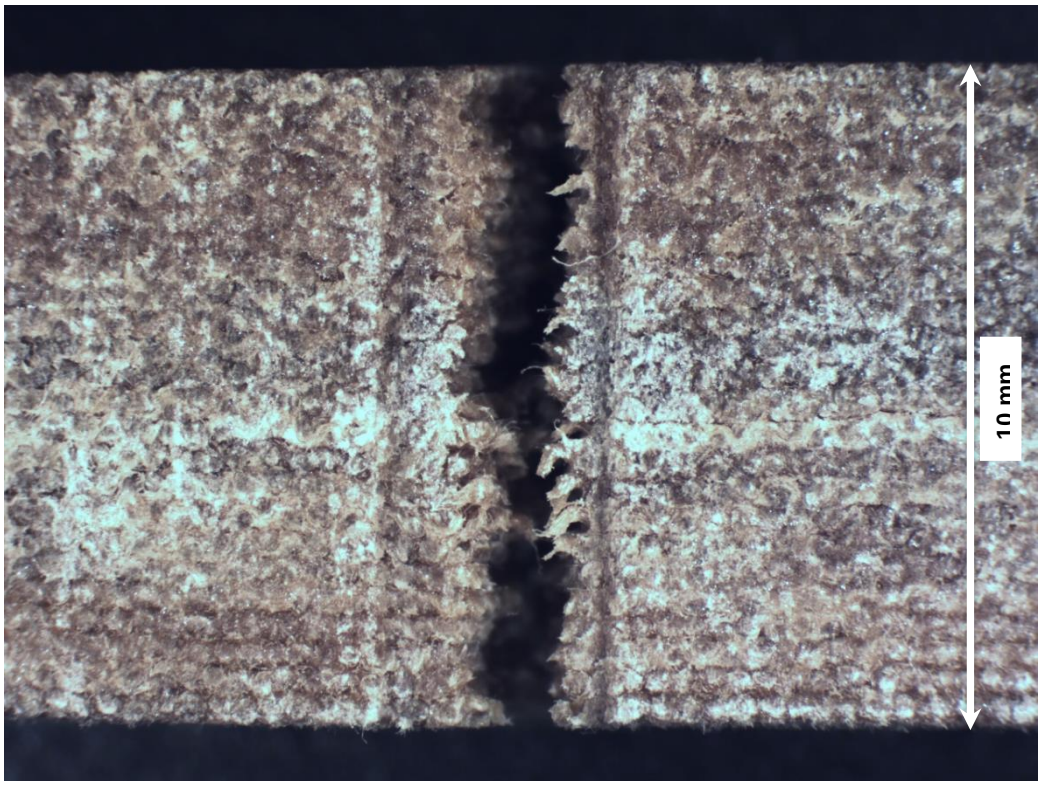

Figure 32: Impact fracture of reinforced MACOPS (notch facing up)

4.2.2 Tensile testing

The tensile stress-strain curve for neat MACOPS can be seen in Figure 33. Although a thermoset, as evidence by it being partially crosslinked, the material is not brittle. The ultimate tensile strength (UTS) was determined to be 23.0 (± 0.6) MPa. Young's modulus of 983 (± 122) MPa was found for the neat MACOPS. Tensile tests have not yet been conducted on this polymer before. The modulus is half that reported by Campanella *et al.* (1955 MPa) but it should be noted that the modulus reported by Campanella *et al.* was measured using dynamic mechanical analysis. Furthermore Campanella *et al*. are reporting on a monoglyceride derived polymer, unlike the triglyceride studied here.

The data compares favourably to a polyurethane polyol, based on a castor oil, synthesized by Zhang *et al.* The PU-CCP polymer had a UTS of 29.1 MPa, a Young's modulus of 495.3 MPa and a toughness of 2.84 MPa [48]. The toughness of the MACOPS, synthesized in this study was 2.53 (± 0.53) MPa.

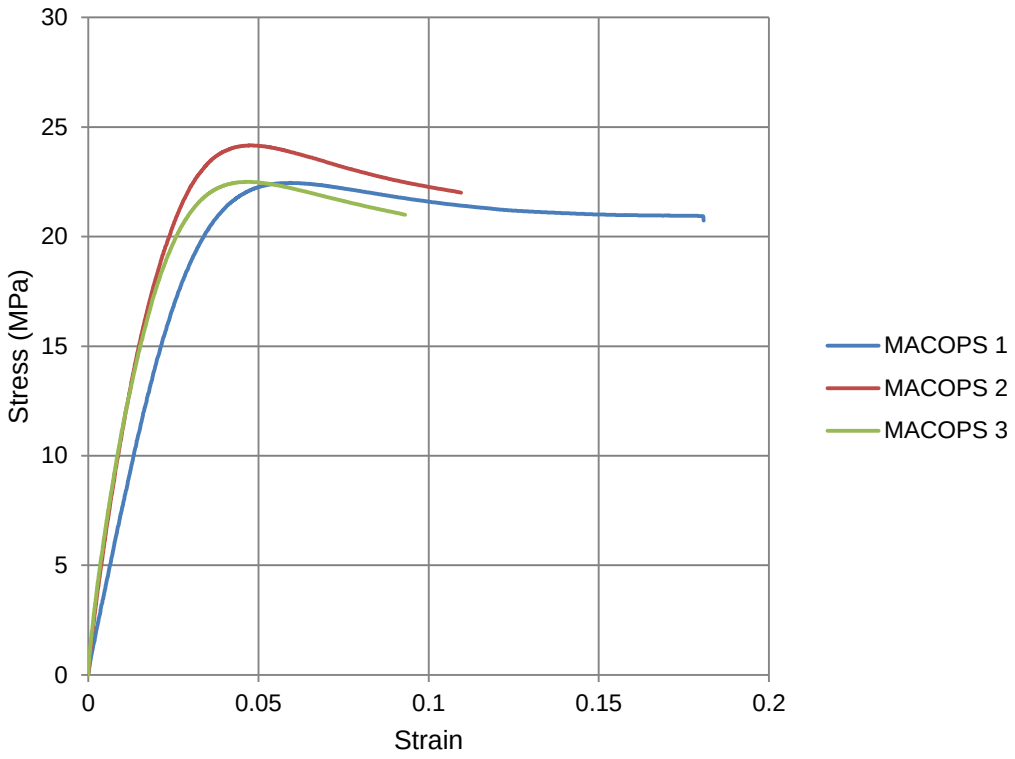

Figure 33: Tensile stress-strain curves for neat MACOPS

Striations can be seen on the fracture surface in Figure 34. Crack initiation is seen at point A followed by outward striations. No shear lips are seen indicating a brittle mode of final fracture despite the yielding observed and significant strain at break when compared to GPPS (Figure 35). The linseed oil monoglyceride maleate/styrene co-polymer synthesized by Mosiewicki et al. also showed a smooth fracture surface thus resulting in a brittle fracture mode. Mosieiwicki et al. states that this fracture mode is usually seen in crosslinked resins [104]. In this case the fracture surface of the MACOPS is similar to crosslinked resins as MACOPS is partially crosslinked, consisting of networks of a crosslinked co-polymer and homopolymerized polystyrene.

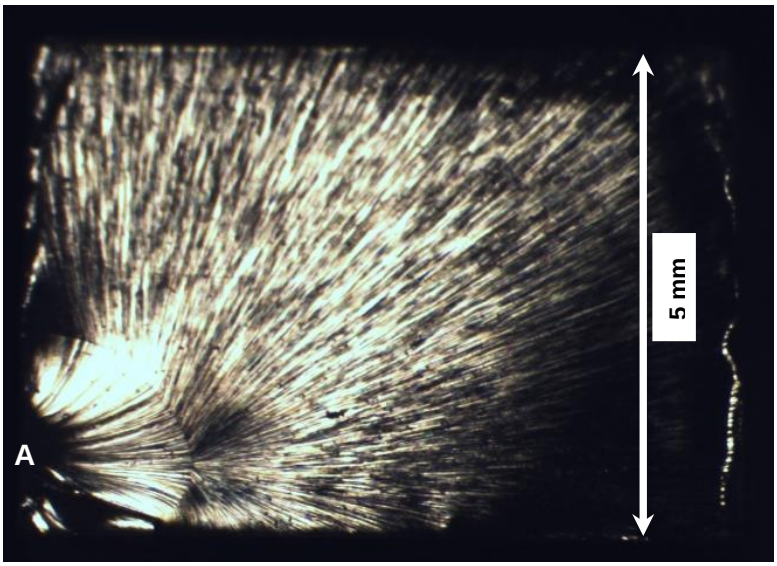

Figure 34: Tensile fracture surface for neat MACOPS

General purpose polystyrene shows brittle behavior under tensile stress. The strain at break was the lowest of all materials tested (<2%) and no appreciable yielding could be discerned in the stress-strain curves. Young's modulus at 3.27 (± 0.06) GPa and the maximum tensile strength of 44.8 (± 0.5) MPa are higher than MACOPS. These properties are in line with the literature values: UTS for GPPS is reported as 46 MPa and the Young's modulus as 2.9 GPa [105].

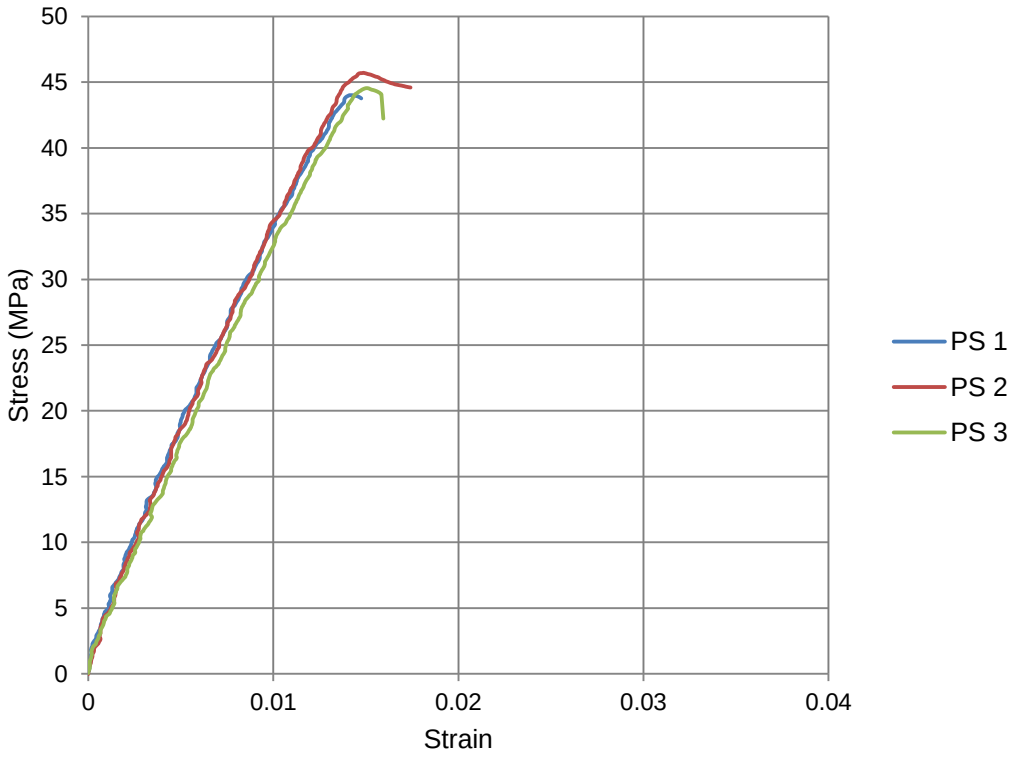

Figure 35: Tensile stress-strain curves for general purpose polystyrene

Due to the brittle nature of GPPS a unique fracture surface is observed (Figure 36). Numerous cracks are observed causing shattering in the sample. Due to rapid crack propagation, cracks are formed and propagate in different directions from the point of crack initiation.

The stress-strain curve for HIPS is seen in Figure 37. Some key-differences are the amount of elongation before break, which is clearly greatest for HIPS. Unlike MACOPS, a slight increase in the stress can be seen towards the strain at break. Young's modulus and UTS were determined to be 1.51 (± 0.06) GPa and 13.52 (± 0.02) MPa respectively. The modulus is in line with that reported in the literature, 1.7 GPa, although the UTS of the sample, tested in this study, is significantly lower than that found in the Polymer Handbook, 24 MPa [105]. The value, however, is more in-line with other authors such as Katime *et al*. [102] who reported 25, 17 and 14 for different grades of HIPS. The shape and extension at break is consistent with the weaker grades of HIPS [102]. Katime *et al*. [102] reported a Young's modulus of 0.94 GPa for the weakest grade.

A shear lip can be seen in the failure surface in Figure 38, indicative of ductile failure.

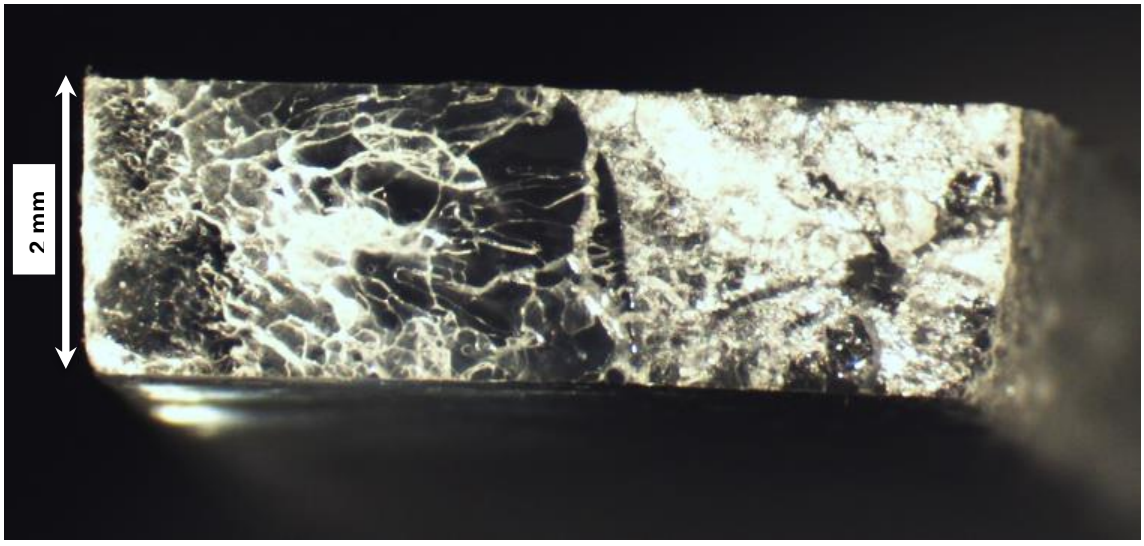

Figure 36: Tensile fracture surface of general purpose PS

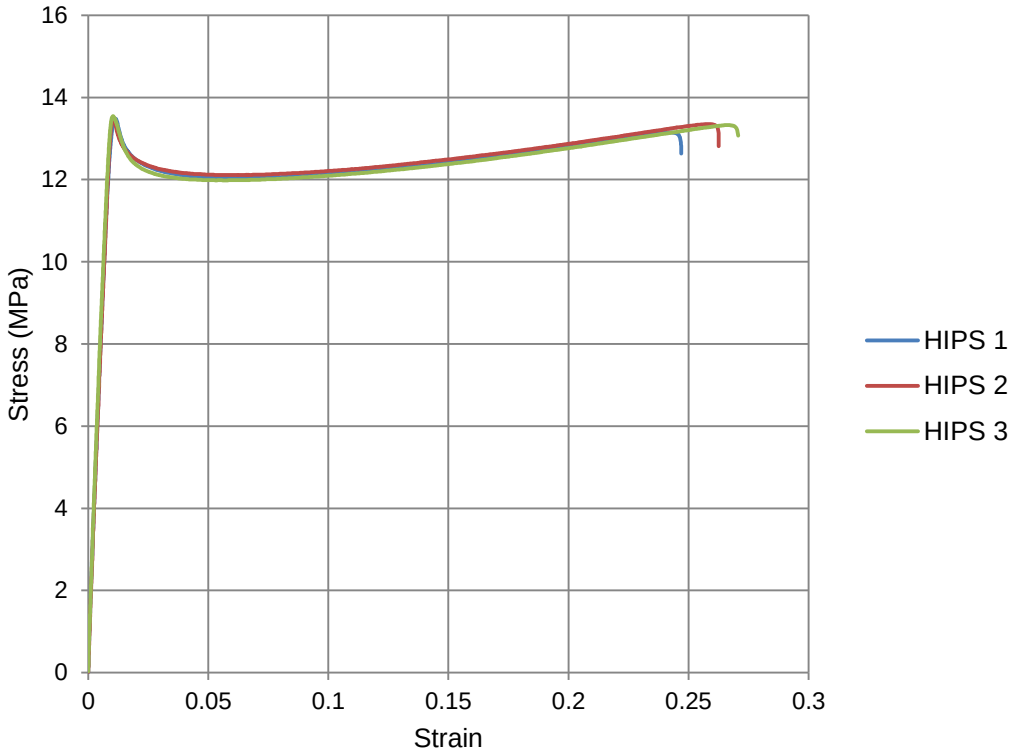

Figure 37: Tensile stress-strain curves for HIPS

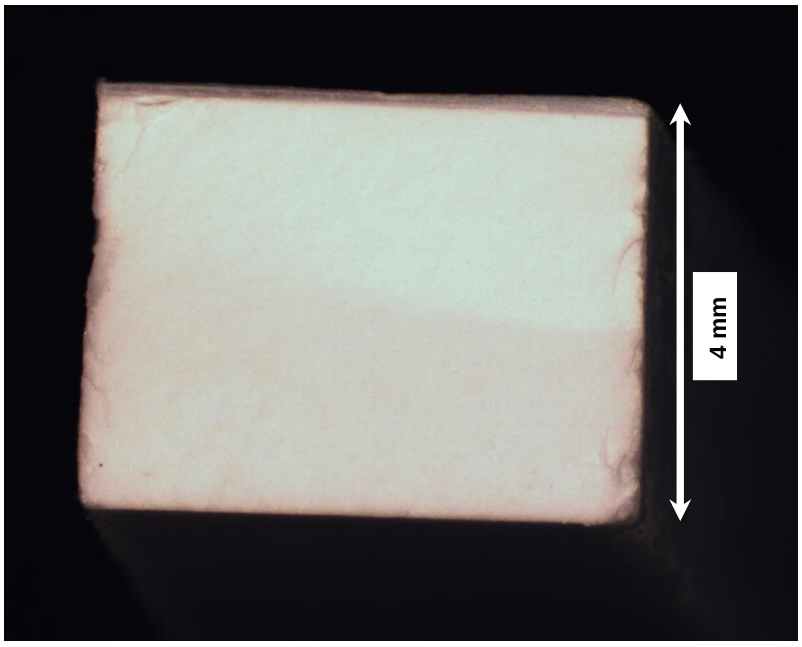

Figure 38: Tensile fracture surface of HIPS

Tensile tests on reinforced MACOPS composites have not previously been reported. The reinforced MACOPS has lower modulus and UTS than the neat MACOPS matrix, which is not expected for reinforced composites. It is possible that there is limited interaction between the resin and the fibre as the resin most likely contains areas of homopolymerized polystyrene. The non-polar polystyrene not wet the polar cellulosic fibres well. The Young's modulus for the reinforced MACOPS was determined as 283 (± 15) MPa with a UTS of 13.1 (± 1.1) MPa. Both of these values are below those of MACOPS which would suggest that the fabric, used in this study, is not reinforcing.

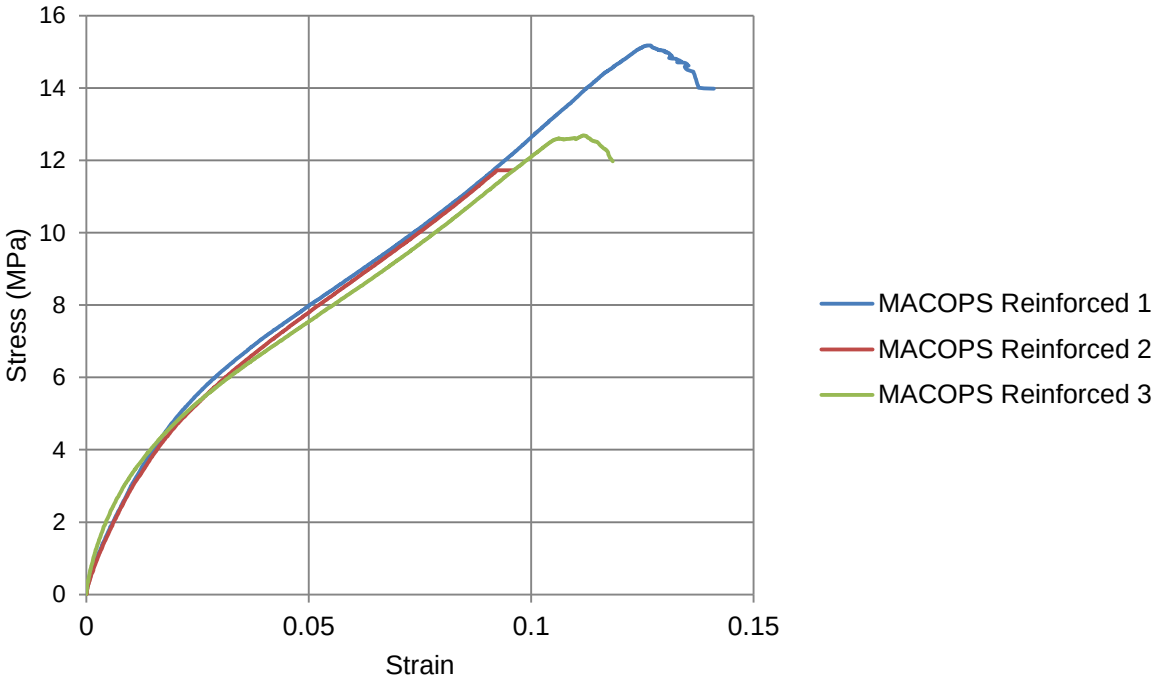

Figure 39: Stress-strain curves for reinforced MACOPS

The shape of the stress strain curves in Figure 39 is not typical of a fibre reinforced material, which tend to be more linear.

The side-on photograph of the fracture surface (Figure 40) shows a very uneven surface caused by the fibres breaking at different lengths. The top of the fracture surface (Figure 41) does not show visible signs of delamination but some voids due to insufficient wetting.

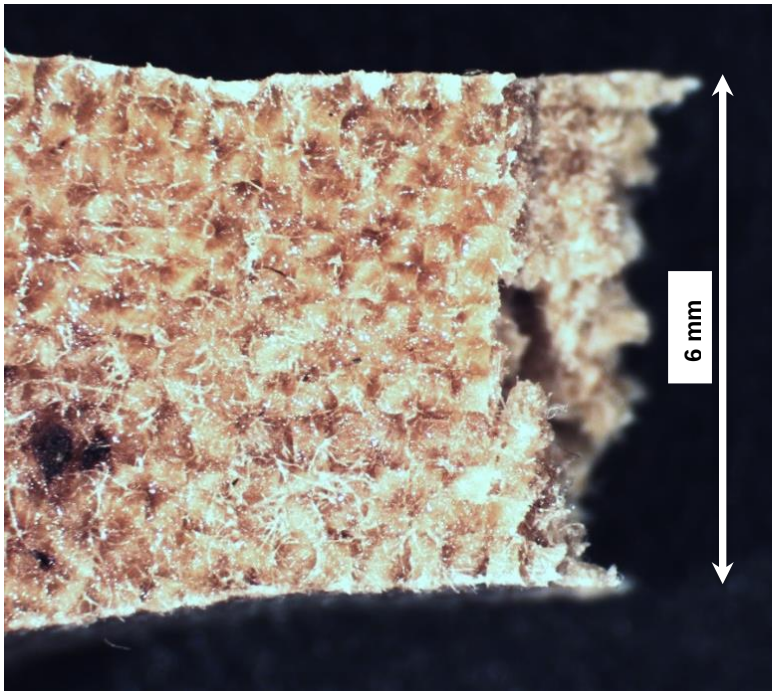

Figure 40: Side-on tensile fracture surface of reinforced MACOPS

By comparing the stress-strain curves for the different materials, information on the strain at break and toughness can be obtained. The strain at break for MACOPS is about seven times more than the strain at break for GPPS and half of the strain at break for HIPS. The average strain of break of the MACOPS and reinforced MACOPS sample are very similar suggesting that it is matrix failure that leads to eventual fracture.

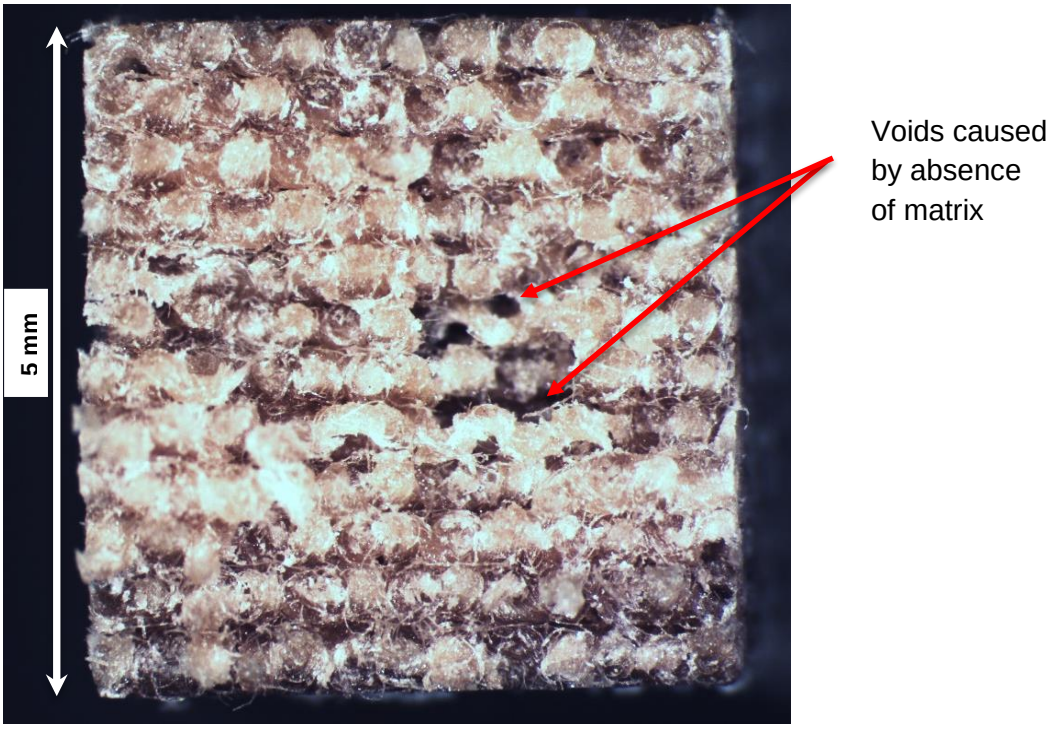

Figure 41: Tensile fracture surface of reinforced MACOPS

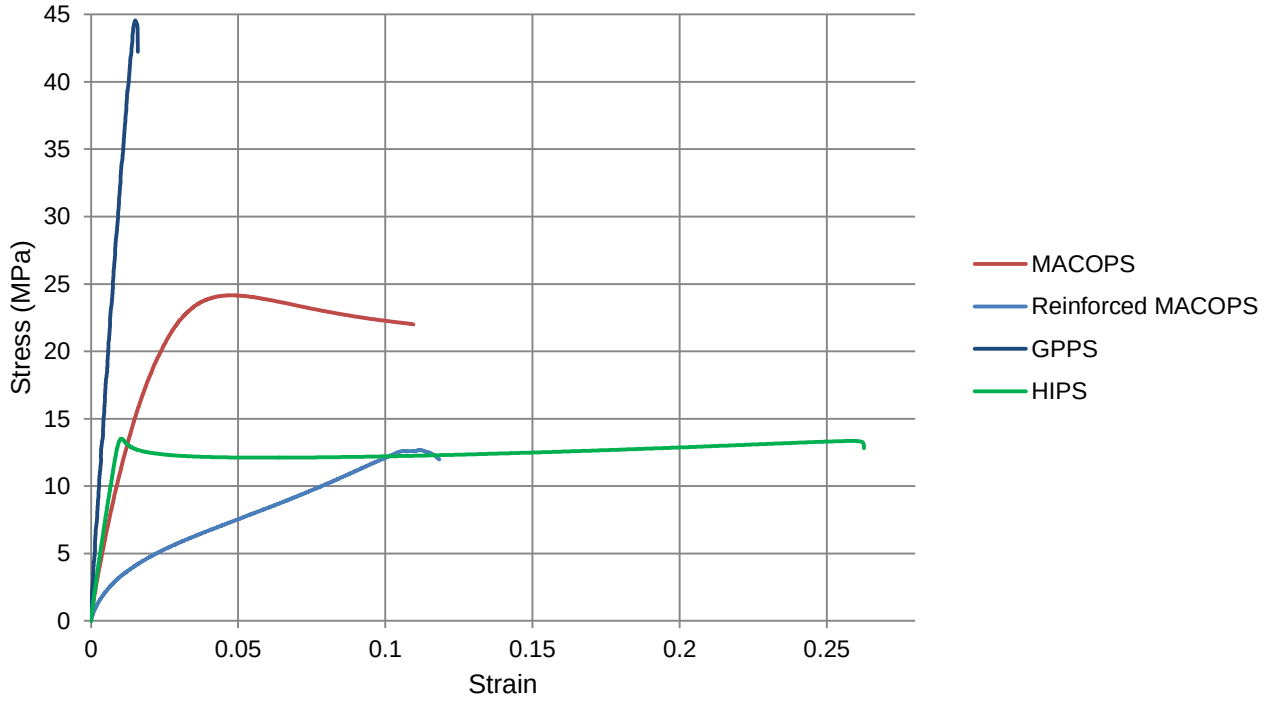

Figure 42: Comparison between different tensile stress-strain curves of representative samples

Table 10: Tensile properties of the tested materials

Material	Young's modulus (GPa)	UTS (MPa)	Tensile toughness (MPa)	Strain at break
MACOPS	1.0 (± 0.1)	23.0 (± 0.6)	2.53 (± 0.53)	0.128 (± 0.027)
Reinforced MACOPS	0.3 (± 0.02)	13.1 (± 1.1).	1.00 (± 0.19)	0.118 (± 0.013)
GPPS	3.3 (± 0.06)	44.8 (± 0.5)	0.61 (± 0.16)	0.016 (± 0.001)
HIPS	1.5 (± 0.06)	13.5 (± 0.02)	3.19 (± 0.10)	0.258 (± 0.008)

Note: the values in brackets refer to the standard deviation of the mean (S/√N) in all tables

Considering the area under the curve, HIPS and MACOPS have values that are closer to each other than they are to GPPS. GPPS has the lowest toughness and extremely low strain at break which is consistent with its brittle nature. With respect to Young's modulus, the MACOPS polymer and HIPS were also closest. The reinforced MACOPS composite underperformed.

To determine why the reinforced MACOPS had such weak mechanical properties, the mechanical properties of the fibre yarns were determined. The stress-strain curves for individual greige fibres can be found in Appendix B. 100% hemp fibres were included for comparison.

Stress calculated using area determined by measurement

The average diameter of the greige fibres was measured as 402.6 µm and the area determined as 0.127 mm^2. 100% hemp fibres, used for comparison, had a diameter of 350.0 µm and a cross-sectional area of 0.096 mm^2.

The UTS and Young's modulus for the greige fibres were determined as 40.7 (± 0.91) MPa and 0.95 (± 0.09) GPa respectively. For the hemp fibres a UTS of 138.6 (± 14.9) MPa and a Young's modulus of 2.5 (± 0.4) GPa was found. The pure hemp fibre has a 70% higher UTS than that of the greige fibre. It should be noted that greige fibre also contains weaker (compared to hemp fibre) cotton filaments (as seen in Table 7) when comparing the modulus and UTS. The mechanical properties are summarized in Table 11. These values are significantly lower than those in Table 7. This is because the data, reported here is for yarns, and not individual filaments. In yarns each filament breaks. The greige fibres are expected to be weaker because of the incorporation of cotton which is weaker and has a lower modulus than hemp [54, 55].

Table 11: Mechanical properties of greige and hemp fibres with a cross-sectional area determined by measurement

Fibre	Diameter (µm)	Area (mm^2)	UTS (MPa)	Young's modulus (GPa)
Greige	402.6	0.127	40.7 (±1.6)	0.95 (±0.16)
Hemp	350.0	0.096	138.6 (±25.8)	2.5 (±0.7)

For both the greige and hemp fibres, the stepwise failure of the fibres and stepwise decrease in stress after the yield point is indicative that both of these fibres are actually made up out of a bundle of thinner fibres (this is also seen in the SEM micrograph as explained in Section 4.3.2).

This could be one of the reasons that the properties of the reinforced MACOPS composite was poor. Firstly, the greige fibres used are weak compared to pure hemp fibres and secondly the fact that a yarn consists out of a bundle of multiple thin fibres also contributes to weakened properties. In the paper by Farouk *et al.* it was shown that voids have a negligible effect on the longitudinal tensile modulus of woven fibre composites [106]. The poor tensile properties are likely due to the physical nature of the fibre used as a reinforcement. The greige fibre reinforcement acts only as a filler and does not contribute structurally to the composite.

4.2.3 Efficiency of the fibre reinforcement

The theoretical modulus was calculated for the Young's modulus of the greige fibres using the method mentioned in section 4.2.2.

Table 12: Efficiency of fibre reinforcements

Method	E_f (MPa)	E_m (MPa)	E_T (MPa)	E_L (MPa)	E_C (theoretical) (MPa)	E_C (experimental) (MPa)	Efficiency (%)
A	954	983	975	975	975	283	29.0

E_f = Young's modulus for fibre reinforcement; E_m = Young's modulus for matrix; E_T = Young's modulus (transverse); E_L = Young's modulus (longitudinal); E_C = Young's modulus for composite

The model used (combination of rule of mixtures and Halpin-Tsai) predicts an upper limit for elastic modulus [93, 94] based on the properties of the constituents. For both cases the reinforced composite was less than 30% efficient. The poor efficiency also points to the presence of voids which results from insufficient wetting of the fibres. Insufficient wetting can be caused by chemical incompatibility between the resin and areas of homopolymerized polystyrene. The difficulties experienced with tight weave greige fabric has already been noted.

4.2.4 Flexural (3-point bending) testing

Flexural tests for a MACOPS polymer have not yet been reported in literature. The flexural stress-strain curve for neat MACOPS can be seen in Figure 43. The curve represents that of a flexible thermoset with high toughness. The maximum flexural strength was determined to be 22.1 MPa (± 1.1). For comparison the MACOPS polymer was compared to a MACO/epoxy blend synthesized by Ray *et al.* [39]. The MACO-epoxy blend showed a flexural strength of approximately 40 MPa compared to the 22 MPa of the MACOPS matrix. The reason for this could be due to the MACO-epoxy blend having a higher crosslink density in comparison to MACOPS, restricting chain movement due to chain entanglement [39] and thus increasing the stiffness of the MACO-epoxy blend.

The fracture surface of MACOPS can be seen in Figure 44. At point A crack initiation is observed with visible striations. In area B a shear lip is present, indicating a small amount of ductile fracture. The high flexibility of MACOPS was observed by the formation of a definite U-shape during testing (seen in Figure 45).

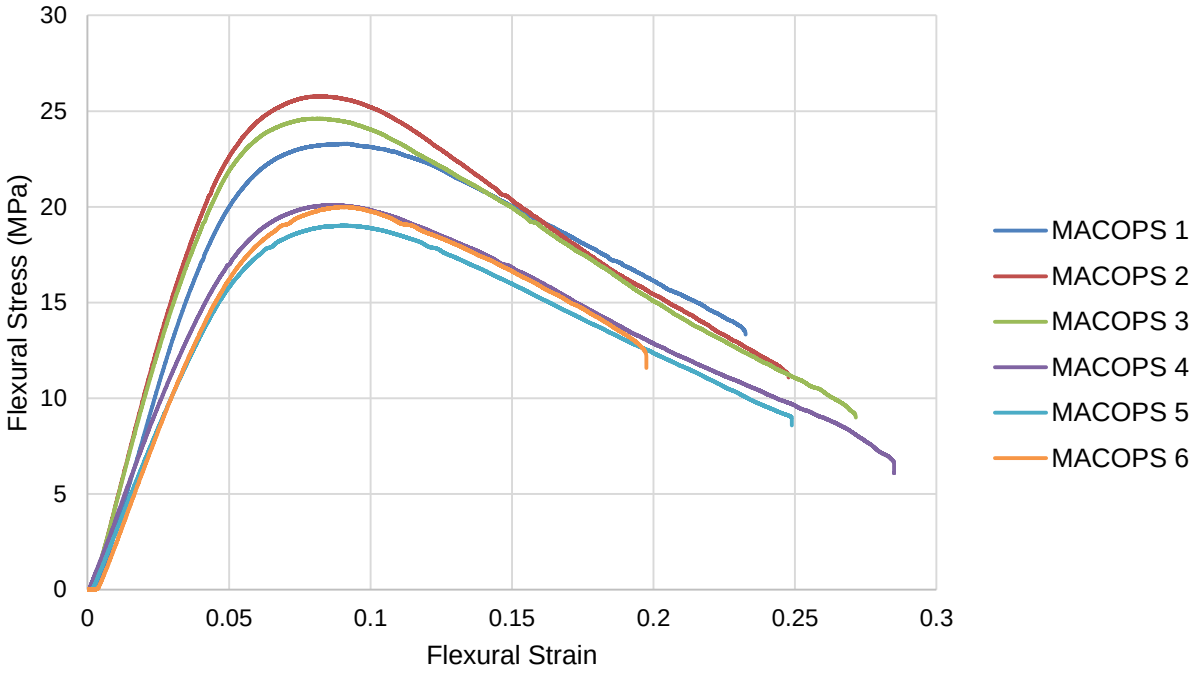

Figure 43: Flexural stress-strain curve for neat MACOPS

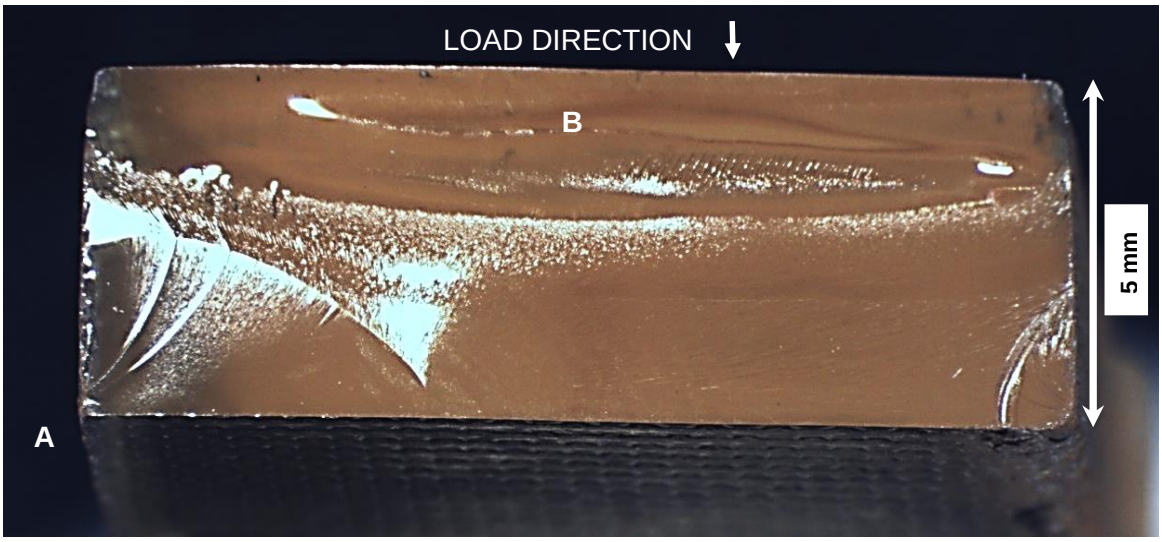

Figure 44: Flexural fracture surface of MACOPS

Figure 45: MACOPS showing a U-shape during 3-point bend testing

Figure 46 shows the stress-strain curves for the MACOPS reinforced with woven greige fibres. The curves have a lower slope than that of the MACOPS (Figure 43). This is consistent with what seen during tensile testing. The noise/jerkiness in the curves took place as soon as delamination started to occur in the samples. Sample 1 and 5 showed the most delamination (Figure 47) and thus the largest drop in stress.

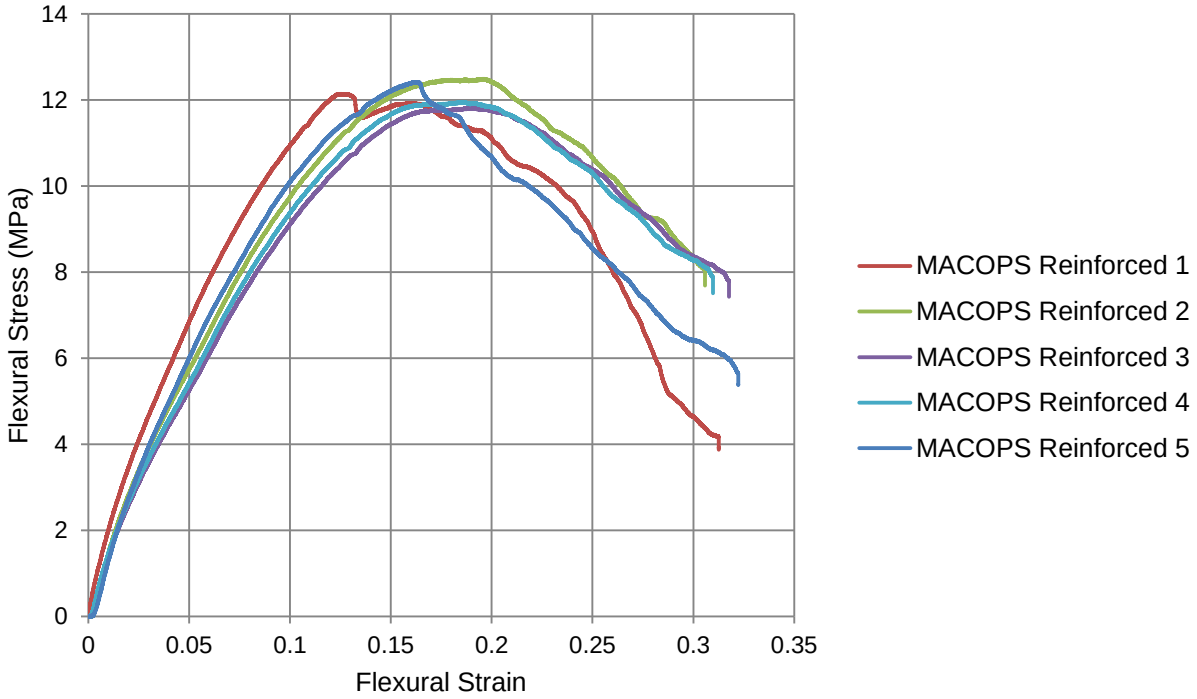

Figure 46: Flexural stress-strain curve for Reinforced MACOPS

It is important to note that none of the reinforced samples broke. The test had to be aborted due to the samples slipping through the supports. The maximum flexural stress for the MACOPS reinforced with greige fibres was determined to be 12.2 (± 0.1) MPa.

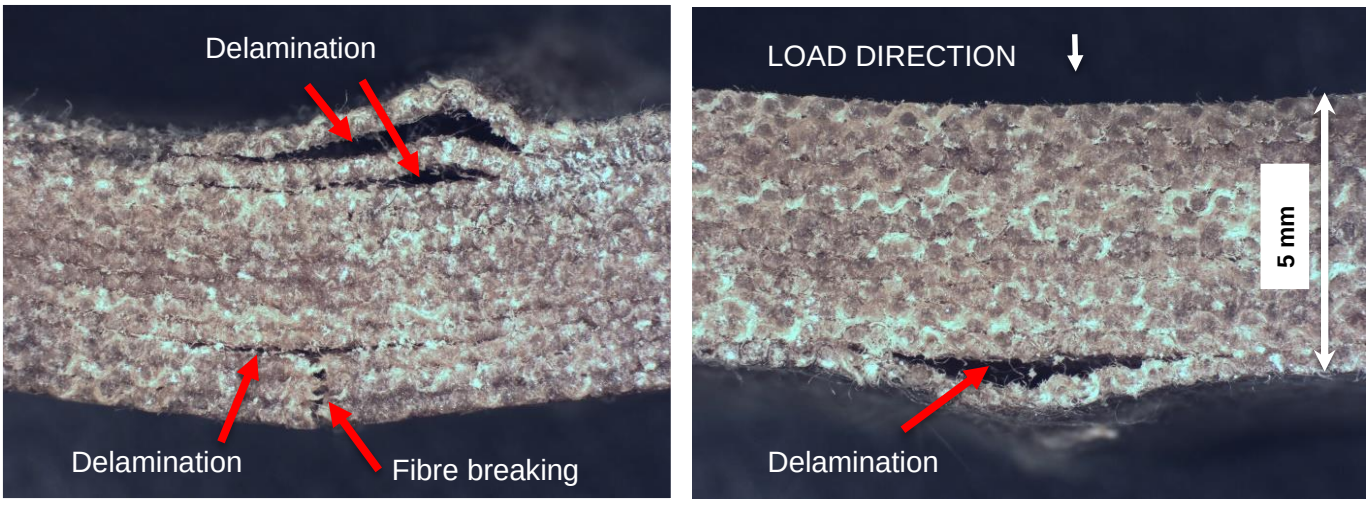

Figure 47: Side-on view of delamination present in the reinforced MACOPS

Comparing the reinforced MACOPS to the MACO/jute reinforced composite produced by Mistri *et al.*, the flexural strength for MACOPS is in line with other natural reinforced composites. Their MACO/jute composite had a flexural strength of approximately 15 MPa [14] which is comparable to the flexural strength of 12.2 MPa found for the reinforced MACOPS composite.

General purpose polystyrene (GPPS) displays a characteristic flexural stress-strain curve for a brittle and hard thermoplastic (Figure 48). The maximum flexural stress was determined as 74.4 (± 0.7) MPa. The sample itself displayed some crazing around the fracture area (Figure 49) with a brittle fracture surface. Crazing is expected for glassy thermoplastics and forms due to the formation of localized areas of plastic deformation perpendicular to the direction of the applied load [101].

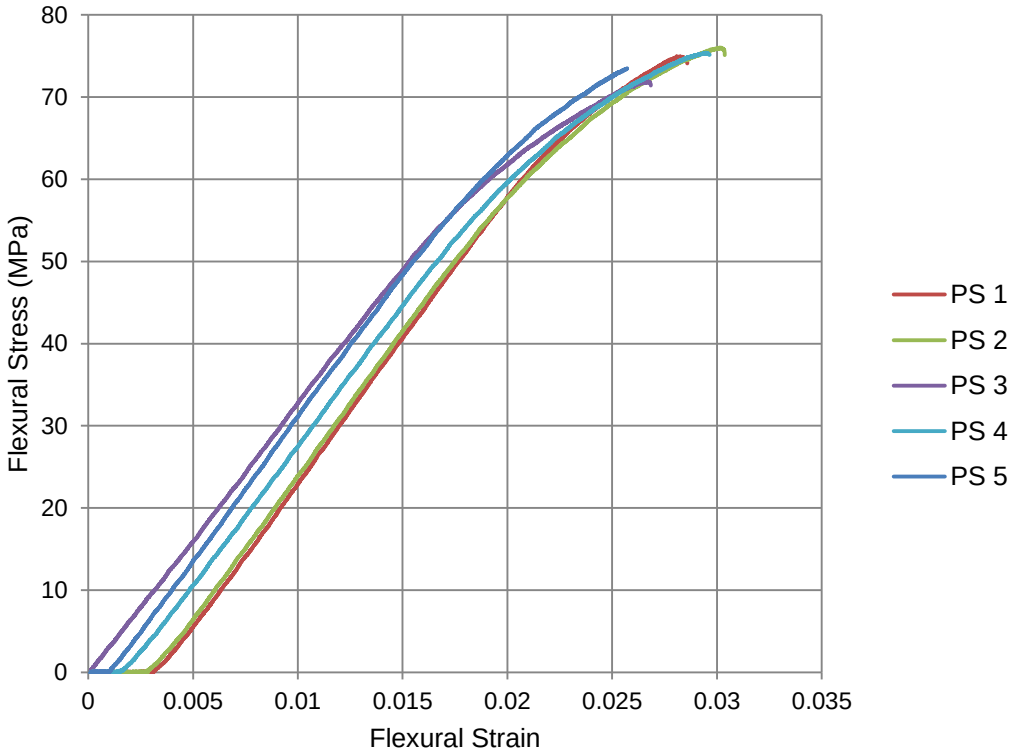

Figure 48: Flexural stress-strain curves for general purpose polystyrene (PS)

High impact polystyrene (HIPS) has a slightly higher slope for the linear elastic region than MACOPS as seen in Figure 50. This overall curve is characteristic of a tough thermoplastic. The maximum flexural stress for HIPS was determined to be 27.2 (± 0.2) MPa. According to literature the flexural strength for HIPS is expected to be approximately 46 MPa [107]. Similar to the UTS, the flexural strength is less than that reported in the literature, indicative of a weaker grade.

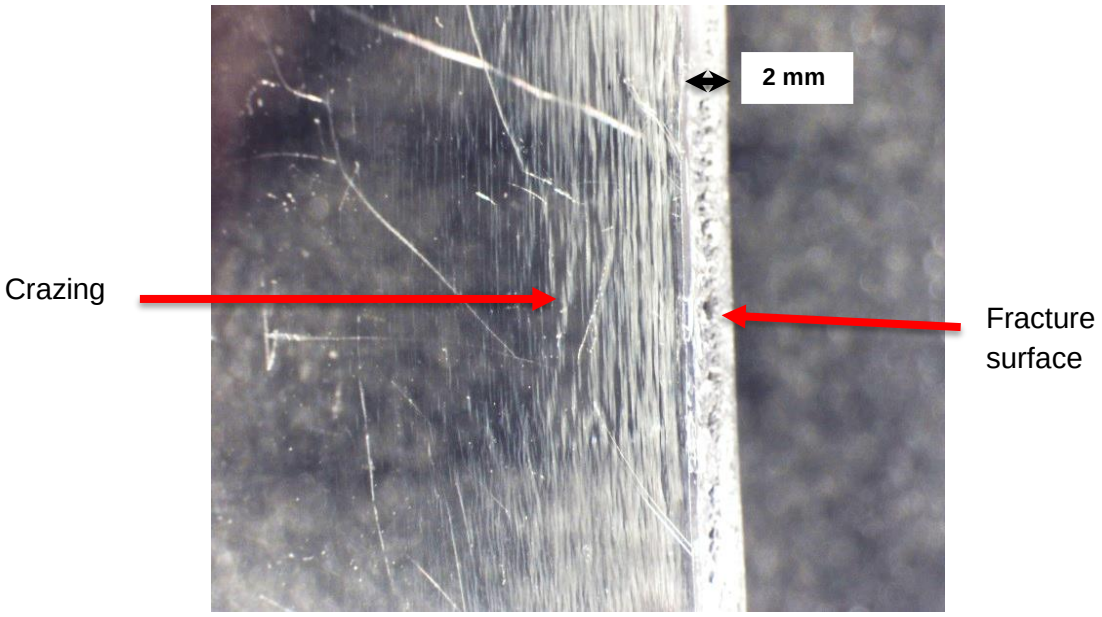

Figure 49: Crazing near the flexural fracture surface of PS

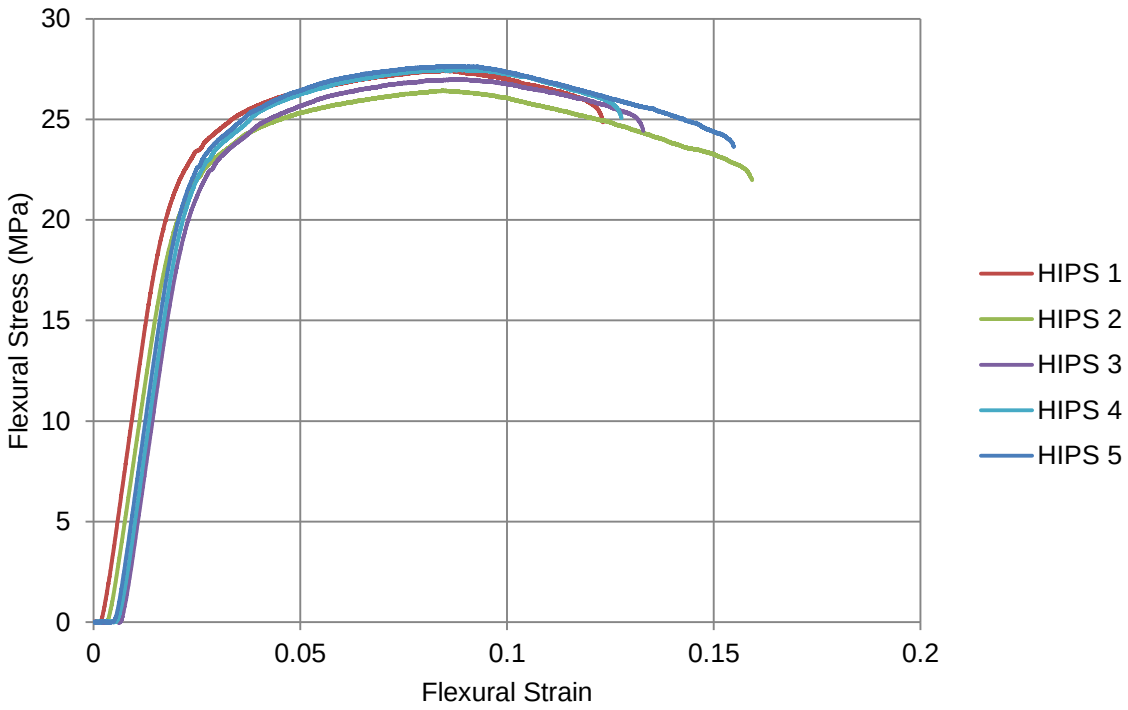

Figure 50: Flexural stress-strain curve for high impact polystyrene (HIPS)

The flexural fracture surface for HIPS (Figure 51) shows a clear shear lip on the edge where the load was applied. This behaviour is similar to that seen in tensile failure (Figure 38).

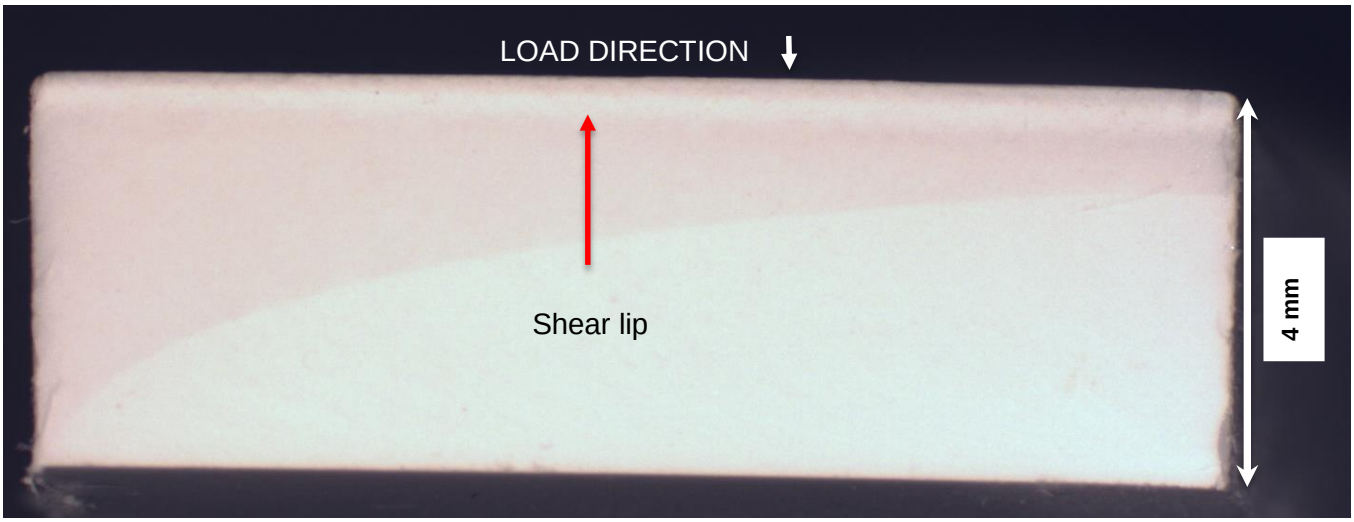

Figure 51: Flexural fracture surface of HIPS

Table 13 summarizes the flexural properties of the tested materials. Comparing the synthesized polymer and composite with the commercially available polymers mentioned above (HIPS and PS), it was observed that the maximum flexural stress of the neat MACOPS is closer to that of HIPS than PS (seen in Figure 52). Under flexion, the strength of the MACOPS matrix decreased when the reinforcement was added. This is ascribed to the large amount of delamination that took place that gave a false representation of the flexural properties of the composite. Furthermore the unconventional decrease in flexural strength may be due to the presence of voids. The flexural strength of a composite can decrease up to 10% per 1% increase in voids [77].

A comparison between the flexural stress-strain curves for the tested materials can be seen in Figure 52. The strain at break for MACOPS under flexural loads is about twice the stain at break for HIPS and about 9 times that of GPPS. This is indicative of the high extensibility of the material. The high toughness of MACOPS and HIPS is consistent with the results seen for Charpy impact and tensile testing. Interestingly under 3-point bending conditions MACOPS is more extensible than HIPS and has lower UTS which is the inverse of what is seen under tensile testing

Table 13: Flexural properties for the tested materials

Polymer	Flexural Strength (MPa)	Flexural toughness (MPa)	Strain at break
MACOPS	22.1 (±1.1)	3.94 (± 0.26)	0.247 (±0.013)
GPPS	74.4 (±0.7)	1.12 (±0.02)	0.028 (±0.0003)
HIPS	27.2 (±0.2)	3.24 (± 0.17)	0.140 (±0.007)
Reinforced MACOPS	12.2 (±0.1)	> 2.76 (± 0.02)	> 0.314 (±0.003)

Note: the values with a "> than", are due to the fact that the samples did not break during testing

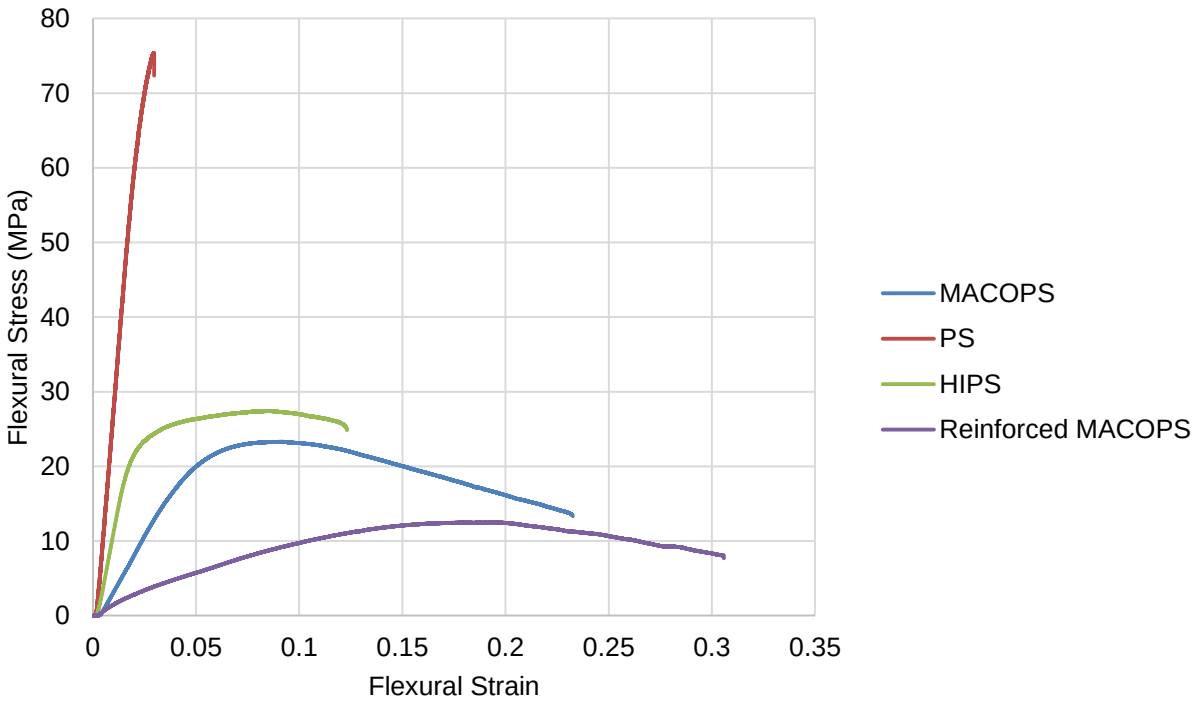

Figure 52: Comparison between flexural stress-strain curves of representative samples

4.2.5 Hardness testing

The results for the Shore-D hardness measurements can be seen in Table 14. Note that for GPPS which had a sheet thickness of 2 mm, two samples were stacked on top of each other before measurements were taken to ensure that the hardness of the surface underneath did not influence the value obtained.

Table 14: Shore-D hardness for the tested materials

Sample	Shore-D hardness
MACOPS	60.5 (± 0.9)
Reinforced MACOPS	68.0 (± 0.7)
HIPS	76.9 (± 0.2)
GPPS	85.0 (± 0.1)

Shore-D hardness tests can provide useful information on the indentation resistance of materials [108]. Materials with a higher Shore-D hardness have a higher resistance to indentation and vice versa. GPPS has the highest resistance to indentation followed by HIPS and lastly the MACOPS composite and matrix. According to literature polystyrene should have an approximate hardness value of at least 70 [108].

4.2.6 Density of the polymer and composite samples

For the determination of density, the density bottle method was chosen due to accuracy and reproducibility of the method. Distilled water was used as the liquid due to its known density.

The density test was repeated three times with different sample masses. The densities of the different materials can be seen in Table 15.

Table 15: Average densities of the different materials

Sample	Average Density (g/cm^3)	Density from Literature (g/cm^3)	Reference
MACOPS	1.034 (± 0.003)	Not available	-
Reinforced MACOPS	1.002 (± 0.014)	Not available	-
HIPS	1.005 (± 0.039)	1.03 – 1.06	[105, 109]
GPPS	1.087 (± 0.003)	1.04	[105, 109]

Theoretically the expected density of the reinforced MACOPS composite can be calculated using the rule of mixtures (as seen in section 3.3.7). The theoretical density for the reinforced MACOPS composite was determined to be 1.01 g/cm^3. As the reinforcement is less dense than the matrix, an increase in the density of the matrix is not expected after reinforcement.

4.2.7 Specific strength and specific toughness

The specific strength or strength-to-weight ratio for the tested materials under tensile and flexural load was calculated. A higher strength-to-weight ratio is preferred when considering materials for applications such as aerospace or automotive applications [110]. Table 16 shows the specific tensile and specific flexural strengths of the tested materials as well as the specific toughness.

Table 16: Specific strength of tested materials

Material	Average Specific Tensile Strength (Nm/kg)	Average Specific Flexural Strength (Nm/kg)	Specific Tensile Toughness (Nm/kg)
MACOPS	2.2×10^4 ($\pm$ 5.4×10^2)	2.1×10^4 ($\pm$ 1.1×10^3)	2.2×10^3 ($\pm$ 5.1×10^2)
Reinforced MACOPS	1.3×10^4 ($\pm$ 1.1×10^3)	1.2×10^4 ($\pm$ 1.3×10^2)	1.3×10^3 ($\pm$ 1.9×10^2)
GPPS	4.1×10^4 ($\pm$ 4.6×10^2)	6.8×10^4 ($\pm$ 6.8×10^2)	3.6×10^2 ($\pm$ 1.9×10^2)
HIPS	1.3×10^4 ($\pm$ 0.16×10^2)	2.7×10^4 ($\pm$ 2.2×10^2)	3.3×10^3 ($\pm$ 0.98×10^2)

From the results it can be seen that under tensile conditions, the MACOPS matrix has a higher specific strength (strength-to-weight ratio) than HIPS. Under flexural conditions HIPS has the higher strength to weight ratio. MACOPS has approximately equal flexural and tensile specific strengths. In applications where the materials is subjected to varying loads (both tensile and flexural), MACOPS will be a better candidate (according to the calculated specific strengths) than HIPS. This is due to the fact that MACOPS has better tensile and flexural properties per kilogram of material (meaning less material is required to obtain similar properties to HIPS). Reinforced MACOPS has the lowest strength to weight ratio of the tested materials. This is a result of poor wetting of the fibres which caused voids and areas of delamination. Although high specific strengths are preferred, the specific toughness should also be considered. GPPS has the highest specific strength under both tensile and flexural loads but its specific toughness is very low (compared to the other tested materials). In most applications where toughness is desired, a material like MACOPS will be chosen instead of GPPS regardless of the high specific strength of GPPS.

4.2.8 DSC analysis

The DSC thermogram for the MACOPS matrix (Figure 53) show two glass transition temperatures (T_g). The two T_g values are indicative of either a system where the two phases are phase segregated or an interpenetrating polymer network.

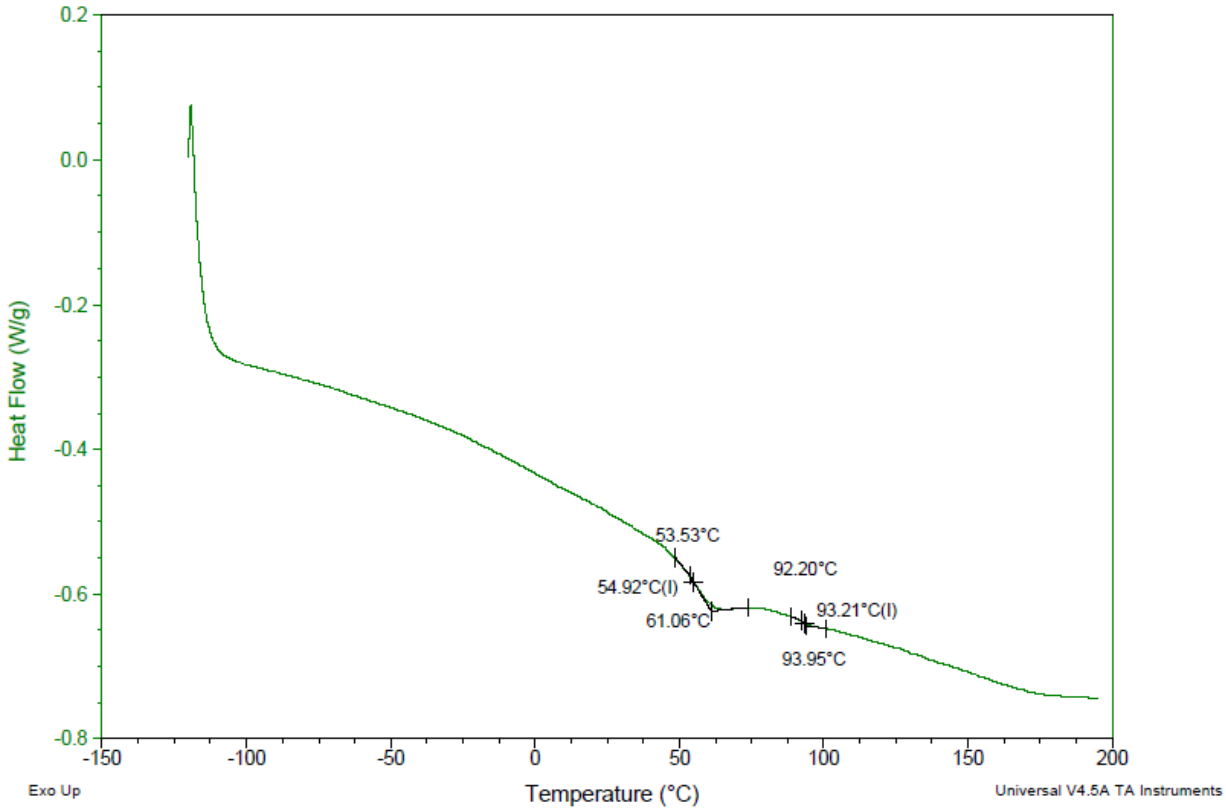

Figure 53: DSC thermogram for MACOPS

A glass transition can be seen at 93.2 ˚C and 54.9 ˚C. The T_g of 93.2 ˚C can be assigned to homopolymerised polystyrene. Polystyrene has a T_g of approximately 100˚C according to literature [88] although this depends on grade. Values as low as 93 ^oC have been reported [111]. The T_g of 54.9 ˚C is ascribed to the MACOPS co-polymer. Comparing the result to the T_g found for the castor oil maleated glyceride-styrene copolymer synthesized by Campanella *et al.* [9], the MACOPS T_g is significantly lower. Campanella *et al.* found a T_g of 121 ˚C for the synthesized COMG-styrene copolymer [9]. Unreacted sidechains in the triglyceride are more likely; thereby increasing free volume and so reducing the T_g.

The DSC thermogram for HIPS (Figure 54) only shows one T_g as the glass transition for polybutadiene is at ≈ -85.2 ˚C [88] (which was not included in the temperature range explored in the experiment). The T_g at 104.3 ˚C is assigned to the polystyrene segments in the system (expected to be in the range of 93 ˚C to 105 ˚C according to Brandrup *et al.* [105]). HIPS is a graft co-polymer which phase segregates [112], hence it has 2 glass transition temperatures.

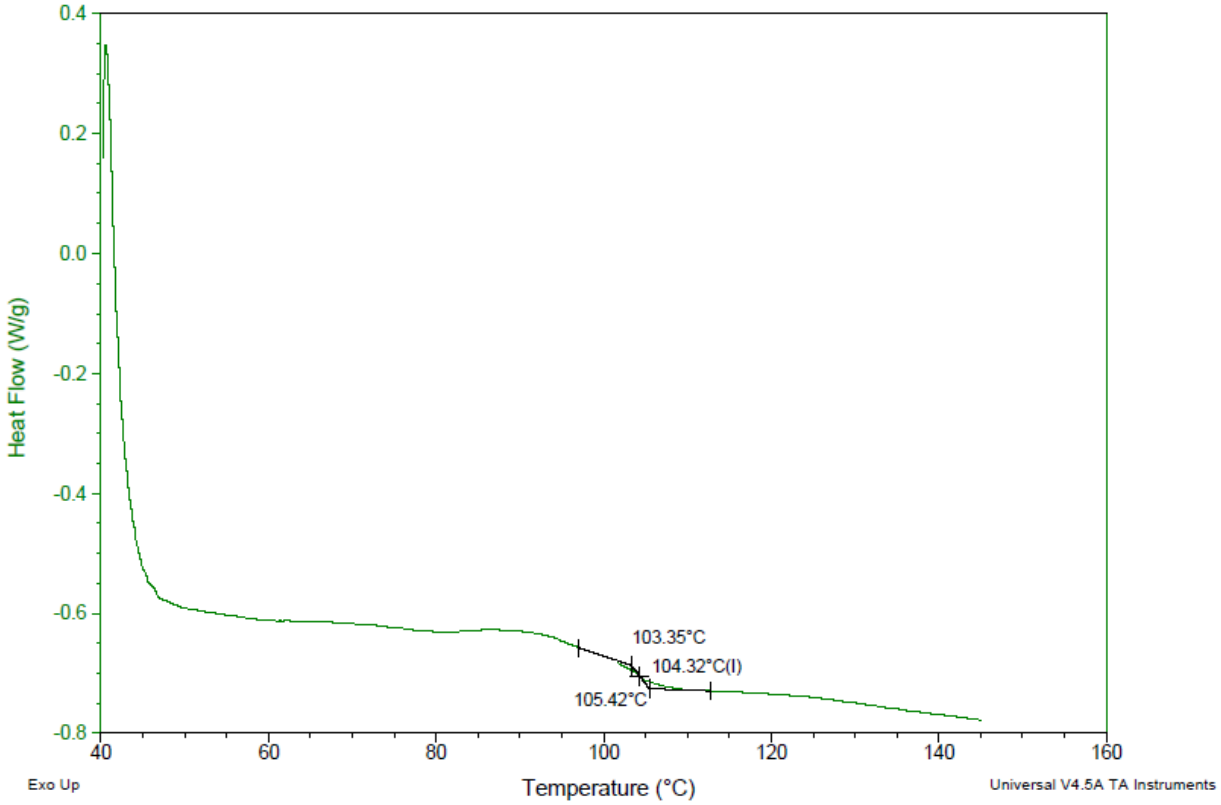

Figure 54: DSC thermogram for HIPS

For GPPS a glass transition temperature in the range of 74 ˚C to 110 ˚C is expected according to literature with most reported values in the range 90 to 105 ˚C [105].

4.2.9 Thermogravimetry

Thermogravimetry of the tested samples was performed to obtain information on the onset temperature of thermal degradation and compositional information. This information is very useful to determine suitable applications for the material.

Figure 55 shows the thermogravimetric thermogram for the MACOPS matrix. The extrapolated onset temperature for thermal degradation was determined as 336 ˚C. Another method of assessing thermal stability is to quote the 5% mass loss temperature. For MACOPS this was 304 ^{o}C. Maximum weight loss took place at a temperature of 396 ˚C. The thermogram suggests a multistage decomposition. This may be indicative of the relative stability of different segments of the MACOPS matrix. Decomposition at higher temperatures is likely due to polystyrene homopolymer (see Figure 63).

Thermal analysis information on MACOPS is not yet reported in literature but a comparison can be made to cross-linked epoxidized maleated castor oil (EMACO) synthesized by Sahin *et al.*

[36]. The onset temperature for thermal degradation of cross-linked EMACO was found to be 209 ˚C (5% mass loss) with maximum mass loss occurring after 300 ˚C [36]. Thus MACOPS has a higher onset temperature for thermal degradation than cross-linked EMACO.

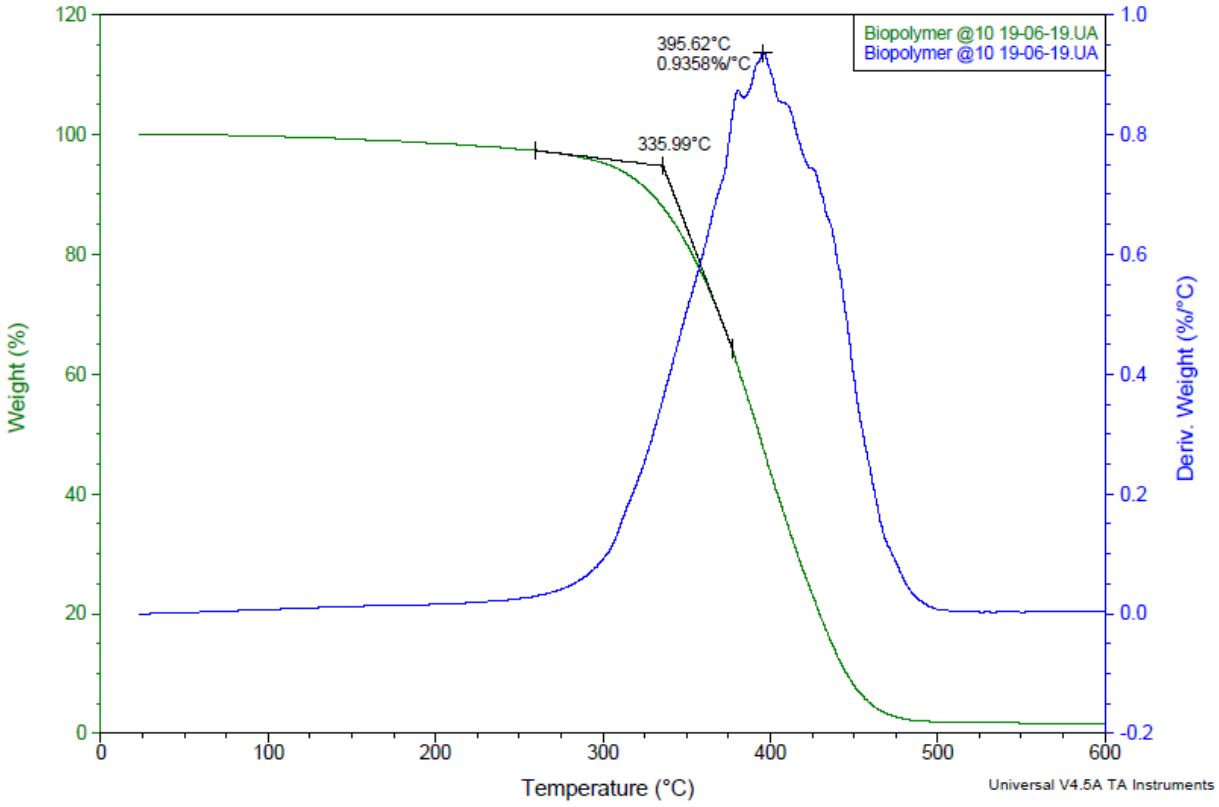

Figure 55: TG thermogram and first derivative curve of MACOPS

The thermogram for the reinforced composite (Figure 56) shows a stepwise thermal degradation. Between temperatures of 50 ˚C to 150 ˚C mass loss is observed. This is most likely due to the evaporation of moisture present in the composite [113, 114] and possibly the presence of unreacted styrene. Such moisture loss is commonly seen with natural fibres [115]. This moisture could also have contributed to the poor interaction between fibres and matrix. Note that the fibres were dried before the hand lay-up process. Moisture could have also been absorbed during the waterjet cutting process (due to storage in wet bags after cutting).

The mass loss in the temperature range of 150 ˚C to approximately 240 ˚C can be attributed to the dehydration of fibre constituents (mainly cellulose) [114]. Major mass loss of approximately 50%, can be seen in the region of 250 ˚C to 350 ˚C, with maximum loss seen at 332 ˚C. This is due to the thermal degradation of the MACOPS matrix and some hemicellulose present in the fibre reinforcement. The thermal degradation of cellulose also starts taking place in this temperature region [113, 114]. The second major mass loss (approximately 17%) in the

temperature region of 350 ˚C to 400 ˚C is assigned to cellulose degradation [114]. The temperature in this region where maximum mass loss occurs is 368˚C.

The 24% weight left over is due to the formation of ash [113].

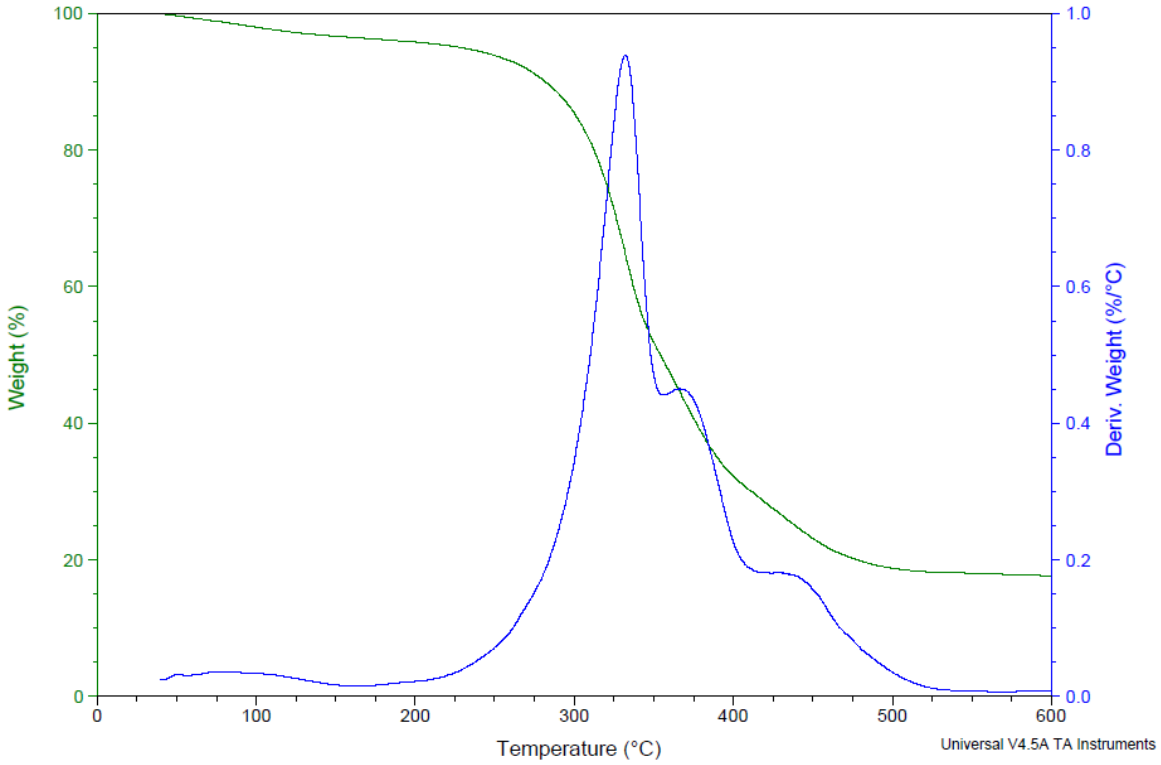

Figure 56: TG thermogram and first derivative curve of reinforced MACOPS

The onset temperature for the thermal degradation of GPPS was found to be 396 ˚C with maximum degradation taking place at 417 ˚C. The onset temperature for thermal degradation according to literature is 375 ˚C [116]. HIPS on the other hand starts to undergo thermal degradation at a temperature of 383 ˚C (5% mass loss) with maximum rate of mass loss at 441 ˚C. Extrapolated onset was 420 ºC. Literature states onset (5% mass loss) to be 380 ºC and the temperature where maximum mass loss occurs for HIPS as 440 ˚C [107]. For HIPS 5% mass loss and maximum rate of mass loss temperature are thus consistent with literature.

The comparison of the thermal degradation properties as seen in Table 17, gives valuable information on the operating temperatures of the newly synthesized polymer matrix. MACOPS has a lower maximum operating temperature than that of GPPS and HIPS.

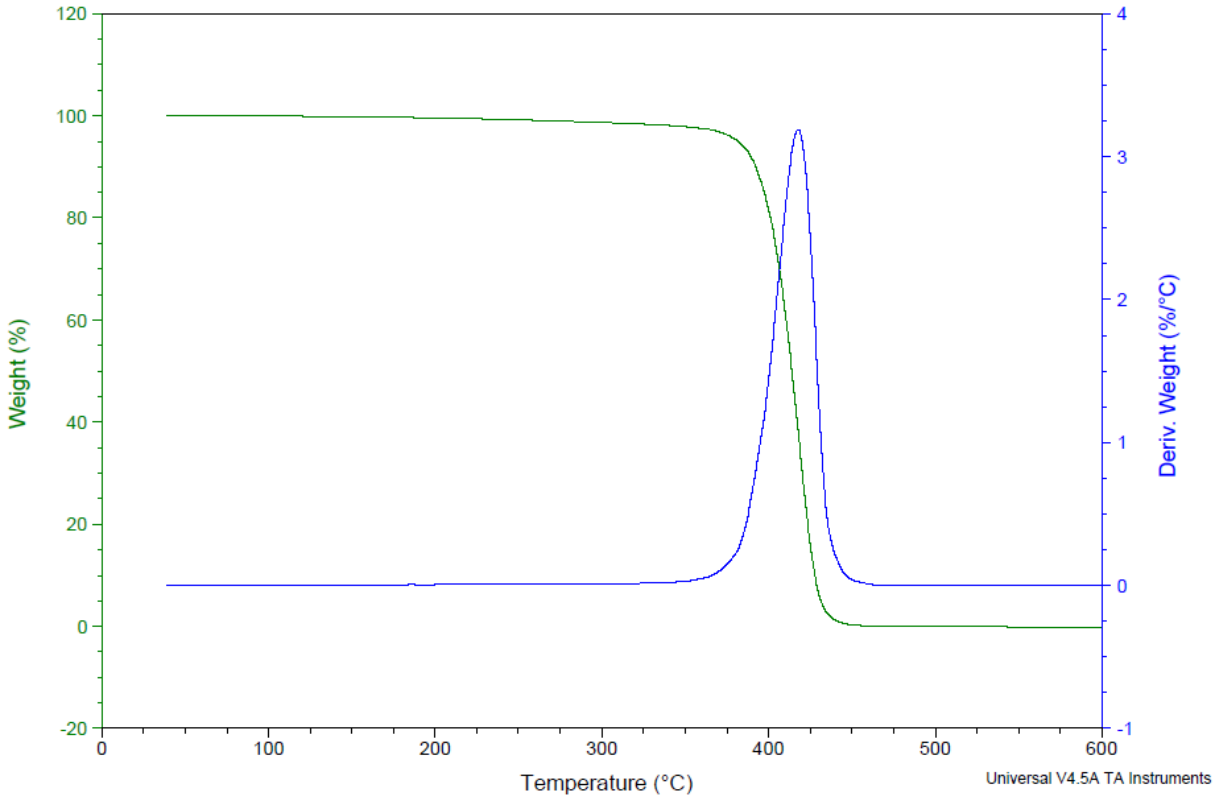

Figure 57: TG thermogram and first derivative curve for GPPS

Table 17: Comparison of thermal degradation properties of tested polymers

Polymer	Onset Temp. (˚C)	Temp. for 5% mass loss (ºC)	Max. Mass Loss Temp. (˚C)	Maximum Rate (%/˚C)
MACOPS	336	304	396	0.94
GPPS	396	382	417	3.19
HIPS	420	383	441	2.29

Onset temperatures are extrapolated from the weight% vs time curve. The 5% mass loss temperatures display a similar trend to the extrapolated onset although the HIPS degradation does include an early step (possibly the butadiene segments) which causes a greater difference with the extrapolated onset than is seen with GPPS.

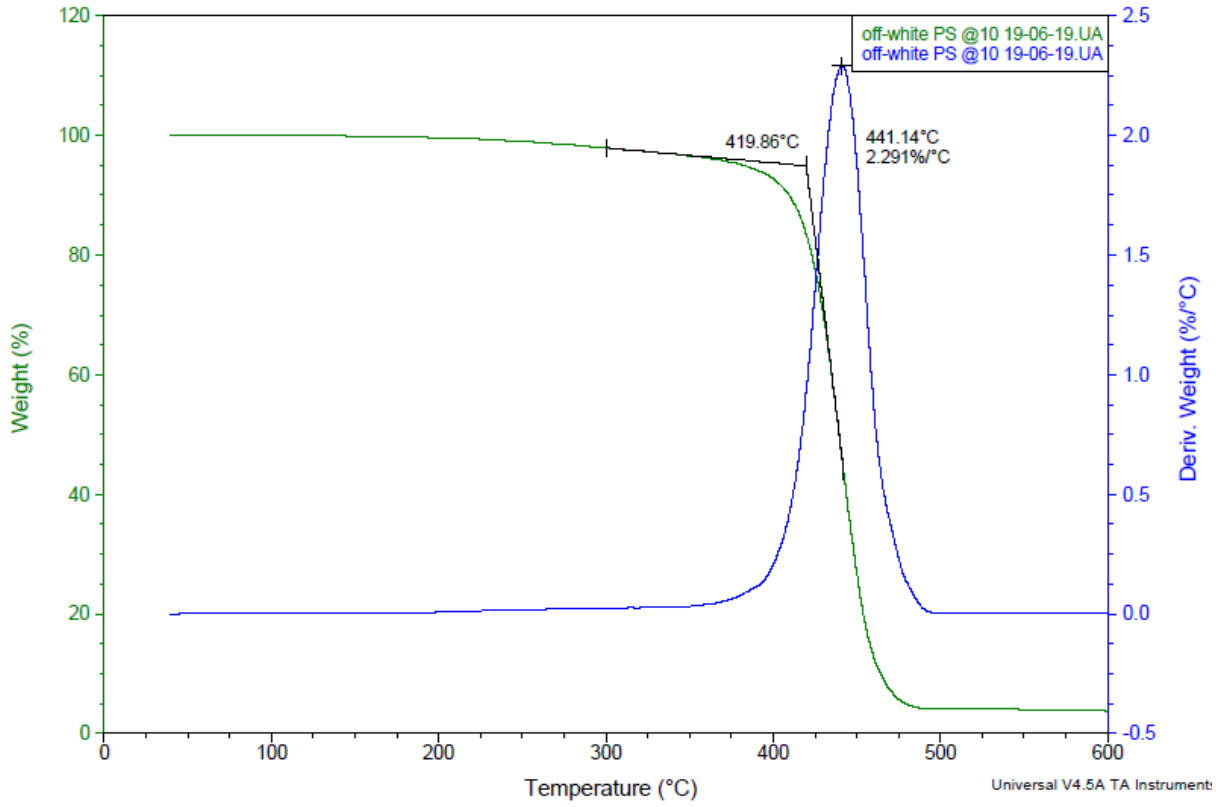

Figure 58: TG thermogram and first derivative curve for HIPS

4.2.10 Biodegradability testing

The biodegradability tests lasted for 10 weeks after which the masses of the degraded samples were measured as well as their tensile properties. All samples were cut to the same dimensions before starting the test. Mass loss data can be seen in Table 18.

Newspaper samples were used as the positive control (almost 100% degradation possible when placed in soil). Note that the degraded mass of the newspaper samples could not be determined due to almost complete disintegration of the material. The highest percentage mass loss was found for the MACOPS matrix (10.4%). The tensile stress-strain curves for the degraded samples can be found in Appendix C.

Table 18: Mass loss of tested materials after biodegradability tests

Sample	Original Mass (g)	Mass after 10 weeks (g)	Percentage mass loss
Newspaper	0.072 (±0.001)	Not Available	Not Available
MACOPS	3.024 (±0.094)	2.710 (± 0.091)	10.4%
Reinforced MACOPS	3.014 (±0.163)	2.970 (± 0.026)	1.46%

Considering the mechanical properties after the biodegradability test, as seen in Table 19, the materials showed no statistically significant loss in mechanical properties after 10 weeks.

Table 19: Comparison of mechanical properties before and after biodegradability test

Sample	Young's modulus (MPa)			UTS (MPa)		
	Original	Degraded	Percentage loss	Original	Degraded	Percentage loss
PS	2580 (± 290)	2397 (± 159)	No loss (within experimental error)	28.3 (± 6.0)	17.9 (± 0.63)	No loss (within experimental error)
MACOPS	722 (± 42)	746 (± 37)	No loss (within experimental error)	20.6 (± 0.81)	19.5 (± 0.52)	No loss (within experimental error)
Reinforced MACOPS	598 (± 65)	702 (± 16)	No loss (within experimental error)	15.2 (± 0.87)	13.5 (± 0.40)	No loss (within experimental error)

Note: The values in brackets refer to the standard deviation of the mean (S/√N)
The values for Young's modulus and UTS is slightly lower for original MACOPS and slightly higher for reinforced MACOPS compared to the values in section 4.2.2

Wang *et al.* synthesized a biodegradable foam from maleated castor oil and styrene [35]. Different styrene contents were used and it was found that an increase in styrene content delayed the mass loss and loss in mechanical properties for the samples undergoing degradation (due to the increase in crosslinking) [35]. 35 wt% styrene was used in the synthesis of MACOPS, which might explain why the degradation results were not statistically significant. It should also be noted that because Wang *et al.* were studying foams there was a significant difference in surface area at which biodegradation could initiate. Another reason might be due to the short exposure time of the samples in the compost as well as a possible lack of microorganisms in the compost (as some researchers added additional microorganisms and nutrients). Furthermore testing was performed in winter. Faster degradation might occur under warmer conditions.

4.2.11 Contact-angle measurements

Contact angle measurements are critical in the development of polymers as it supplies information on the degree of wettability of a solid (polymer) with a liquid, *e.g.,* water. Wettability can be influenced by the surface topography or the chemical nature, amongst others, of the solid [117].

Table 20: Measured contact angles of the tested materials

Sample	Contact Angle		
	Original	**Degraded**	**Percentage decrease**
MACOPS	76.5° (±0.4)	69.1° (±0.2)	9.67%
Reinforced MACOPS	88° (±1)	54.2° (±0.2)	38.4%
	Untreated	Treated	
Greige fibre	74.3˚ (±0.3)	Not measurable	

Note: the values in brackets refer to the error as stated by the ImageJ analysis program (Contact angle plugin)

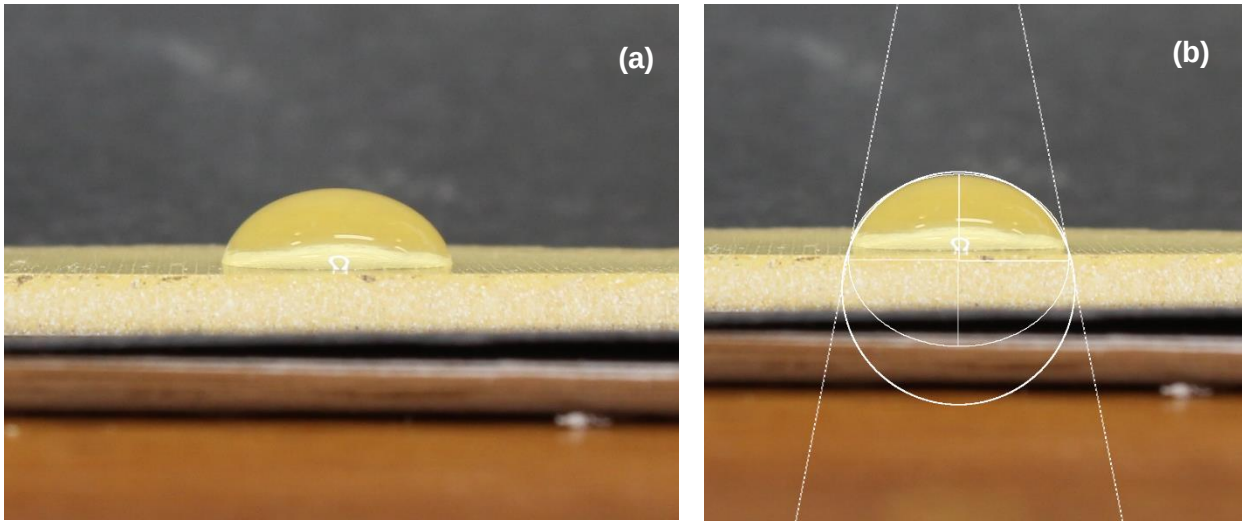

Figure 59: (a) Water droplet on MACOPS surface and (b) an example of the contact angle analysis done by ImageJ

It is known that better wetting of a material results in a lower contact angle. Non-polar groups on the surface of the polymer such as methyl groups, results in water molecules (which are polar) being “pushed away” from the material. This results in a hydrophobic material. Polymers that have polar groups on the surface such as hydroxyl or carboxyl groups, attract water molecules to the surface of the material; thus resulting in a hydrophilic material [117]. Hydrophobic materials have low surface energies and contact angles above 90° whilst hydrophilic materials have higher surface energies and contact angles below 90° [117, 118].

The degradation process seemed to increase the hydrophilicity of the materials. The contact angle pictures can be seen in Appendix D. A constant contact angle was observed for the reinforced MACOPS sample but after degradation a decrease in the contact angle was seen which kept on decreasing as time passed. For the greige fibres it was found that the contact angle decreased after the alkalization process. The contact angle for the treated greige fibre could not be measured as the water droplet almost immediately wetted the whole surface of the fibre (Figure 60). The excellent wetting of the treated fibre and the fact that some fibre might have been exposed after the degradation process of the reinforced MACOPS composite, can further explain the continuous decrease observed for the contact angle of the water droplet on the reinforced MACOPS.

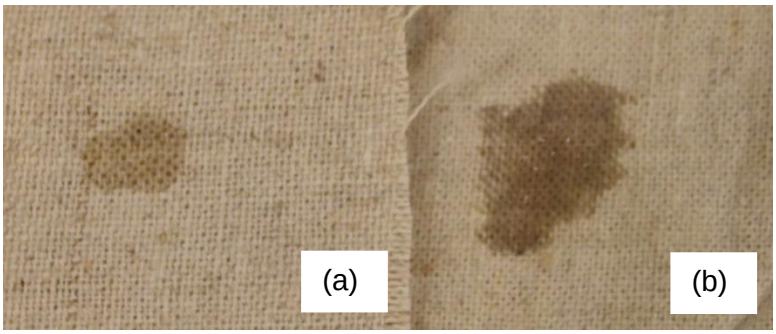

Figure 60: (a) Untreated fibre after removal of water droplet and (b) treated fibre after water droplet wetted surface of fibre

It is suggested that some degradation occurred in the reinforced sample exposing greige fibres which then absorbed water, lowering the contact angle.

The biodegradability results were thus mixed. Contact angle and mass loss measurements suggested some degradation but no decrease in mechanical properties was observed. This may be because, on the time scale of the experiment, styrene crosslinks were still intact and the MACOPS fraction would require further hydrolysis before breakdown occurred.

4.3 Optical characterization

4.3.1 Transmission Electron Microscopy

Information on phase separation and the distribution of phases through the sample can be obtained through transmission electron microscopy.

In Figure 61 two phases are clearly seen in the HIPS sample. The salami-like structure of the polybutadiene phase (dark grey) is distributed throughout the light grey polystyrene phase. Phase segregation is thus seen in this graft co-polymer.

The TEM micrograph for MACOPS (Figure 62) shows no phase segregation. No localised staining of residual fatty acid ester double bonds was observed. This result supports the idea that MACOPS is a co-polymer with little to no phase separation or that any polystyrene formed is present as an IPN with the MACOPS polymer and homopolymerized polystyrene not phase segregated. When the sample was stained with RuO_4, the sample section turned a grey colour. Once again no preferential staining was observed. RuO_4-stained are not included.

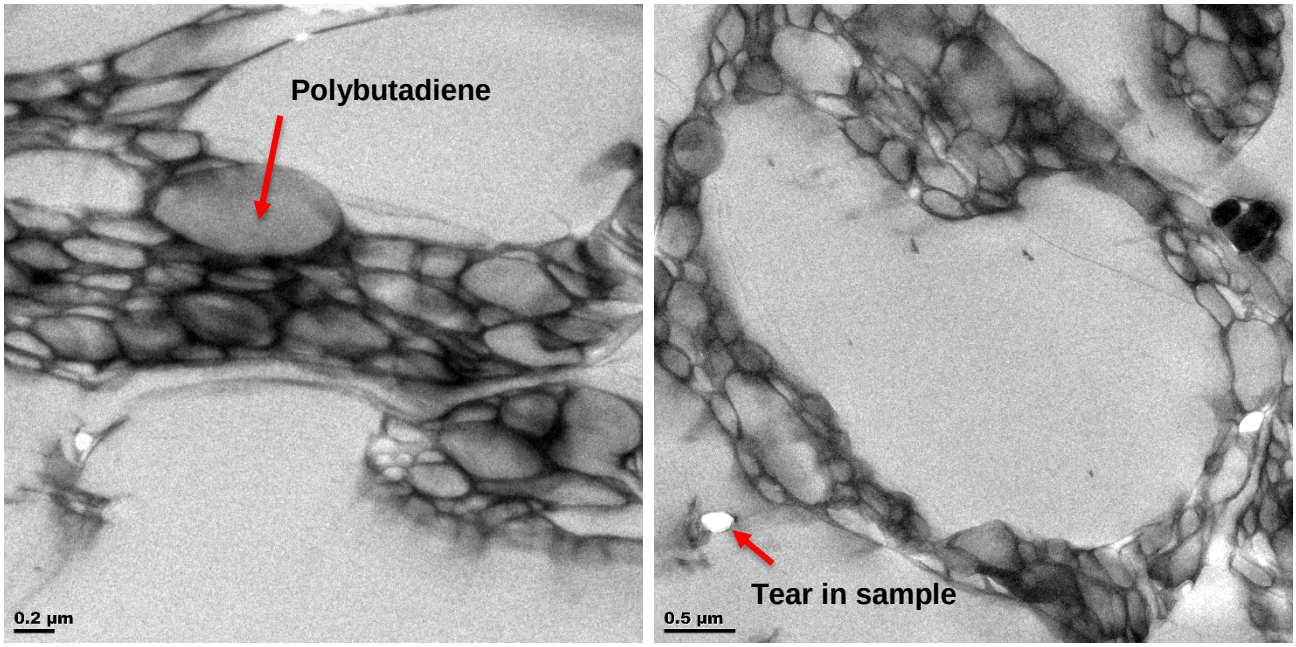

Figure 61: TEM micrograph of HIPS (Staining agent: OsO_4)

4.3.2 Raman analysis

In Figure 64, some clear resemblances and differences can be seen between the spectra. The most significant being the peak in area A which is only present in the spectrum of MACOPS and area B where noticeable changes in the peak intensity can be observed.

The research by Mamat *et al.*, produced a FTIR spectrum for maleic acid-castor oil monoester (MACOME) and a copolymer of styrene and MACOME [119]. For both Raman and IR (infrared spectroscopy), the wavenumbers for characteristic peaks are comparable but a difference in the intensities are clearly noticeable. Therefore when the experimental data for MACOPS and MACO were compared to the literature, area A and area B (as seen in Figure 63) could be recognized in both experimental and literature data.

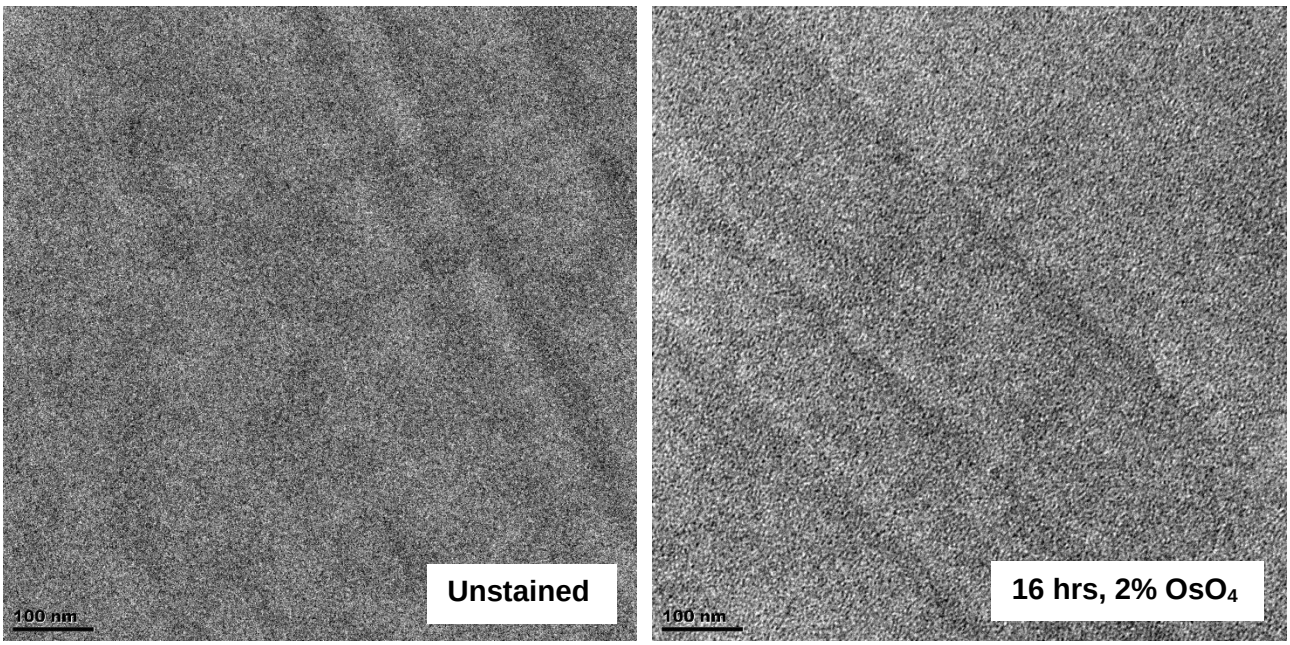

Figure 62: TEM micrographs of MACOPS (Staining agent: OsO_4)

Considering the experimental data, the set of small peaks in area A at 476 cm^{-1} and 619 cm^{-1} for the MACOPS sample (Figure 64 and Figure 65) and as set of small peaks in the PS sample at approximately 483 cm^{-1} and 627 cm^{-1} (Figure 64 and Figure 66)) may represent that of a mono-substituted benzene ring [120]. This can be assigned to the presence of styrene-derived units. At 1661 cm^{-1} the absorption band of the carbonyl group can be seen for MACOPS as well as methyl and methylene groups at 2856 and 2924 cm^{-1} (area B). A decrease in these methyl and methylene peaks were seen as the reactions progressed, with the highest intensity seen for castor oil (Figure 67). Another area of interest is area C where the visible peak is representative of alkene and aromatic double bonds.

Figure 65 to Figure 68 are expanded spectra of those shown in Figure 64. Raman spectroscopy was used as an effective tool to confirm that maleation of the castor oil took place during the maleation reaction. The presence of maleic anhydride in the MACO sample would suggest an incomplete reaction. Maleic anhydride is known to have absorption bands at 1850 and 1790cm^{-1}. Considering the experimental data for MACO (Figure 68), no significant absorption bands can be seen at these wavenumbers; thus the maleation reaction can be considered completed. An increase in the carbonyl group absorption band at 1739.4 cm^{-1} (comparing castor oil (Figure 67) to MACO (Figure 68)) confirms the addition of the maleate groups.

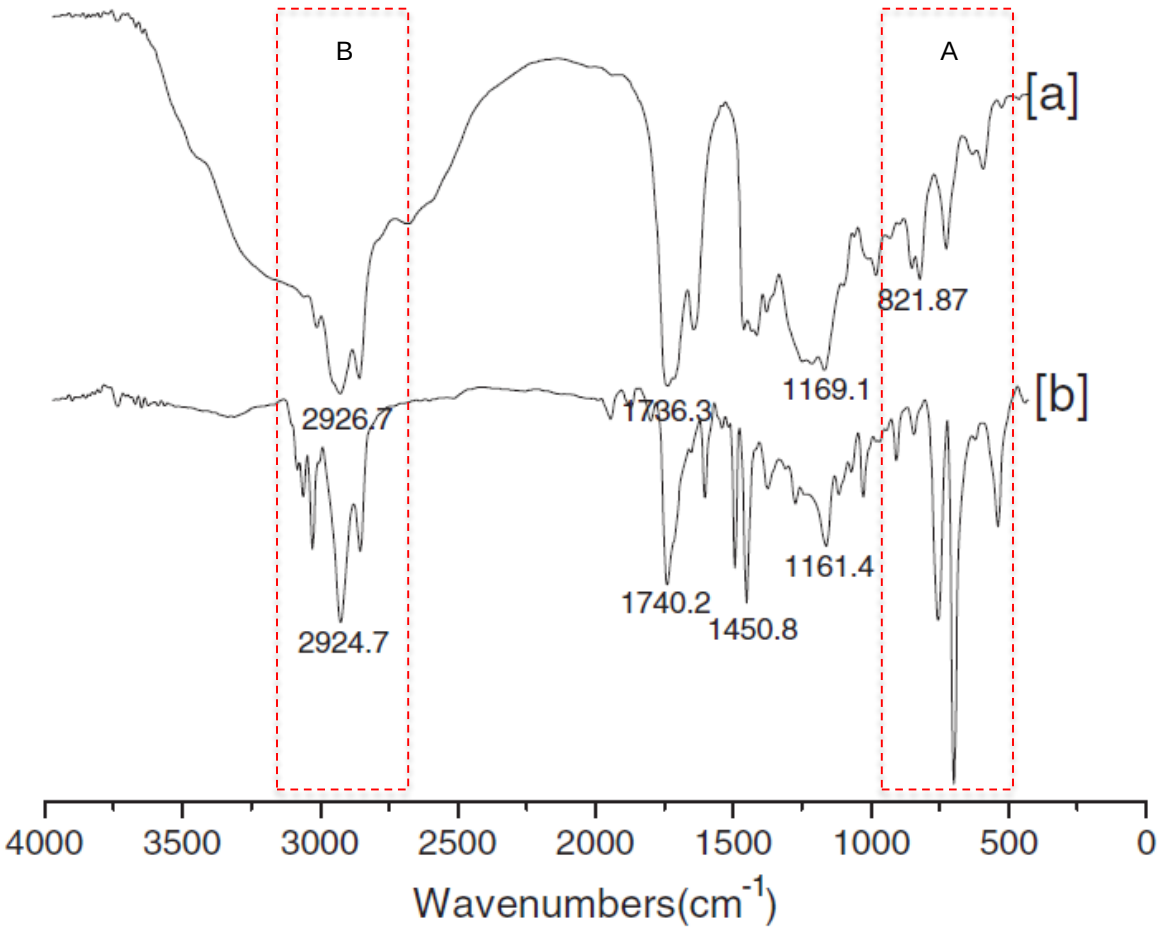

Figure 63: FTIR spectrum of (a) MACOME and (b) MACOME and styrene co-polymer [119]

A Raman map was used to study the distribution of polystyrene through the MACOPS sample. Polystyrene is shown in green on the map. In Figure 70 (a) the light green regions represent areas with high intensity signals for PS, with the darker regions being less intense. Figure 70 (b) and Figure 69 (b) shows the microscope image of the surface being analyzed. For HIPS the lighter green regions also represent areas of high intensity PS signals whilst the darker black areas correspond to the polybutadiene present in the sample (Figure 69 (a)). The Raman map for HIPS corresponds to the TEM micrograph found in section 4.3.1 (Figure 61) also showing clusters of polybutadiene.

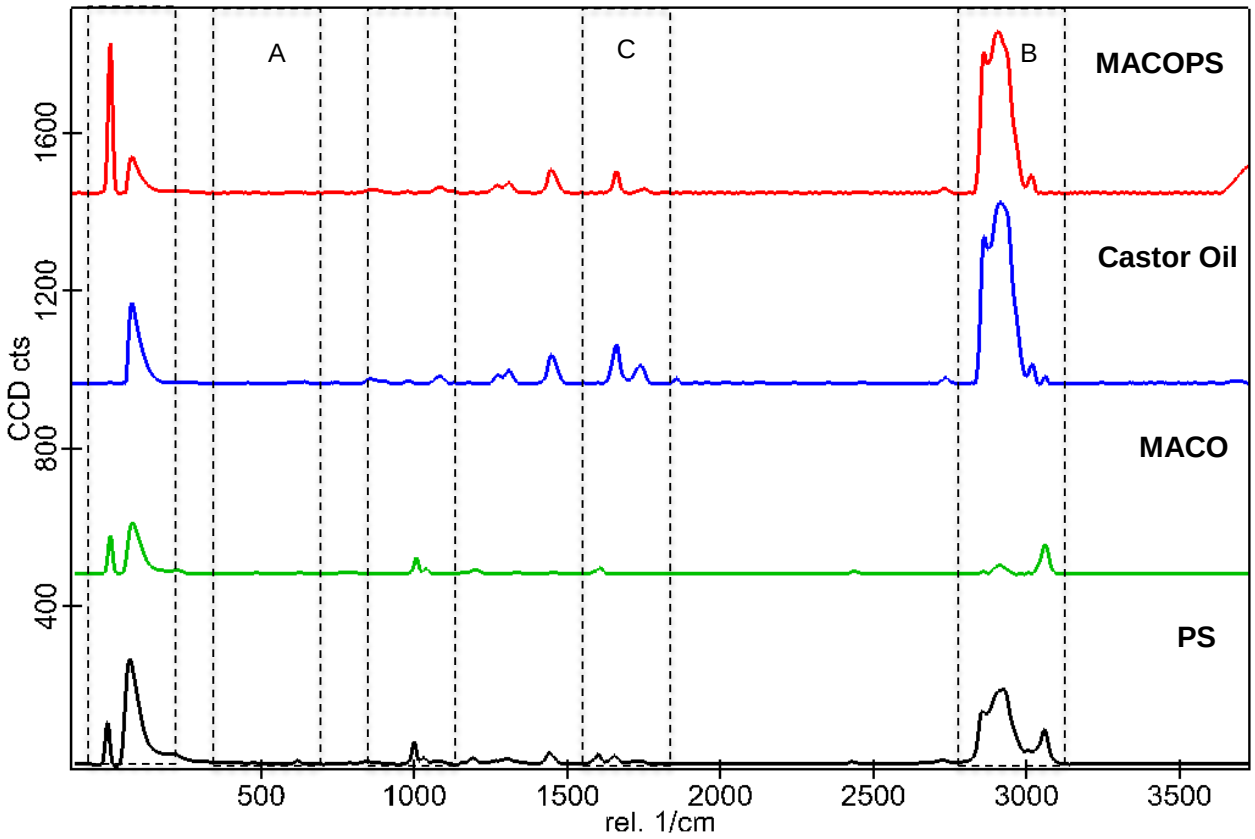

Figure 64: Overlayed Raman spectra of MACOPS and its components

The lines present on the map of the MACOPS sample correspond to the scratches visible on the surface image and do not suggest the formation of linear clusters of PS. Both maps confirm the mostly uniform distribution of PS throughout MACOPS and HIPS. HIPS is seen to have clusters of polybutadiene present in the sample whereas MACOPS shows no phase segregation. Raymond *et al.* conducted a SEM study on an epoxy/castor oil graft interpenetrating polymer network which resulted in a uniform morphology throughout the IPN [31]; therefore the uniform morphology of the MACOPS as seen in Figure 70 (a) might point to the formation of an IPN.

4.3.3 SEM analysis of the fracture surface of reinforced MACOPS

Analyzing the fracture surface of a broken reinforced sample can give valuable information as to the nature of the fibre being used, nature of the matrix (ductile or brittle) and matrix-fibre interactions. Due to the mechanical properties of the reinforced composite being significantly less than expected, SEM analysis is critical in determining the cause.

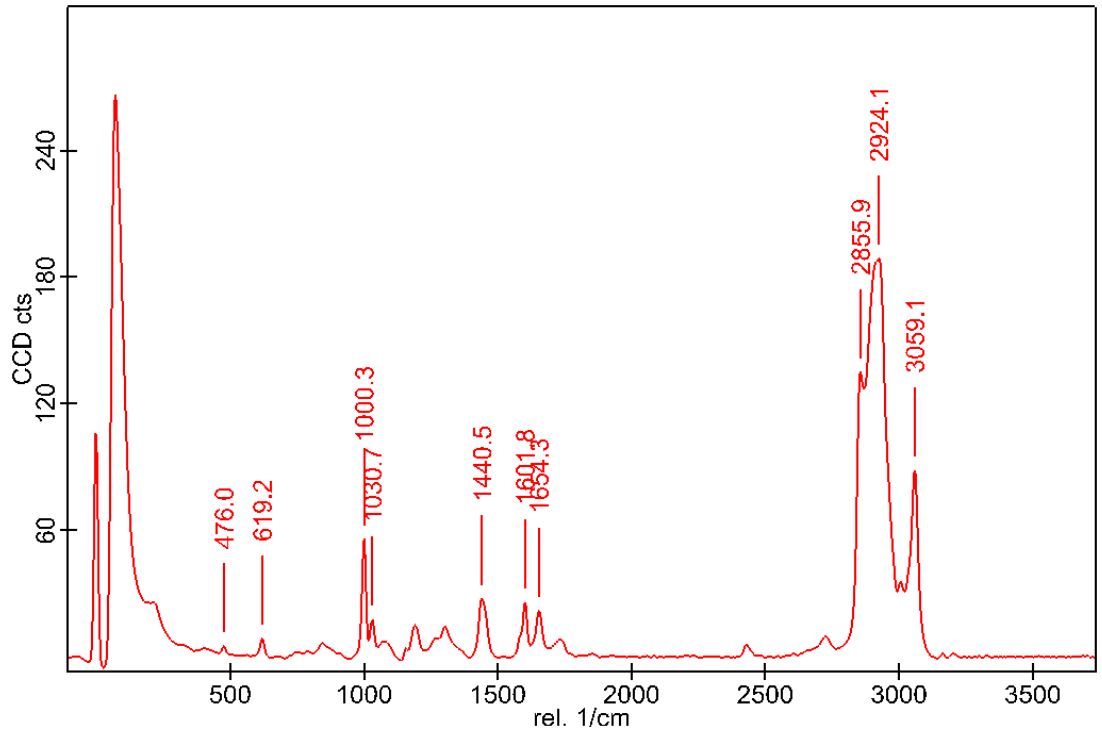

Figure 65: Raman spectra of MACOPS

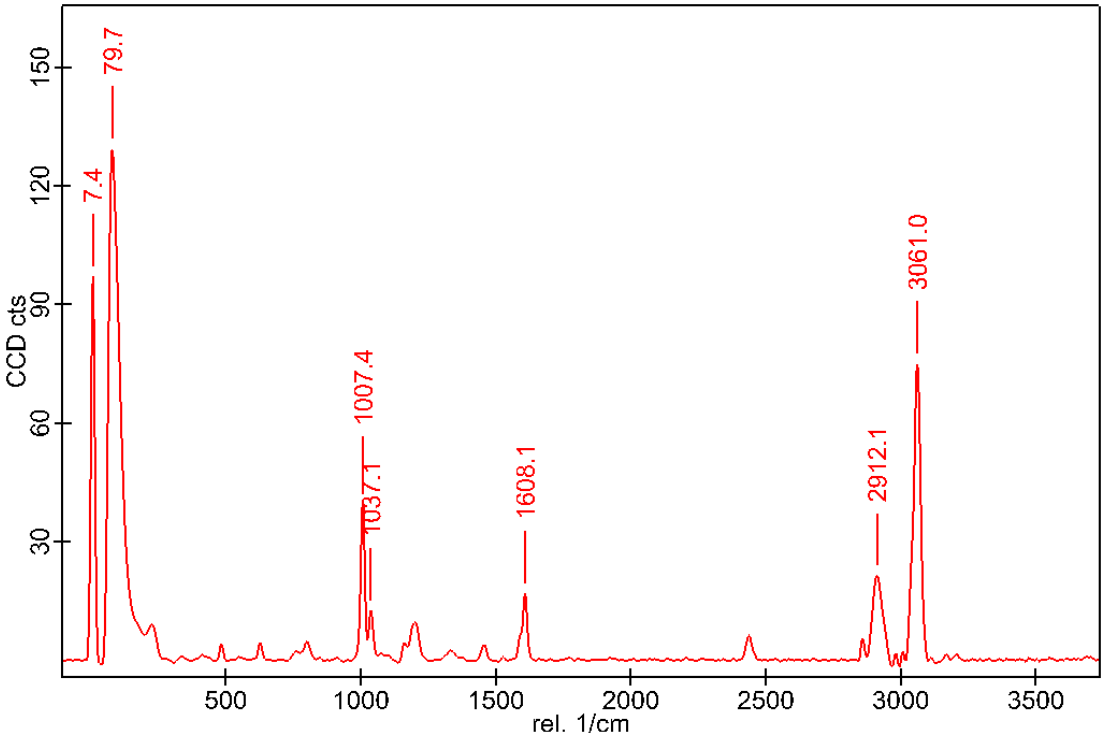

Figure 66: Raman spectra of GPPS

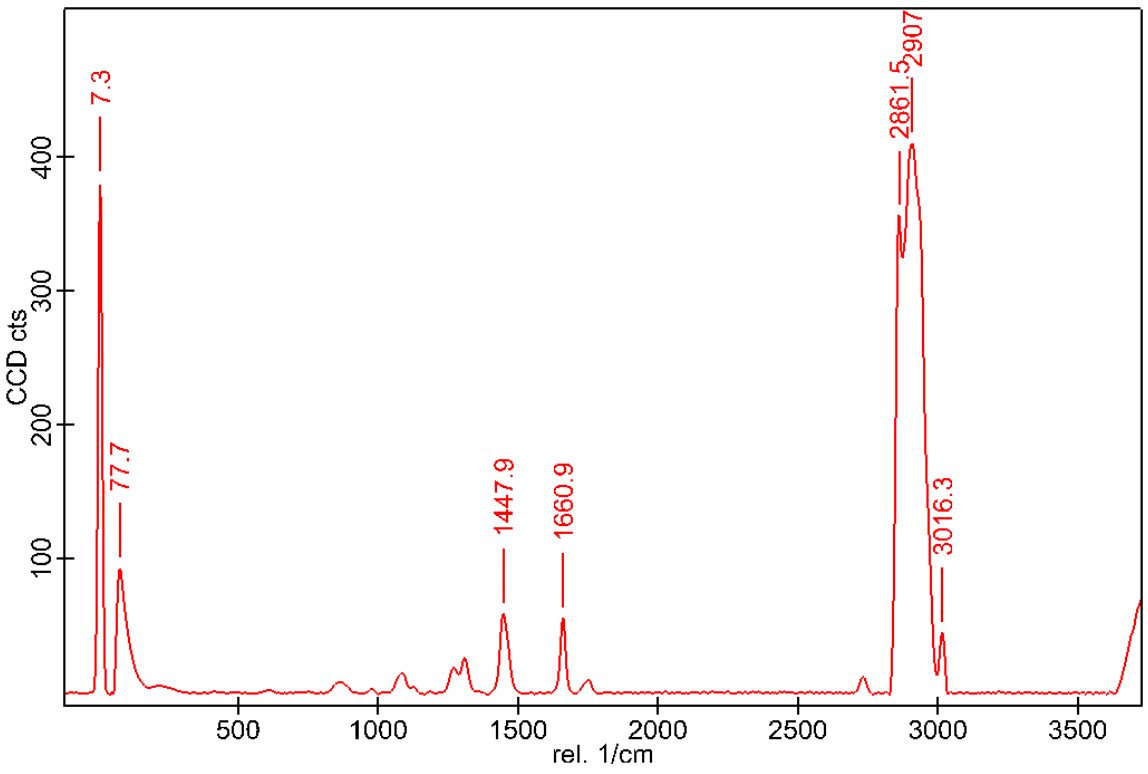

Figure 67: Raman spectrum of castor oil

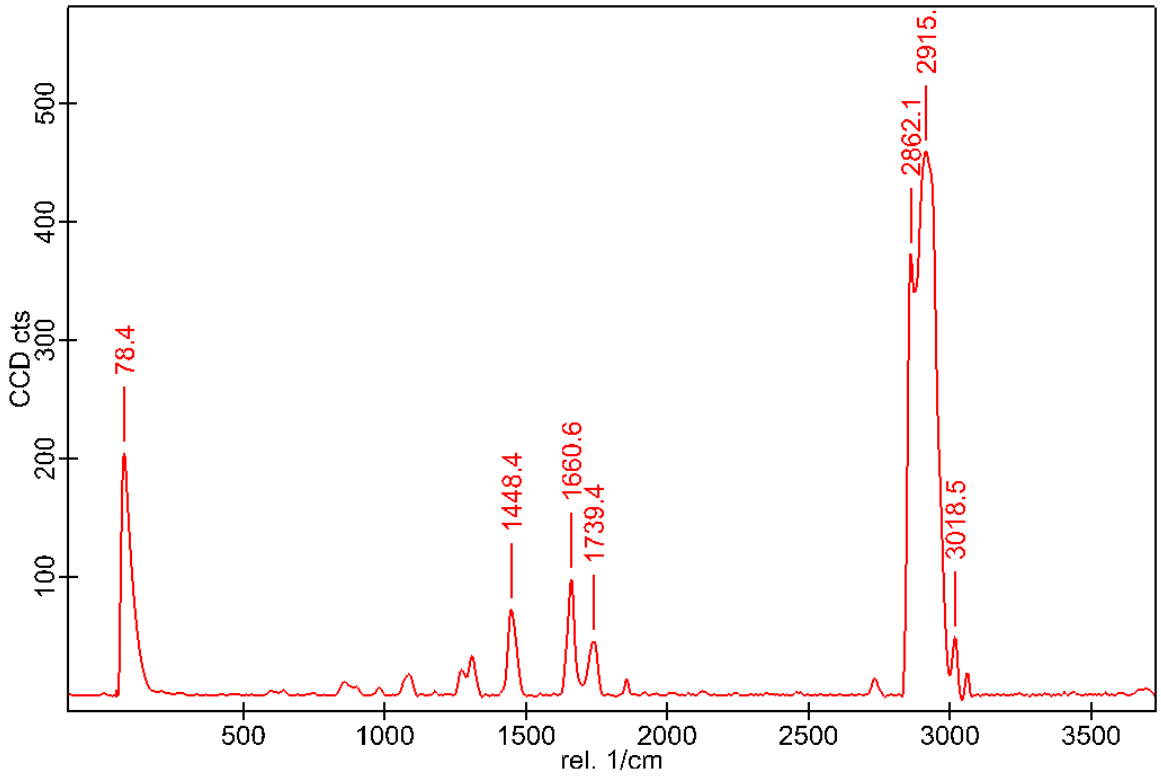

Figure 68: Raman spectrum of maleated castor oil

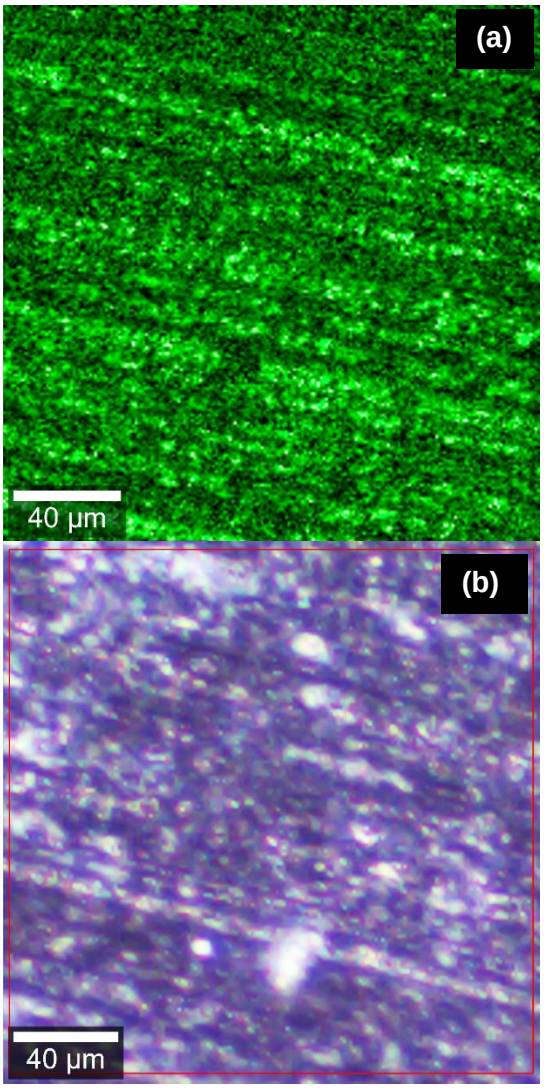

Figure 70: Raman map of MACOPS

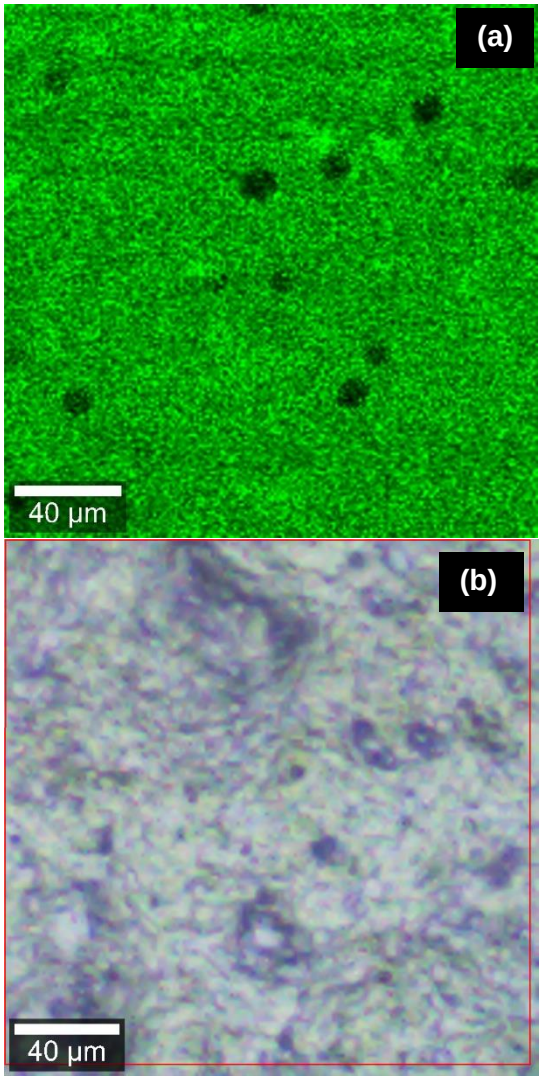

Figure 69: Raman map of HIPS

Figure 71 shows a SEM image of two tensile fracture surfaces. Some critical flaws can be detected in the images. Area A shows what can be seen as an imprint of the fibres left on the matrix. This points to weak adhesion between the matrix and the fibre. Area B shows a region where no matrix is present causing a void in the composite. Voids can be caused by insufficient wetting of the fibres. At C debonding between the fibre and matrix can be observed. This causes a crack to form along the fibre with a length of approximately 300µm. Once again the presence of debonding can be ascribed to weak fibre-matrix interactions. Area D shows ductile matrix cracking.

Figure 72 shows the presence of possible fibre pull-out. No matrix is attached to the base of the fibres Exposed fibres are seen sticking out of the matrix and in the matrix the imprint is visible where fibres were present before fracture.

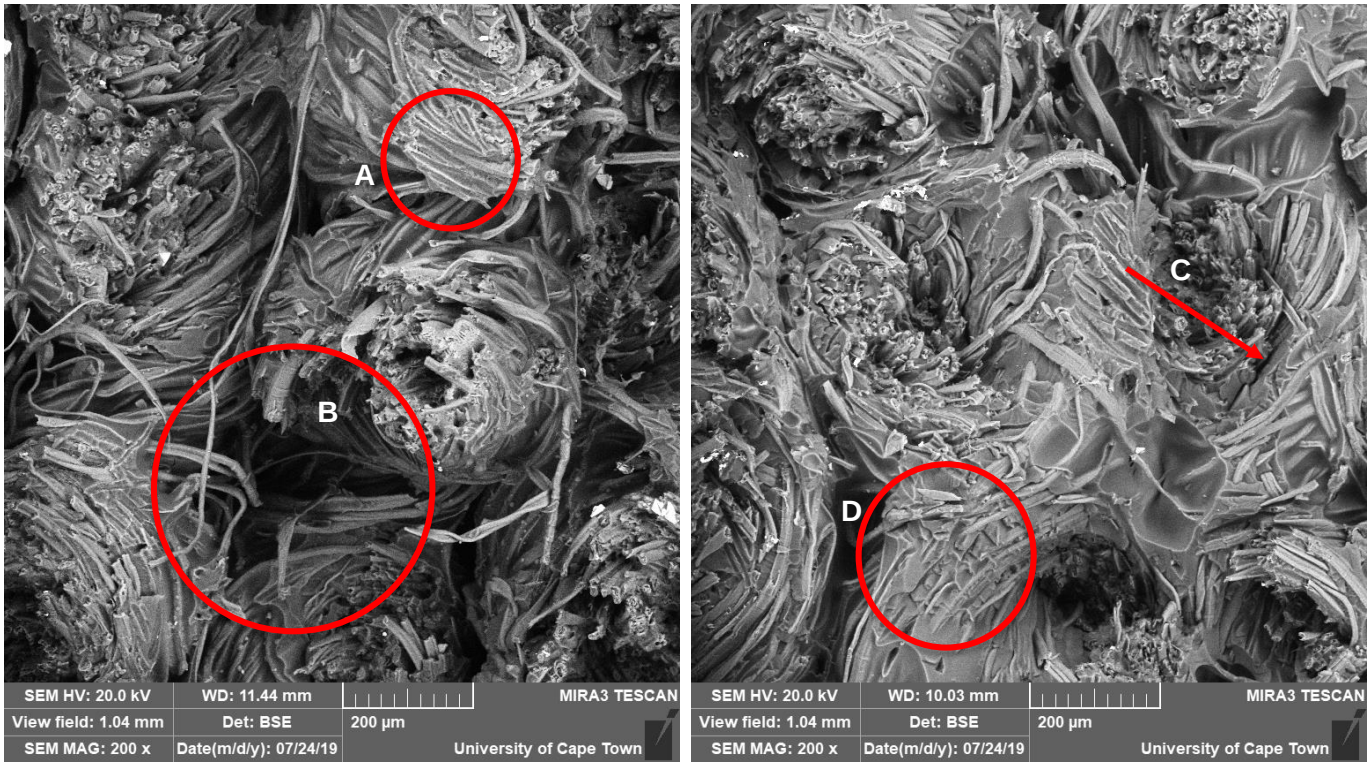

Figure 71: SEM image of the tensile fracture surface for reinforced MACOPS

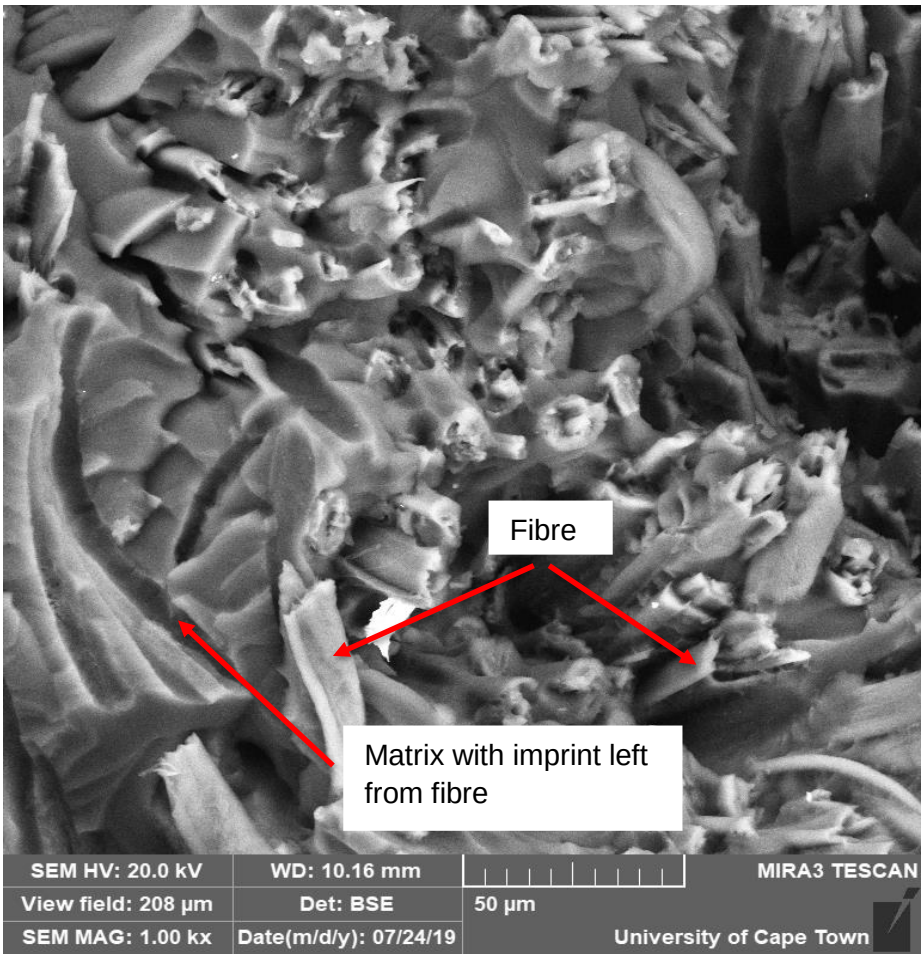

Figure 72: View of the reinforced composite fracture surface at higher magnification

Chapter 5: Conclusions

It has been demonstrated that a polymer matrix can be successfully synthesized using maleated castor oil and styrene. Research done in this paper extends the literature on polymers made from renewable resources by measuring a suite of mechanical properties not measured before. It has been demonstrated that a polymer matrix can be successfully synthesized using maleated castor oil and styrene. Valuable information has been obtained during the course of the research regarding mechanical properties. The synthesis of the matrix is a “one pot” synthesis and relatively energy efficient.

Curing of the MACOPS resin resulted in a flexible but tough matrix. The impact, flexural and tensile properties were similar to those of HIPS. The morphology of the MACOPS matrix was found to be either a co-polymer or an interpenetrating polymer network and revealed the presence of crosslinks between polymer chains.

The high impact strength of the MACOPS matrix and composite (almost 1.5 times that of GPPS) correlate with the toughness results which were 4 times that of GPPS.

The addition of MACO to styrene resulted in a 70% decrease in modulus and a 50% decrease in tensile strength of the matrix when compared to GPPS. The results obtained for flexural strength are evidence for MACOPS being flexible. The addition of MACO to styrene resulted in a matrix with increased flexibility compared to that of GPPS as the flexural strength of MACOPS was 70% less. MACOPS showed the presence of shape memory after flexural tests which confirmed the presence of crosslinking.

For the flexural, tensile and impact properties, the reinforcement with greige fibres produced mixed results. In the case of the reinforced matrix under flexion, the greige fibre reinforcement increased the flexural strength but showed large amounts of delamination. Under tensile loads the efficiency of the fibres as reinforcement was low and thus the fibres acted primarily as a filler. Possible causes for the greige fibres failing as a reinforcement were identified, namely the volume fraction of the fibres was too high and the homopolymerized polystyrene network might have caused chemical incompatibility between the fibres and the matrix.

Degradation studies produced mixed results with contact angle measurements and mass loss indicating that some degradation took place although no decrease in the mechanical properties were seen. Although the results were mixed, the matrix is still made from renewable resources resulting in a green polymer.

Differential scanning calorimetry revealed two glass transition temperatures for MACOPS. The Tg peak corresponding to polystyrene was small. However a large glass transition temperature peak was seen for the co-polymer. This resulted in the conclusion that either a co-polymer was formed or an interpenetrating polymer network was formed. The low Tg (55˚C) corresponds with

the flexibility of the matrix at room temperature. Thermal gravimetric analysis revealed a thermal degradation onset temperature for MACOPS lower than those of the commercial polymers used in this study.

Raman spectroscopy was effective in determining if the castor oil was maleated successfully. Similarities between the peaks in the MACOPS spectrum and PS spectrum were seen.

Through scanning electron microscopy critical flaws were observed in the reinforced MACOPS tensile fracture surface. These flaws included voids, debonding and brittle matrix cracking. The visible flaws account for the weak mechanical properties of the reinforced MACOPS composite. Fibre pull out was also noted. The flaws present seemed to be largely due to processing issues of the composite.

Transmission electron microscopy and Raman mapping showed visible phase segregation for HIPS as it is a graft co-polymer. The TEM micrograph and Raman map for MACOPS showed no phase segregation and therefore confirms the conclusion that MACOPS is either a co-polymer or an IPN.

The successful characterization of a biopolymer made from renewable materials, which can be used as an alternative to traditional plastics such as HIPS, was accomplished in this study. The MACOPS biopolymer may possibly be used as an alternative in the future.

Chapter 6: Recommendations and future work

This project has formed a good basis for the research on a matrix formed using maleated castor oil. Numerous opportunities for future research can stem from this project.

Firstly, the mixing ratios of the reactants can be changed to determine the effect of MACO weight percent on the properties of the matrix. The weight percent of MACO and styrene can be varied from 10 wt% to 90 wt%. By conducting this study on various mixing ratios, the composition for optimal mechanical properties can be determined. Various mixing ratios can be used to tailor the properties depending on the application. A variety of initiators can be investigated which can alter the reaction time. At present the reaction is a time-consuming process which will not be suited for industrial use and therefore exploring different options can make the process more viable. Examples of suitable initiators are BPO and dicumyl peroxide. Together with such a study, comparison with an unsaturated polyester or polyurethane should be included as some of these co-polymers would be expected to have properties similar to these additional reference polymers.

The composite can be manufactured using different methods. For example, the effects that vacuum bagging and the vacuum infusion process have on the properties of the composite can be explored. By changing the manufacturing process to an enclosed process, voids and delamination may be minimized due to the pressure formed by the vacuum. Furthermore, the type of fibre used and the amount of fibre used for reinforcement can be altered. Pure hemp fibre, sisal or jute fibres (with a looser weave than the greige fibres used in this study) can be used as an alternative reinforcement. The fibre volume fraction should cover the range from 0.2 to 0.4.

As mentioned in the aim of this project, a completely biodegradable matrix is desired; thus more research can be done to completely replace styrene with a structurally similar environmentally friendly alternative. This may produce more satisfactory results after conducting the biodegradability tests. Research could be done on ways to produce an odourless matrix, which is preferred for certain applications. It would also be of value to conduct gas chromatography on the soil after the biodegradability test to examine any substances that were released into the soil. The biodegradability of the matrix and composite can be investigated in the presence of various microorganisms, UV-rays and oxidative environments. These experiments could provide information on the degradation processes of maleated castor oil modified polymers.

The determination of the molecular structure of the matrix by solid state NMR-spectroscopy will provide valuable information and explain some of the mechanical properties observed. NMR-spectroscopy can provide, through analysis, information on the number of double bonds present (if present) and of the final molecular structure of the matrix. The final structure will enable the explanation of mechanical properties on a molecular level (e.g., chain entanglement and interactions between the functional groups present).

To improve the matrix-fibre interactions, the effect of silane coupling agents can be investigated with regards to the improvement of mechanical properties of the composite. Organosilane coupling agents (adhesion promoters) are regularly used and will improve the fibre matrix bonding by acting as an intermediate between the matrix and the fibre [121].

References

[1] N. Winterton, Chemistry for Sustainable Technologies: A Foundation, Cambridge, UK: RSC Publishing, 2011.

[2] F. S. Guner, Y. Yagci and A. T. Erciyes, "Polymers from triglyceride oils," *Progress in Polymer Science,* vol. 31, pp. 633-670, 2006.

[3] M. Mosiewicki and M. Aranguren, "A short review on novel biocomposites based on plant oil precursors," *European Polymer Journal,* vol. 49, pp. 1243-1256, 2013.

[4] C. Zhang, T. Garrison, S. Madbouly and M. Kessler, "Recent advances in vegetable oil-based polymers and their composites," *Progress in Polymer Science,* vol. 71, pp. 91-143, 2017.

[5] A. Mohanty, M. Misra and L. Drzal, "Sustainable bio-composites from renewable resources: Opportunities and challenges in the green materials world," *Journal of Polymers and the Environment,* vol. 10, no. 112, 2002.

[6] E. Mubofu, "Castor oil as a potential renewable resource for the production of functional materials," *Sustainable Chemical Processes,* vol. 4, no. 11, 2016.

[7] B. Imre and B. Pukánszky, "Compatibilization in bio-based and biodegradable polymer blends," *European Polymer Journal,* vol. 49, pp. 1215-1233, 2013.

[8] S. Ochi, "Development of high strength biodegradable composites using Manila hemp fiber and starch-based biodegradable resin," *Composites: Part A: Applied science and manufacturing,* vol. 37, 2006.

[9] A. Campanella, J. La Scala and R. Wool, "Fatty acid-based comonomers as styrene replacements in soybean and castor oil-based thermosetting polymers," *Journal of Applied Polymer Science,* vol. 119, pp. 1000-1010, 2010.

[10] H. Mutlu and M. Meier, "Castor oil as a renewable resource for the chemical industry," *European Journal of Lipid Science and Technology,* vol. 112, pp. 10-30, 2010.

[11] O. Akaranta and A. Anusiem, "A bioresource solvent for extraction of castor oil," *Industrial Crops and Products,* vol. 5, pp. 273-277, 1996.

[12] V. Patel, G. Dumancas, L. Viswanath, R. Maples and B. Subong, "Castor oil: properties, uses, and optimization of processing parameters in commercial production," *Lipid insights,* vol. 9, pp. 1-12, 2016.

[13] G. Totaro, L. Cruciani, M. Vannini, G. Mazzola, D. Gioia, A. Celli and L. Sisti, "Synthesis of castor oil-derived polyesters with antimicrobial activity," *European Polymer Journal,* vol. 56, pp. 174-184, 2014.

[14] E. Mistri, S. Routh, D. Ray, S. Sahoo and M. Misra, "Green composites from maleated castor oil and jute fibres," *Industrial crops and products,* vol. 34, pp. 900-906, 2011.

[15] P. Sathiskumar and G. Madras, "Synthesis, characterization, degradation of biodegradable castor oil based polyesters," *Polymer Degradation and Stability,* vol. 96, pp. 1695-1704, 2011.

[16] M. De Luca, M. Martinelli and C. Barbieri, "Hybrid films synthesized from epoxidised castor oil, y-glycidoxypropyltrimethoxysilane and tetraethoxysilane," *Progress in Organic Coatings,* vol. 65, pp. 375-380, 2009.

[17] J. La Scala and R. P. Wool, "Property analysis of triglyceride-based thermosets," *Polymer,* vol. 46, pp. 61-69, 2005.

[18] E. Can, R. P. Wool and S. Kusefoglu, "Soybean- and castor-oil-based thermosetting polymers: mechanical properties," *J Applied Polymers Science,* vol. 102, pp. 1497-1504, 2006.

[19] M. Desroches, M. Escouvois, R. Auvergne, S. Caillol and B. Boutevin, "From vegetable oils to polyurethanes: synthetic routes to polyols and main vegetable products," *Polymer Reviews,* vol. 52, pp. 38-79, 2012.

[20] A. Dotan, "Chapter 15. Biobased Thermosets," in *Handbook of Thermoset Plastics*, H. Dodiuk and S. H. Goodman, Eds., Norwich, NY, William Andrew Publishing, 2014, pp. 579-622.

[21] J. Cowie and V. Arrighi, Polymers: Chemistry and Physics of Modern Materials, Boca Raton, FL: CRC Press, 2008.

[22] L. Ruiz, A. Aghmiz, A. Masdeu-Bulto, G. Lligadas, J. Ronda, M. Galia and V. Cadiz, "Upgrading castor oil: From heptanal to non-isocyanate poly(amide-hydroxyurethane)s," *Polymer,* vol. 124, pp. 226-234, 2017.

[23] P. Nayak, "Natural oil-based polymers: Opportunities and challenges," *Journal of Macromolecular Science Part C,* vol. 40, no. 1, pp. 1-21, 2000.

[24] M. Robertson, J. Paxton and M. Hillmyer, "Tough blends of polylactide and castor oil," *ACS Applied Materials and Interfaces,* vol. 3, pp. 3402-3410, 2011.

[25] G. Çayli, D. Gürbüz and A. Çinarli, "Characterization and polymerization of epoxidized methacrylated castor oil," *European Journal of Lipid Science and Technology,* 2018.

[26] C. Kim, T. Traylor and C. Perrin, "MCPBA epoxidation of alkenes: Reinvestigation of correlation between rate and ionization potential," *Journal of the American Chemical Society,* vol. 120, no. 37, pp. 9513-9516, 1998.

[27] N. Parada Hernandez, A. Bonon, J. Bahù, M. Barbosa, M. Wolf Maciel and R. Filho, "Epoxy monomers obtained from castor oil using a toxicity-free catalytic system," *Journal of Molecular Catalysis A: Chemical,* vol. 426, pp. 550-556, 2017.

[28] V. Sharma and P. Kundu, "Condensation polymers from natural oils," *Progress in Polymer Science,* vol. 33, pp. 1199-1215, 2008.

[29] B. Suthar, M. Dave and K. Jadav, "Sequential-interpenetrating polymer networks from castor oil-based polyesters," *Journal of Applied Polymer Science,* vol. 50, pp. 2143-2147, 1993.

[30] L. Sperling and J. Manson, "Interpenetrating polymer networks from triglyceride oils containing special functional groups: A brief review," *Journal of the American Oil Chemists' Society,* vol. 60, no. 11, 1983.

[31] M.-P. Raymond and V. Bui, "Epoxy/castor oil graft interpenetrating polymer networks," *Journal of Applied Polymer Science,* vol. 70, no. 9, pp. 1649-1659, 1998.

[32] D. Maia, E. Filho, A. Barros Jr. and F. Fernandes, "Kinetics of the production of castor oil maleate through the autocatalyzed thermal reaction and the free radical reaction," *International Journal of Chemical Kinetics,* pp. 112-121, 2017.

[33] D. Echeverri, W. Perez and L. Rios, "Synthesis of maleated-castor oil glycerides from biodiesel-derived crude glycerol," *Industrial Crops and Products,* vol. 49, pp. 299-303, 2013.

[34] M. Saied, S. Mansour, A. Ward, I. Rahim, H. Zayed, A. Saad and K. Abdel Nour, "Characterization of maleated vegetable oils for insulation purposes and agricultural applications," *Polimery,* vol. 59, no. 10, 2014.

[35] H. Wang, M. Rong, M. Zhang, J. Hu, H. Chen and T. Czigány, "Biodegradable foam plastics based on castor oil," *Biomacromolecules,* vol. 9, pp. 615-623, 2008.

[36] Y. Sahin, G. Çayli, J. Çavusoglu, E. Tekay and S. Sen, "Cross-linkable epoxidized maleinated castor oil: a renewable resin alternative to unsaturated polyesters," *International Journal of Polymer Science,* vol. 2016, pp. 1-7, 2016.

[37] D. Echeverri, F. Jaramillo and L. Rios, "Curing copolymerization kinetics of styrene with maleated castor oil glycerides obtained from biodiesel-derived crude glycerol," *Journal of Applied Polymer Science,* vol. 132, 2015.

[38] H. Wang, C. Zhang, M. Rong, M. Zhang and T. Czigany, "Interfacial effects in short sisal fiber/maleated castor oil foam composites," *Composite Interfaces,* vol. 15, no. 2-3, pp. 95-110, 2008.

[39] D. Ray, S. Ghorui, N. Bandyopadhyay, S. Sengupta and T. Kar, "New materials from maleated castor oil/epoxy resin blend reinforced with fly ash," *Industrial and Engineering Chemistry Research,* vol. 51, pp. 2603-2608, 2012.

[40] I. Dewi, I. Indrajati and I. Setyorini, "Blends of nitrile butadiene rubber/poly (vinyl chloride): The use of maleated anhydride castor oil based plasticizer," *Majalah Kulit, Karet Dan Plastik,* vol. 32, no. 1, pp. 51-58, 2016.

[41] I. Indrajati and I. Dewi, "Performance of maleated castor oil based plasticizer on rubber: rheology and curing characteristic studies," *IOP Conference Series: Materials Science and Engineering,* vol. 223, 2016.

[42] C. Merlini, V. Soldi and G. M. Barra, "Influence of fiber surface treatment and length on physico-chemical properties of short random banana fiber-reinforced castor oil polyurethane composites," *Polymer Testing,* vol. 30, pp. 833-840, 2011.

[43] V. M. Wik, M. I. Arungeren and M. A. Mosiewicki, "Castor oil-based polyurethanes containing cellulose nanocrystals," *Polymer Engineering & Science,* vol. 51, pp. 1389-1396, 2011.

[44] A. Kaushik, D. Ahuja and V. Salwani, "Synthesis and characterization of modified clay/castor oil based chain extended polyurethane nanocomposites," *Composites. Part A,* vol. 42, pp. 1534-1541, 2011.

[45] S. Miao, Y. Liu, P. Wang and S. Zhang, "Castor oil and microcrystalline cellulose based polymer composites with high tensile strength," *Advanced Materials Research,* vol. 399, pp. 1531-1535, 2012.

[46] Z. Gao, J. Peng, T. Zhong, J. Sun, X. Wang and C. Yue, "Bionanocomposites from elastomer of waterborne polyurethane based on castor oil and polyethylene glycol with cellulose nanocrystals," *Carbohydrate Polymers,* vol. 87, pp. 2068-2075, 2012.

[47] E. M. Maafi, L. Tighzert and F. Malek, "Elaboration and characterization of composites of castor oil-based polyurethane and fibers from alfa stems," *Journal of Applied Polymer Science,* vol. 118, pp. 902-909, 2010.

[48] C. Zhang, S. Madbouly and M. Kessler, "Biobased polyurethanes prepared from different vegetable oils," *ACS Applied Materials & Interfaces,* vol. 7, pp. 1226-1233, 2015.

[49] S. Rana, N. Karak, J. W. Cho and Y. H. Kim, "Enhanced dispersion of carbon nanotubes in hyperbranched polyurethane and properties of nanocomposites," *Nanotechnology,* vol. 19, p. 495707, 2008.

[50] N. Paluvai, S. Mohanty and S. Nayak, "Mechanical and thermal properties of sisal fiber reinforced acrylated epoxidized castor oil toughened diglycidyl ether of bisphenol A epoxy nanocomposites," *Journal of Reinforced Plastics and Composites,* vol. 34, no. 18, pp. 1476-1490, 2015.

[51] S. Mutalikdesai, G. Sujaykumar, A. Raju, C. Moses, J. Jose and V. Lakshmanan, "Mechanical characterization of epoxy/basalt fiber/flax fiber hybrid composites," *American Journal of Materials Science,* vol. 7, no. 4, pp. 91-94, 2017.

[52] V. Manikandan, P. Amuthakkannan and V. Arumuga Prabu, "Review on natural fiber composites: Banana/hemp fiber and its hybrid composites," *International Journal of Composite Material and Matrices,* vol. 1, no. 2, pp. 1-14, 2015.

[53] J. D. Rahman, M. Yunus, T. Yezdani and A. Ramkrishna, "Road map for the selection of characteristic parameters of polymer matrix composites for engineering applications," *International Journal of Emerging Technology and Advanced Engineering,* vol. 2, no. 7, pp. 63-70, 2012.

[54] P. Mallick, Fiber-reinforced Composites: Materials, Manufacturing and Design, Boca Raton, FL: CRC Press, 2008.

[55] P. Peças, H. Carvalho, H. Salman and M. Leite, "Natural fibre composites and their applications: A review," *Journal of Composites Science,* vol. 2, no. 66, pp. 1-20, 2018.

[56] N. Ramli, N. Mazlan, Y. Ando, Z. Leman, K. Abdan, A. Aziz and N. Sairy, "Natural fiber for green technology in automotive industry: A brief review," *IOP Conference Series: Material Science and Engineering,* vol. 368, p. 012012, 2018.

[57] S. Sahoo, S. Mohanty and S. Nayak, "Mechanical, dynamic mechanical, and interfacial properties of sisal fiber-reinforced composite with epoxidized soybean oil-based epoxy matrix," *Polymer Composites,* pp. 2065-2072, 2018.

[58] D. Saheb and J. Jog, "Natural fiber polymer composites: A review," *Advances in Polymer Technology,* vol. 18, no. 4, pp. 351-363, 1999.

[59] S. Joshi, L. Drzal, A. Mohanty and S. Arora, "Are natural fiber composites environmetally superior to glass fiber reinfoced composites?," *Composites Part A: Applied Science and Manufacturing,* vol. 35, pp. 371-376, 2004.

[60] J. Prabakaran, C. Dinesh, M. Dinesh, A. Singh and A. Vasan, "Analysis of mechanical properties of sisal, jute, coir fibre (hybrid) reinforced epoxy composites," *International Journal of Science, Engineering and Technology Research,* vol. 6, no. 4, pp. 537-542, 2017.

[61] M. Ahmad, M. Majid, M. Ridzuan, A. Firdaus and N. Amin, "Tensile properties of interwoven hemp/PET (Polyethylene Terephthalate) epoxy hybrid composites," *Journal of Physics: Conference Series,* vol. 908, 2017.

[62] S. Koppula, A. Kaviti and K. Namala, "Experimental investigation of fibre reinforced composite materials under impact load," *IOP Conference Series: Materials Science and Engineering,* vol. 330, p. 012047, 2018.

[63] D. Hernandez, C. Soufen and M. Orlandi, "Carbon fiber reinforced polymer and epoxy adhesive tensile test failure analysis using scanning electron microscopy," *Materials Research,* vol. 20, no. 4, pp. 951-961, 2017.

[64] L. Mwaikambo and M. Ansell, "Chemical modification of hemp, sisal, jute, and kapok fibers by alkalization," *Journal of Applied Polymer Science,* vol. 84, pp. 2222-2234, 2001.

[65] M. Fogorasi and I. Barbu, "The potential of natural fibers for automotive sector - review," *IOP Conference Series: Material Science and Engineering,* vol. 252, p. 012044, 2017.

[66] R. Hu and J. Lim, "Fabrication and mechanical properties of completely biodegradable hemp fiber reinforced polylactic acid composites," *Journal of Composite Materials,* vol. 41, no. 13, pp. 1655-1669, 2007.

[67] A. Komuraiah, S. K. N. and B. Durga Prasad, "Chemical composition of natural fibers and its influence on their mechanical properties," *Mechanics of Composite Materials,* vol. 50, no. 3, 2014.

[68] H. Hargitai, I. Rácz and R. Anandjiwala, "Development of hemp fiber reinforced polypropylene composites," *Journal of Thermoplastic Composite Materials,* vol. 21, pp. 165-174, 2008.

[69] M. Ansell and L. Mwaikambo, "The structure of cotton and other plant fibres," in *Handbook of Textile Fibre Structure*, vol. 2, Sawston, UK, Woodhead Publishing, 2009, pp. 62-94.

[70] I. Raftoyiannis, "Experimental testing of composite panels reinforced with cotton fibers," *Open Journal of Composite Materials,* vol. 2, pp. 31-39, 2012.

[71] S. Grishanov, "Structure and properties of textile materials," in *Handbook of Textile and Industrial Dyeing*, vol. 1, Sawston, UK, Woodhead Publishing, 2011, pp. 28-63.

[72] M. Symington, O. David-West, W. Banks, J. Thomason and R. Pethrick, "Vacuum infusion of natural fibre comoposites for structural applications," in *13th European Conference on Composite Materials (EECM 13)*, 2008.

[73] M. I. Arungeren, I. Rácz and N. E. Marcovich, "Microfoams based on castor oil polyurethanes and vegetable fibers," *Journal of Applied Polymer Science,* vol. 105, pp. 2791-2800, 2007.

[74] N. Graupner, "Application of lignin as natural adhesion promoter in cotton fibre-reinforced poly(lactic acid) (PLA) composites," *Journal of Material Science,* vol. 43, pp. 5222-5229, 2008.

[75] A. Timar-Balazsy and D. Eastop, Chemical Principles of Textile Conservation, London, UK: Routledge, 2012, p. 35.

[76] K. Abdurohman, T. Satrio, N. Muzayadah and Teten, "A comparison process between hand lay-up, vacuum infusion and vacuum bagging method toward e-glass EW 185/lycal composites," *Journal of Physics: Conference Series,* vol. 1130, p. 012018, 2018.

[77] M. Mehdikhani, L. Gorbatikh, I. Verpoest and S. Lomov, "Voids in fiber-reinforced polymer composites: A review on their formation, characteristics, and effects on mechanical performance," *Journal of Composite Materials,* vol. 53, no. 12, pp. 1579-1669, 2019.

[78] A. Elshabini, F. Barlow and P. Wang, "Semiconductor Packages," in *Encyclopedia of Materials: Science and Technology*, 2nd ed., Oxford, UK, Pergamon Press, 2001, pp. 8339-8356.

[79] D. Rosato, D. Rosato and M. Rosato, Plastic Product Material and Process Selection Handbook, Amsterdam, Netherlands: Elsevier Science, 2004, pp. 439-454.

[80] C. Park and W. Lee, "Compression molding in polymer matrix composites," in *Manufacturing Techniques for Polymer Matrix Composites (PMCs)*, Sawston, UK, Woodhead Publishing, 2012, pp. 47-94.

[81] D. Dixit, R. Pal, G. Kapoor, Stabenau and M., "Lightweight composite materials processing," in *Lightweight Ballistic Composites: Military and Law-Enforcement Applications*, 2nd ed., Sawston, UK, Woodhead Publishing, 2016, pp. 157-216.

[82] A. Luyt and S. Malik, "Can Biodegradable Plastics Solve Plastic Solid Waste Accumulation?," in *Plastics to Energy: Fuel, Chemicals and Sustainability Implications*, William Andrew Publishing, 2019, pp. 403-423.

[83] K. Leja and G. Lewandowicz, "Polymer Biodegradation and Biodegradable Polymers," *Polish Journal of Environmental Studies,* vol. 19, no. 2, pp. 255-266, 2010.

[84] M. Abhilash and D. Thomas, "Biopolymers for biocomposites and chemical sensor applications," in *Biopolymer Composites in Electronics*, Amsterdam, Netherlands, Elsevier, 2017, pp. 405-435.

[85] N. Lucas, C. Bienaime, C. Belloy, M. Queneudec, F. Silvestre and J. Nava-Saucedo, "Polymer biodegradation: Mechanisms and estimation techniques - A review," *Chemosphere,* vol. 73, no. 4, pp. 429-442, 2008.

[86] J. Arutchelvi, M. Sudhakar, A. Arkatkar, M. Doble, S. Bhaduri and P. Uppara, "Biodegradation of polyethylene and polypropylene," *Indian Journal of Biotechnology,* vol. 7, pp. 9-22, 2008.

[87] A. Albertsson and S. Karlsson, "Biodegradable polymers," in *Comprehensive Polymer Science: The Synthesis, Characterization, Reactions and Applications of Polymers*, Amsterdam, Netherlands, Elsevier, 1996, pp. 285-297.

[88] L. Sperling, Introduction to Physical Polymer Science, New York, NY: John Wiley & Sons, 2001, p. 312.

[89] ASTM D6110-17 Standard Test Method for determining the Charpy impact resistance of notched specimens of plastics, West Conshohocken, PA: ASTM International, 2018.

[90] ASTM D638-14 Standard test method for tensile properties of plastics, West Conshohocken, PA: ASTM International, 2014.

[91] ASTM D3822-14 Standard test method for tensile properties of single textile fibers, ASTM International, 2014.

[92] J. C. Halpin and J. L. Kardos, "The Halpin-Tsai equations: a review," *Polymer Engineering & Science,* vol. 16, pp. 344-352, 1976.

[93] M. C. Gupta and A. P. Gupta, Polymer Composites, 3rd ed., London, UK: New Academic Science, 2019.

[94] M. Abdel Ghafaar, A. A. Mazen and N. A. El-Mahallawy, "Application of the rule of mixtures and Halpin-Tsai equations to woven fabric reinforced epoxy composites," *Journal of Engineering Sciences, Assiut University,* vol. 34, no. 1, pp. 227-236, 2006.

[95] D. Tam, S. Ruan, P. Gao and T. Yu, "High-performance ballistic protection using polymer nanocomposites," in *Advances in Military Textiles and Personal Equipment*, Woodhead Publishing, 2012, pp. 213-237.

[96] ASTM D7264-15 Standard test method for flexural properties of polymer matrix composite materials, West Conshohocken, PA: ASTM International, 2015.

[97] ASTMD D5988-18 Standard test method for determining aerobic biodegradation of plastic materials in soil, West Chonshohocken: ASTM International, 2018.

[98] S. Ghorui, N. Bandyopadhyay, D. Ray, S. Sengupta and T. Kar, "Use of maleated castor oil as biomodifier in unsaturated polyester resin/fly ash composites," *Industrial Crops and Products,* vol. 34, pp. 893-899, 2011.

[99] D. Pavia, G. Lampman, G. Kriz and J. Vyvyan, Introduction to Spectroscopy, USA: Brooks/Cole Cengage Learning, 2009.

[100] F. Wu and O. Musa, "Vegetable Oil-Maleic Anhydride and Maleimide Derivatives," in *Handbook of Maleic Anhydride Based Materials: Synthesis, properties and applications*, Springer, 2016, p. 159.

[101] D. Askeland and W. Wright, The Science and Engineering of Materials, 7 ed., Boston, MA: Cengage Learning, 2016.

[102] I. Katime, J. R. Quintana and C. Price, "Influence of the microstructural morphology on the mechanical properties of high-impact polystyrene," *Materials Letters,* vol. 22, pp. 297-301, 1995.

[103] D. Hull and T. W. Clyne, An Introduction to Composite Materials, 2nd ed., Cambridge, UK: Cambridge University Press, 1996.

[104] M. Mosiewicki, M. Aranguren and J. Borrajo, "Mechanical Properties of Linseed Oil Monoglyceride Maleate/Styrene Copolymers," *Journal of Applied Polymer Science,* vol. 97, pp. 825-836, 2005.

[105] J. Brandrup, E. Immergut and E. Grulke, Polymer Handbook, 4th ed., New York, NY: John Wiley & Sons, 2003.

[106] A. Farouk, N. Langrana and G. Weng, "Modulus prediction of a cross-ply fiber reinforced fabric composite with voids," *Polymer Composites,* vol. 13, pp. 285-294, 1992.

[107] D. Bachtiar, S. M. Sapuan, A. Khalina, E. S. Zainudin and K. Z. Dahlan, "The flexural, impact and thermal properties of untreated short sugar palm fibre reinforced high impact polystyrene (HIPS) composites," *Polymers and Polymer Composites,* vol. 20, pp. 493-502, 2012.

[108] J. Bergström, "Experimental Characterization Techniques," in *Mechanics of Solid Polymers: Theory and Computational Modelling*, Norwich, NY, William Andrew Applied Science Publishers, 2015, pp. 19-114.

[109] M. Biron, Material Selection for Thermoplastic Parts: Practical and Advanced Information for Plastics Engineers, Elsevier, 2016.

[110] S. Mustapha and L. Ye, "Non-Destructive evaluation (NDE) of composites: assessing debonding in sandwich panels using guided waves," *Woodhead Publishing Series in Composites Science and Engineering,* pp. 238-278, 2013.

[111] J. Momanyi, M. Herzog and P. Muchiri, "Analysis of thermomechanical properties of selected class of recycled thermoplastic materials based on their applications," *Recycling,* vol. 4, p. 33, 2019.

[112] G. P. Leal and J. M. Asua, "Evolution of the morphology of HIPS particles," *Polymer,* vol. 50, pp. 68-76, 2009.

[113] M. Misnon, M. Islam, J. Epaarachchi and K. Lau, "Analyses of woven hemp fabric characteristics for composite reinforcement," *Materials and Design,* vol. 66, pp. 82-92, 2015.

[114] M. Poletto, H. L. Ornaghi and A. J. Zattera, "Thermal decomposition of natural fibers: Kinetics and degradation mechanisms," in *Reactions and Mechanisms in Thermal Analysis of Materials*, Beverly, MA, Scrivener Publishing LLC, 2015, pp. 515-546.

[115] D. Bachtiar, S. Sapuan, E. Zainudin, A. Khalina and K. Dahlan, "Thermal properties of alkali-treated sugar palm fibre reinforced high Impact polystyrene composites," *Pertanika Journal of Science and Technology,* vol. 21, no. 1, pp. 141-150, 2013.

[116] S. Seleem, M. Hopkins, J. Olivio and D. Schiraldi, "Comparison of thermal decomposition of polystyrene products vs. bio-based polymer aerogels," *Ohio Journal of Science,* vol. 117, no. 2, pp. 50-60, 2017.

[117] J. Ahmad, K. Bazaka, M. Oelgemoller and M. Jacob, "Wetting, solubility and chemical characteristics of plasma-polymerized 1-isopropyl-4-methyl-1,4-cyclohexadiene thin films," *Coatings,* vol. 4, pp. 527-552, 2014.

[118] R. Förch, H. Schönherr and A. Jenkins, Surface Design: Applications in Bioscience and Nanotechnology, Wiley-VCH, 2009, p. 471.

[119] X. Mamat, Y. Wang and W. Eli, "New potentially environmentally friendly copolymer of styrene and maleic acid-castor oil monoester," *Polymers Advanced Technologies,* vol. 23, pp. 1271-1275, 2012.

[120] G. Lampman, D. Pavia, G. Kriz and J. Vyvyan, Spectroscopy, 4th ed., Brooks/Cole Cengage Learning, 2010.

[121] S. Ebnesajjad, "Adhesion Promoters," in *Surface Treatment of Materials for Adhesive Bonding*, 2nd ed., Norwich, NY, William Andrew, 2014, pp. 301-329.

[122] R. Abargues, U. Nickel and P. Rodriguez-Canto, "Charge dissipation in e-beam lithography with Novolak-based conducting polymer films," *Nanotechnology,* vol. 19, 2008.

[123] C. Mothé and C. De Araujo, "Properties of polyurethane elastomers and composites by thermal analysis," *Thermochimica acta,* no. 357-358, pp. 321-325, 2000.

[124] J. Müller, W. Van Biesen and P. Saling, "BASF," 2008. [Online]. Available: https://www.basf.com/global/en/who-we-are/sustainability/management-and-instruments/quantifying-sustainability/eco-efficiency-analysis/examples/lupranol-balance-50.html.

[125] W. Reusch and J. Clark, "Chemistry LibreTexts," 2015. [Online]. Available: https://www.google.co.za/search?q=condensation+polymerization+mechanism&sa=X&tbm=isch&tbo=u&source=univ&ved=0ahUKEwjQ5_aPq6jcAhUFSsAKHdCjBgsQsAQIPA&biw=1920&bih=974#imgrc=x_IKlIApbEwgAM:.

[126] M. Belgacem and A. Gandini, Monomers, polymers and composites from renewable resources, M. Belgacem and A. Gandini, Eds., Elsevier, 2008, p. 53.

[127] "Chinese Medicine Division," 2019. [Online]. Available: http://www.cmd.gov.hk/hkcmms/vol8/Vol8_pdf_English/Appendix/Appendices_E_XIV.pdf .

[128] L. Rohen, A. Neves, D. Mantovani, F. Mauricio, J. Da Silva Vieira, L. Pontes, F. Margem and S. Monteir, "Hemp fiber density using the pycnometry technique," *Characterization of Minerals, Metals and Materials,* pp. 423-428, 2017.

[129] L. Carvalho, E. Canedo, S. Farias Neto, A. Barbosa de Lima and C. Silva, "Moisture transport process in vegetable fiber composites: Theory and analysis for technological applications," *Advanced Structured Materials,* vol. 36, pp. 37-62, 2013.

[130] R. Petrucci, C. Santulli, D. Puglia, F. Sarasini, L. Torre and J. Kenny, "Mechanical characterisation of hybrid composite laminates based on basalt fibres in combination with flax, hemp and glass fibres manufactured by vacuum infusion," *Materials and Design,* vol. 49, pp. 728-735, 2013.

[131] S. Sharma, L. Sowntharya and K. Kar, "Polymer-Based Composite Structures: Processing and Applications," in *Composite Materials: Processing, applications and characterizations*, Springer, Berlin, Heidelberg, 2016, pp. 1-36.

[132] Vacman, "Vacmobiles.com," 2012. [Online]. Available: https://www.vacmobiles.com/resin_infusion.html.

[133] Richmond Aerovac, "EC Fibre Glass Supplies," 2019. [Online]. Available: https://www.ecfibreglasssupplies.co.uk/topic/wetlayupwithvacuumbag.

[134] G. Francucci, N. Manthey, F. Cardona and T. Aravinthan, "Processing and characterization of 100% hemp-based biocomposites obtained by vacuum infusion," *Journal of Composite Materials,* vol. 48, no. 11, pp. 1323-1335, 2014.

[135] J. Zhao, P. Yu and S. Dong, "The Influence of Crosslink Density on the Failure Behaviour in Amorphous Polymers by Molecular Dynamics Simulations," *Materials,* vol. 9, 2016.

[136] B. Hulugappa, M. Achutha and B. Suresha, "Effect of Filler on Mechanical Properties and Fracture Toughness of Glass Fabric Reinforced Epoxy Composites," *Journal of Minerals and Materials Characterization and Engineering,* vol. 4, pp. 1-14, 2016.

[137] S. Bobade, N. Paluvai, S. Mohanty and S. Nayak, "Bio-based thermosetting resins for future generation: A review," *Polymer-Plastics Technology and Engineering,* vol. 55, no. 17, pp. 1863-1896, 2016.

[138] P. Sharma, A. Srivastava and A. Pandey, "Tensile and impact strength analysis of cotton fiber reinforced polymer composites," *Asia Pacific Journals,* vol. 6, pp. 1-5, 2017.

[139] F. Campbell, Structural Composite Materials, Cleveland, OH: ASM International, 2010.

[140] M. Sharaf and J. Mark, "The effects of cross-Linking and strain on the glass transition temperature of a polymer network," *Rubber Chemistry and Technology,* vol. 53, no. 4, pp. 982-987, 1980.

[141] T. Foley, "Chemistry World," Royal Society of Chemistry, 2017. [Online]. Available: https://www.chemistryworld.com/news/castable-polymers-made-from-castor-beans/3007982.article.

[142] K. Chan and J. Tan, Understanding Advanced Organic and Analytical Chemistry, WS Education, 2017.

[143] F. Liu and J. Zhu, "Plant-oil-based polymeric materials and their applications," *RSC Green Chemistry,* vol. 29, pp. 93-126, 2015.

Appendix A: Temperature profiling of the vulcanization press

Experimental Procedure

A temperature profile of the vulcanization press was done by fastening type-K thermocouples to the bottom platen of the vulcanization press. The temperature at each setting (low, medium and high as seen in Figure 73) was recorded until the temperature stabilized. This was recorded using a Pico Technology USB TC-08 Temperature Data Logger. The placement of the thermocouples can be seen in Figure 74 as shown by the red dots.

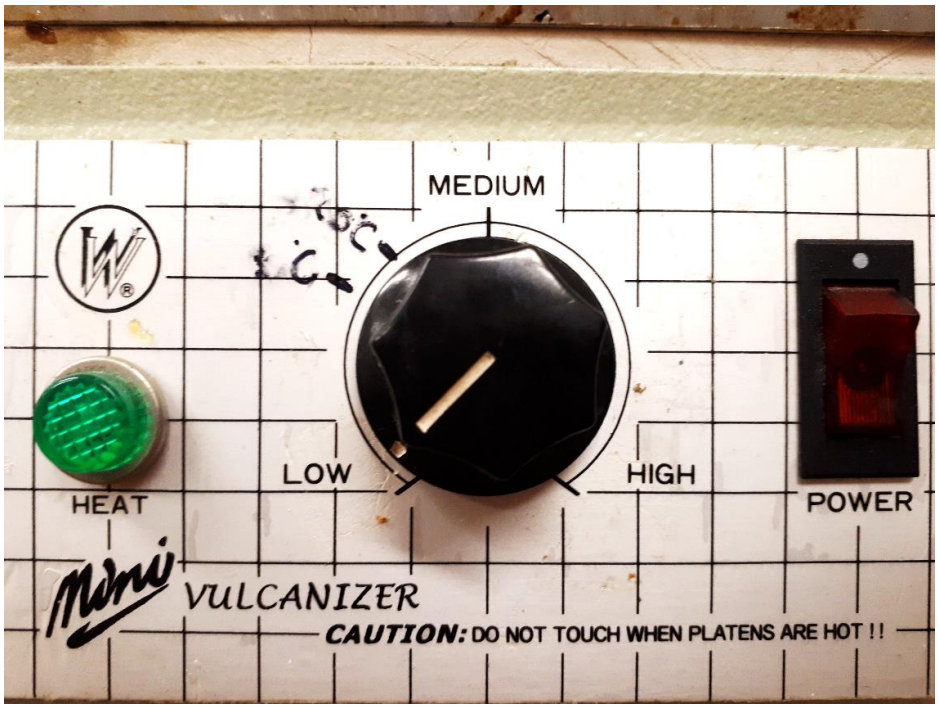

Figure 73: Temperature settings on the vulcanization press

Results

As seen in the experimental procedure, each channel represents a spot on the vulcanization press. The profiling was done to determine if the vulcanization press showed uniform heating throughout the plate.

Considering Figure 75 the low setting on the press reached a maximum temperature of about 48.5°C. The graph for each channel is relatively close to each other except for Channel 5 being an outlier. Nonetheless the overall range across the platen was less than 2°C. There is a decrease in the temperature after the maximum temperature for a particular setting is reached. This is due to the fact that the temperature sensor switches off the heating element which allows for a drop of approximately 3°C before the heating element is switched on again.

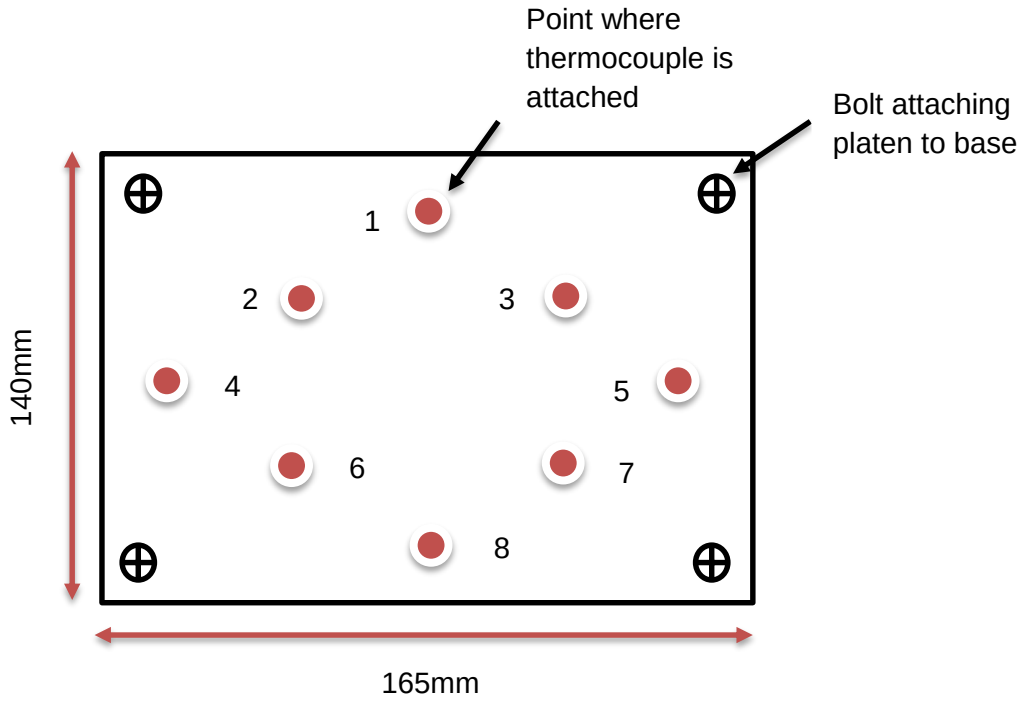

Figure 74: Map of temperature profile points on vulcanization press heating plate

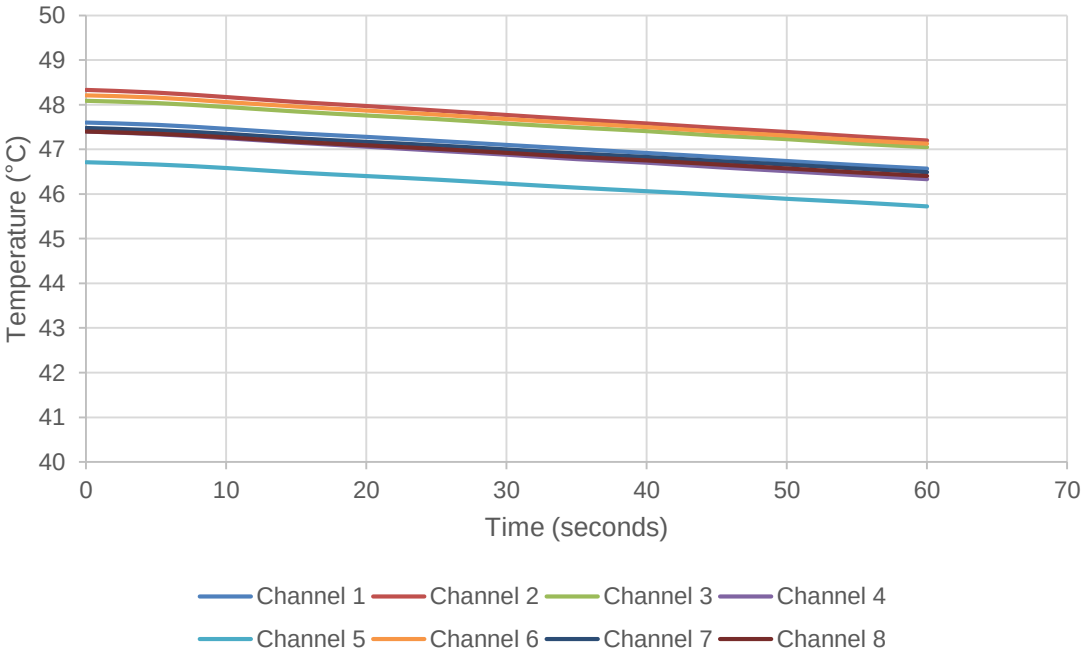

Figure 75: Temperature profile for low setting on vulcanization press

Figure 76 shows an initial increase in the temperature of the press platen until the maximum temperature for the medium setting was reached. This was found to be just under 180°C. A decrease is seen in the temperature once again, immediately after the maximum temperature was reached. Uniform heating is seen from each channel with no outliers. The temperature values between the channels differed with approximately 5˚C (maximum difference).

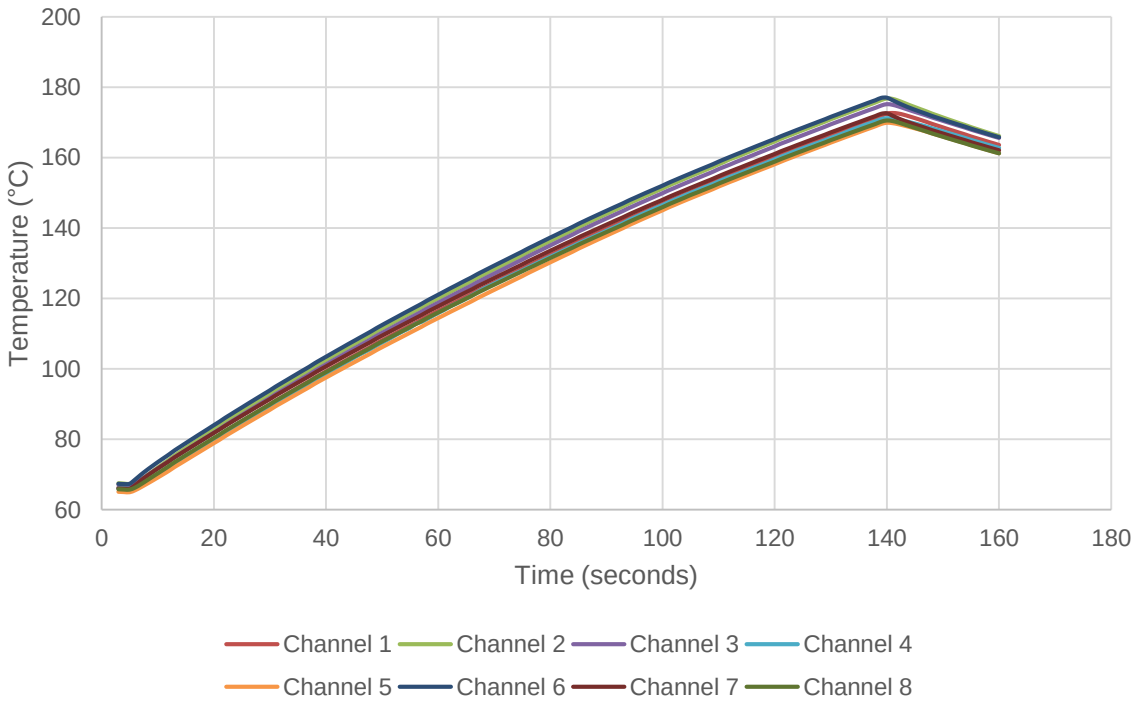

Figure 76: Temperature profile for medium setting on the vulcanization press

Uniform heating is seen in Figure 77 for the high setting on the vulcanization press. A maximum temperature of approximately 270˚C was reached.

The temperature profiling eliminated the possibility of insufficient curing caused by non-uniform heating over the platens. The range of temperatures achieved across the platen was deemed acceptable

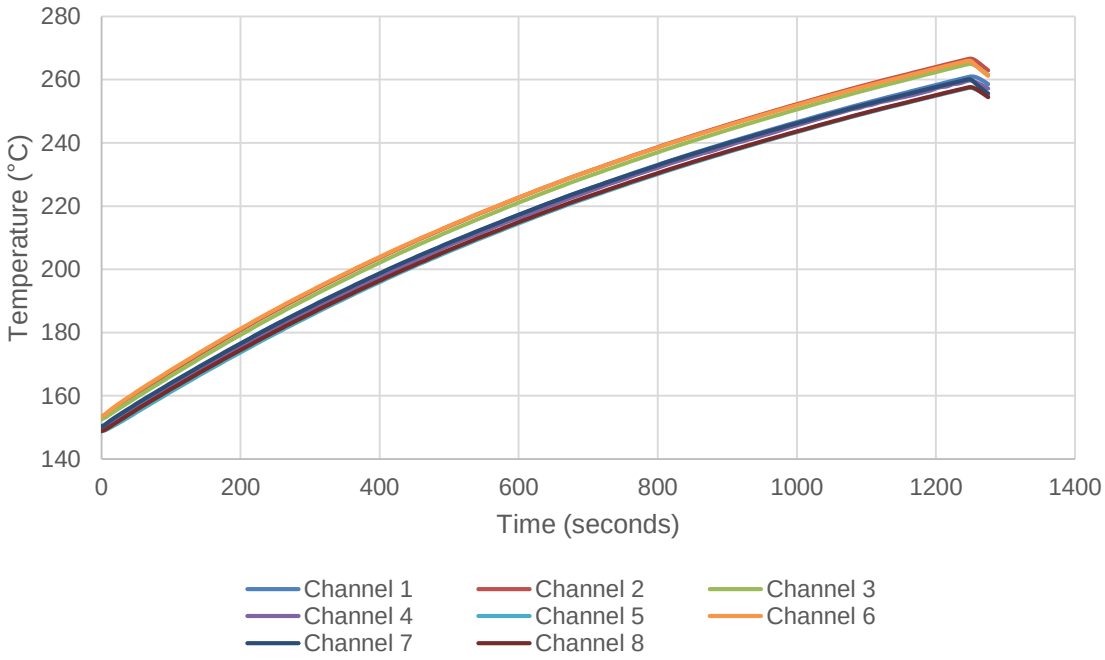

Figure 77: Temperature profile for the high setting on the vulcanization press

Appendix B: Tensile test of fibres

The tensile stress-strain curves for greige and hemp fibres with cross-sectional areas determined by measurement can be seen in Figure 78 and Figure 79 respectively.

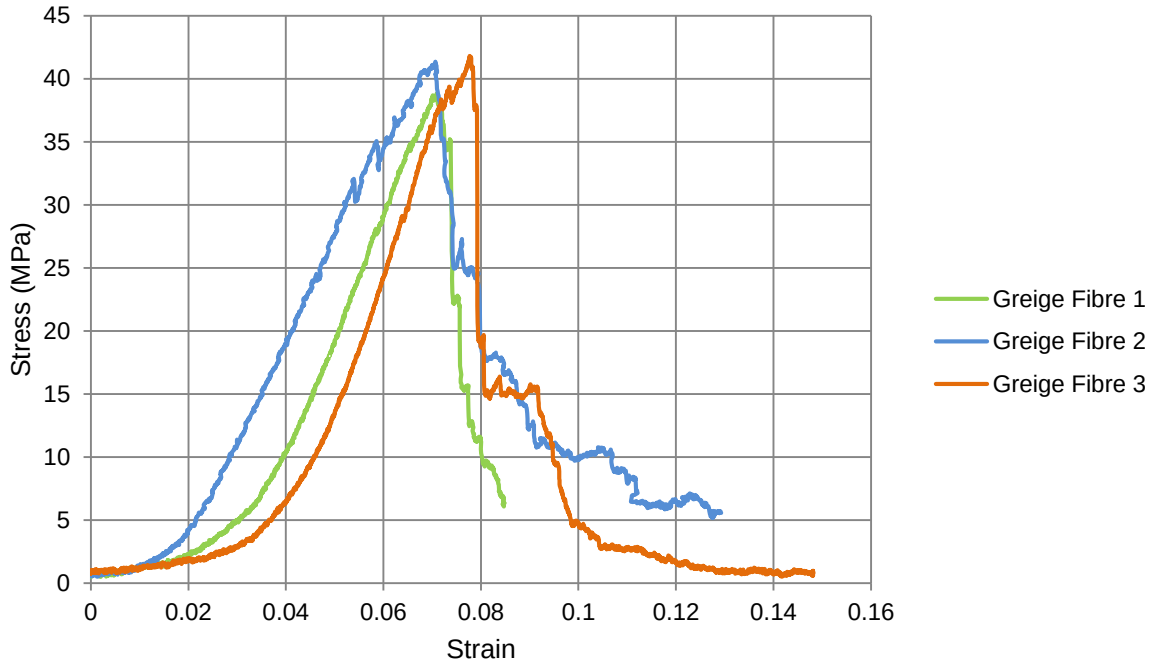

Figure 78: Tensile stress-strain curves for greige fibre

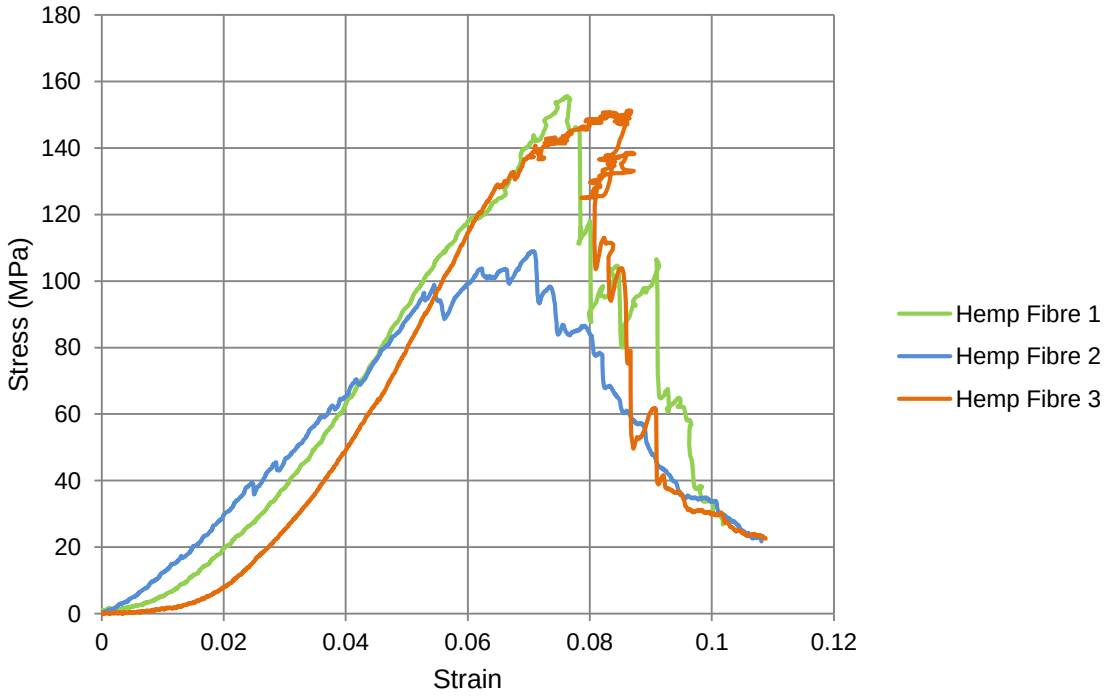

Figure 79: Tensile stress-strain curves for hemp fibre

Appendix C: Tensile stress-strain curves for biodegraded samples

The stress-strain curve for degraded MACOPS can be seen in Figure 80. Sample 2 was removed from data due to breaking before yielding.

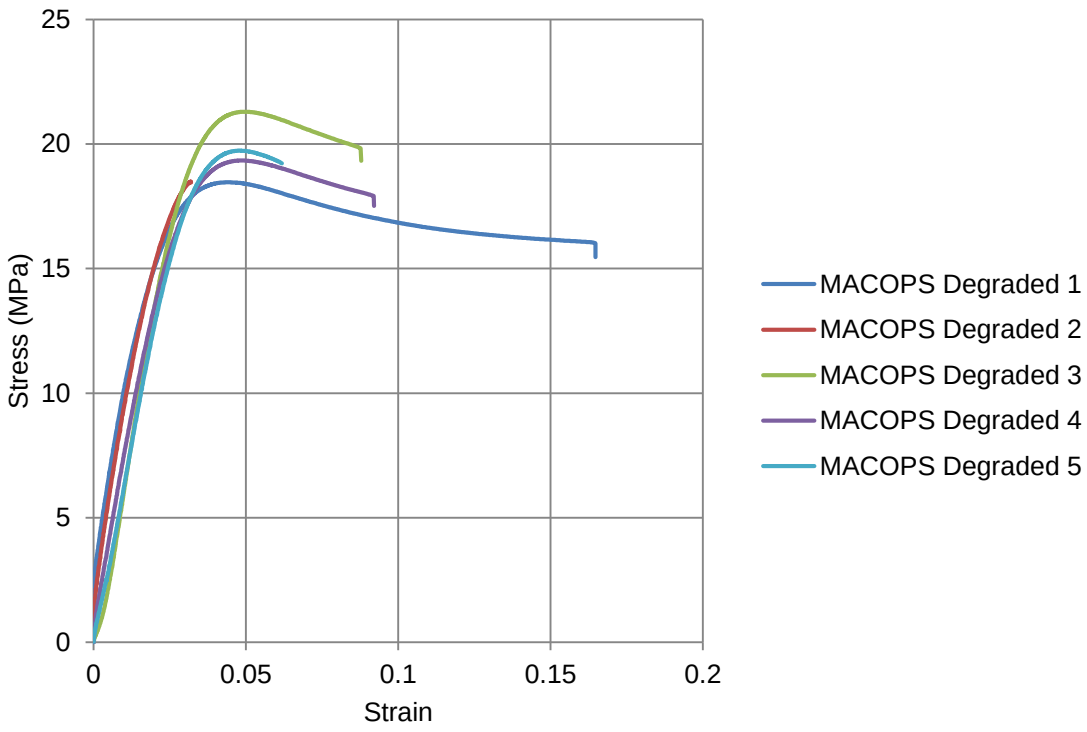

Figure 80: Tensile stress-strain curves of degraded MACOPS

After the biodegradability test the stress-strain curve for the GPPS CD-case can be seen in Figure 81. Note that these samples were cut using a blade, which could explain the scatter in UTS.

Figure 82 shows the tensile stress-strain curve for the degraded reinforced MACOPS.

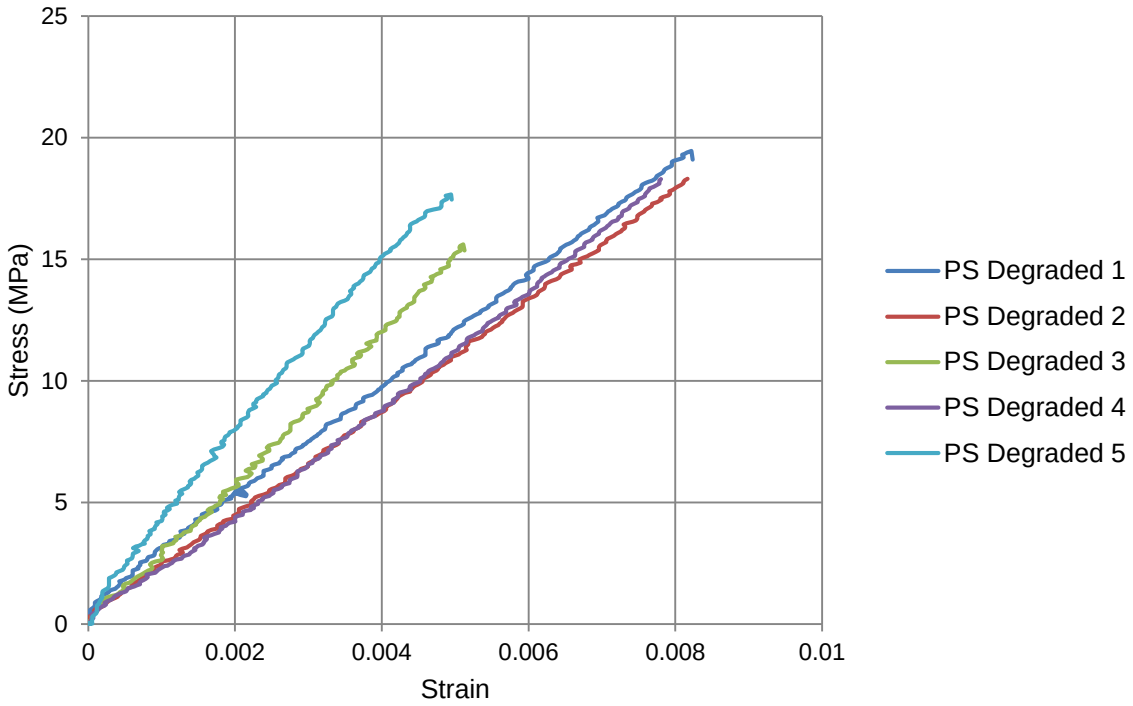

Figure 81: Tensile stress-strain curves for degraded PS CD-case (negative control)

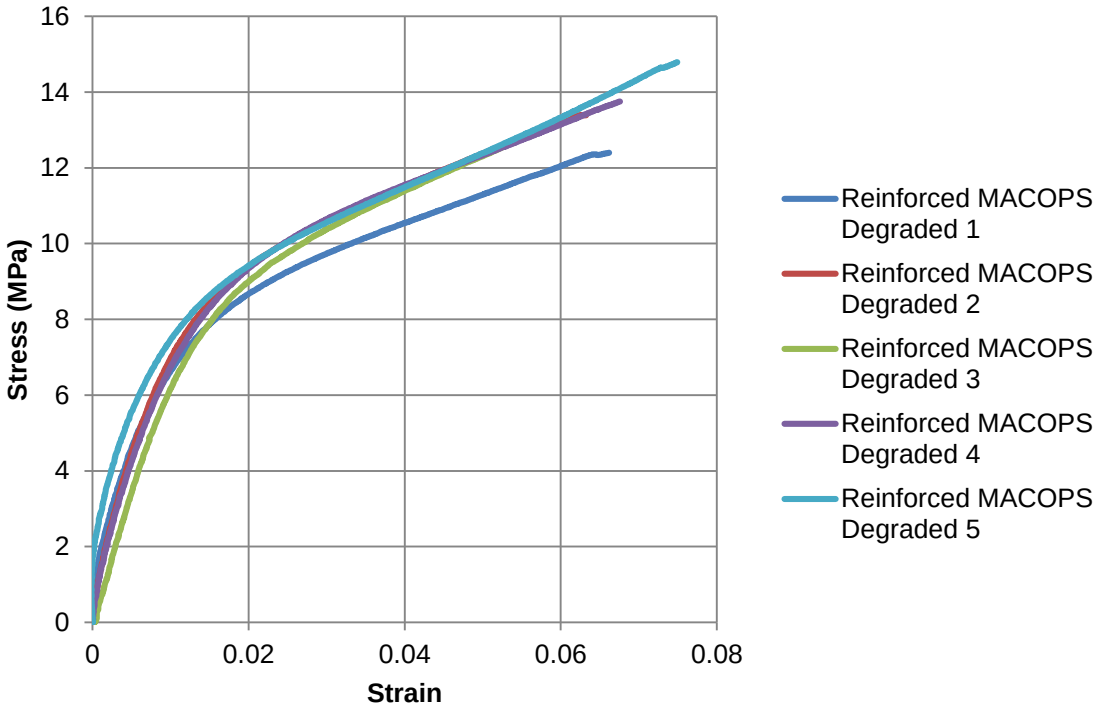

Figure 82: Tensile stress-strain curve for degraded reinforced MACOPS

Appendix D: Contact angles

The contact angle for MACOPS and degraded MACOPS can be seen in Figure 83 and Figure 84 respectively.

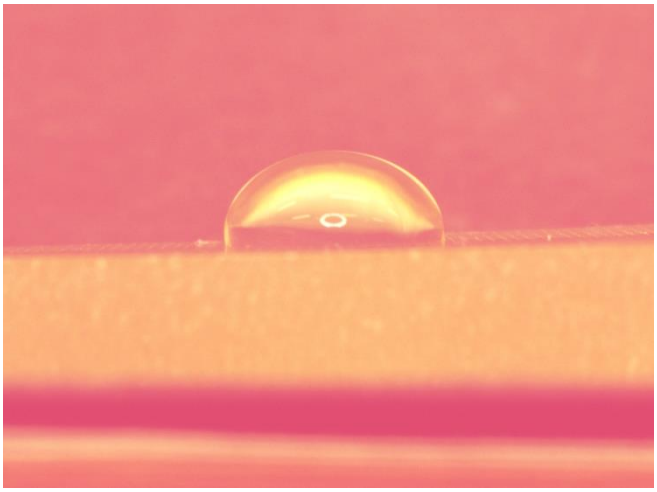

Figure 83: Contact angle of water droplet on original MACOPS

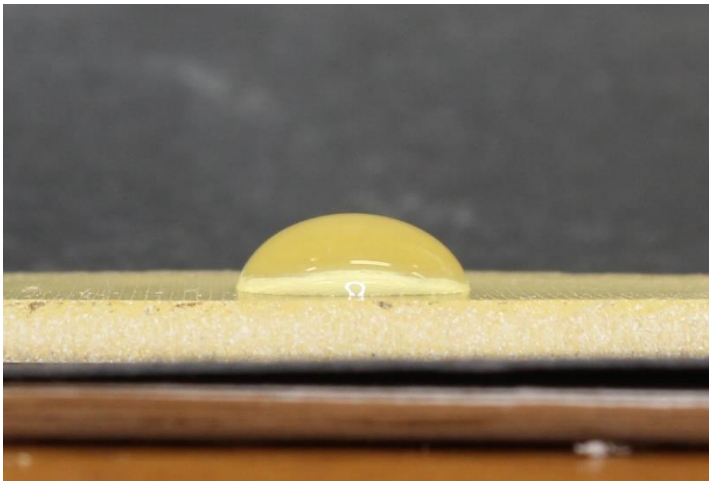

Figure 84: Contact angle of water droplet on degraded MACOPS

The contact angle for the reinforced MACOPS can be seen in Figure 85. For the degraded reinforced MACOPS the constant decrease can be seen in Figure 86 and Figure 87. Figure 88 shows the contact angle of the water droplet on the surface of the untreated woven greige fibres.

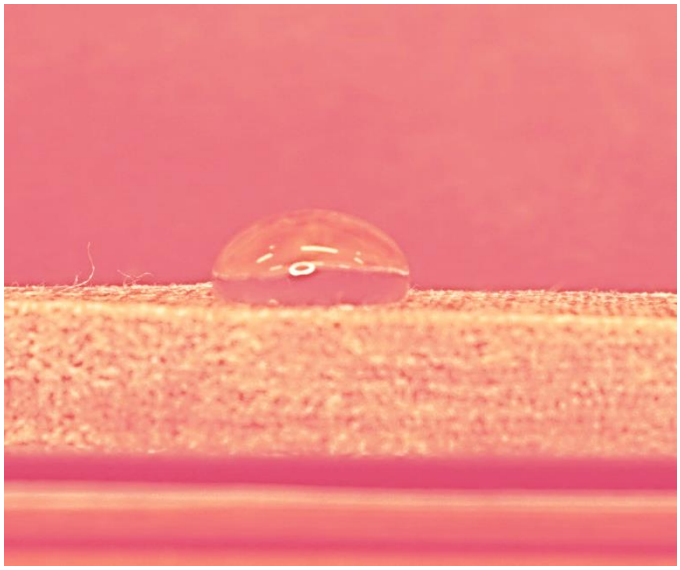

Figure 85: Contact angle of water droplet on original reinforced MACOPS

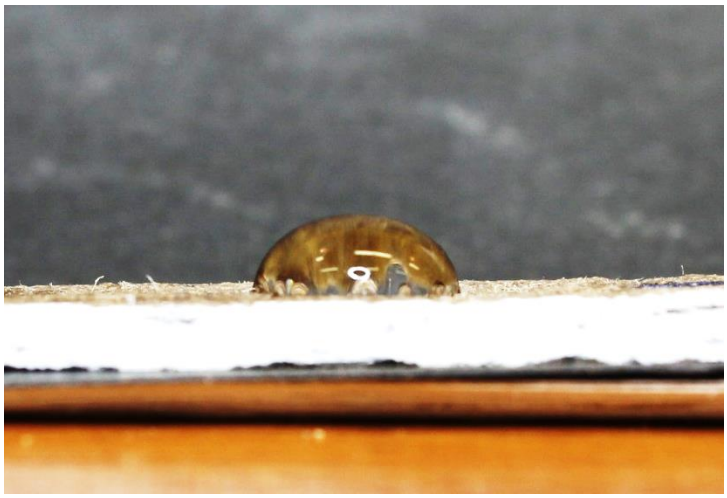

Figure 86: Contact angle of water droplet on degraded reinforced MACOPS (start)

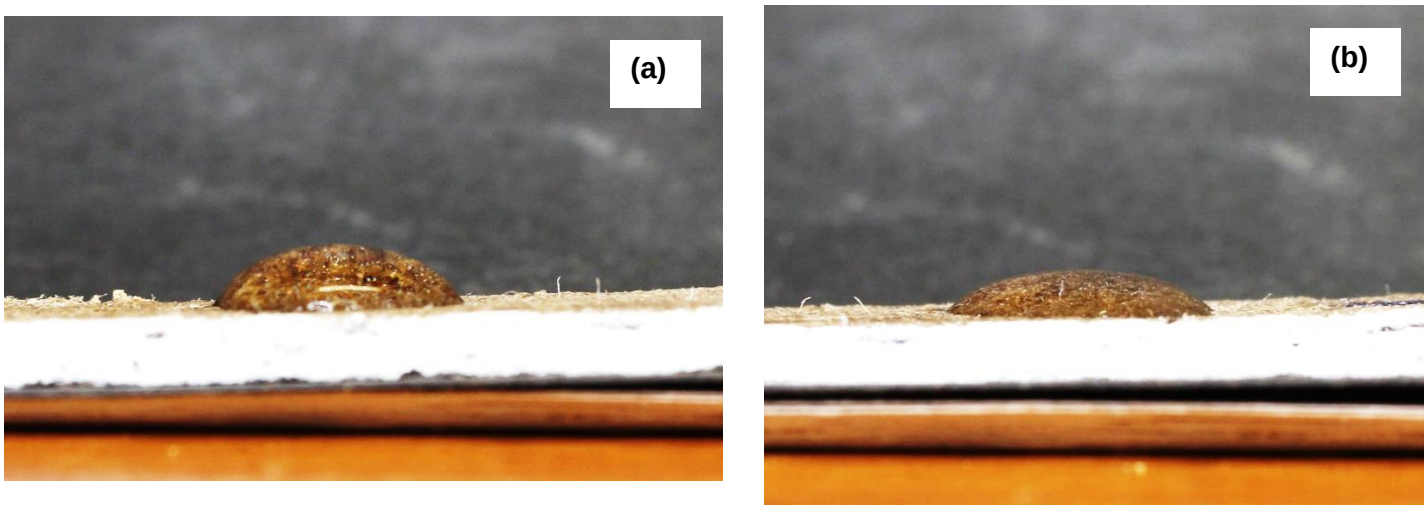

Figure 87: Contact angle of water droplet on degraded reinforced MACOPS after (a) 1 minute and (b) 1 minute 30 seconds

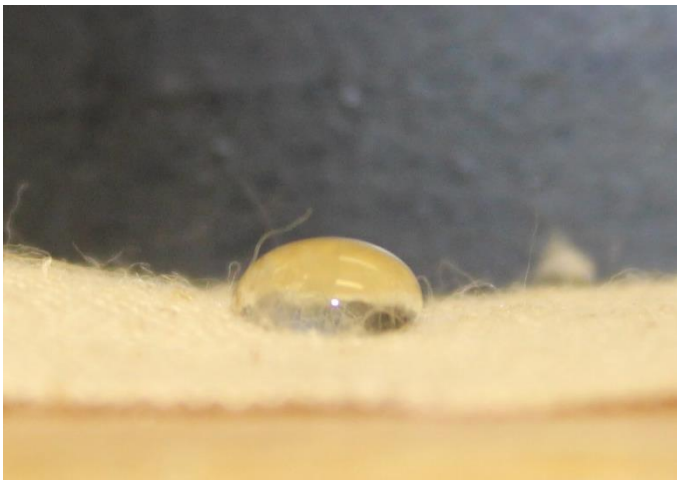

Figure 88: Contact angle of water droplet on the surface of untreated woven greige fibre